In-situ SEM electrochemistry and radiolysis

Møller-Nilsen, Rolf Erling Robberstad; Mølhave, Kristian; Norby, Poul; Wagner, Jakob Birkedal

Publication date:
2016

Document Version
Publisher's PDF, also known as Version of record

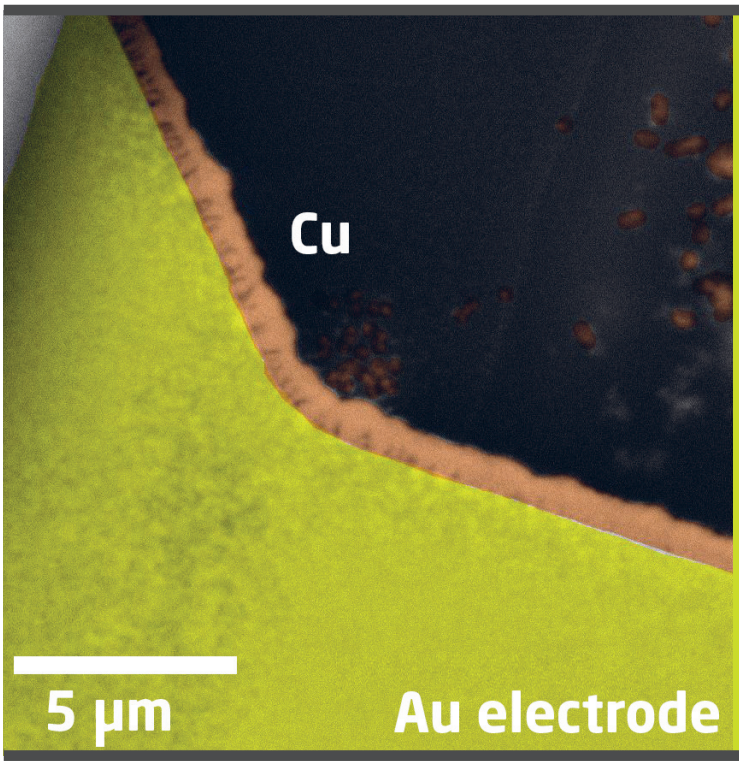

In-situ SEM electrochemistry and radiolysis

Rolf Erling Robberstad Møller-Nielsen
PhD Thesis March 2016

DTU Nanotech
Department of Micro- and Nanotechnology

In-situ SEM electrochemistry and radiolysis

Rolf Møller-Nilsen

PhD Thesis, March 2016

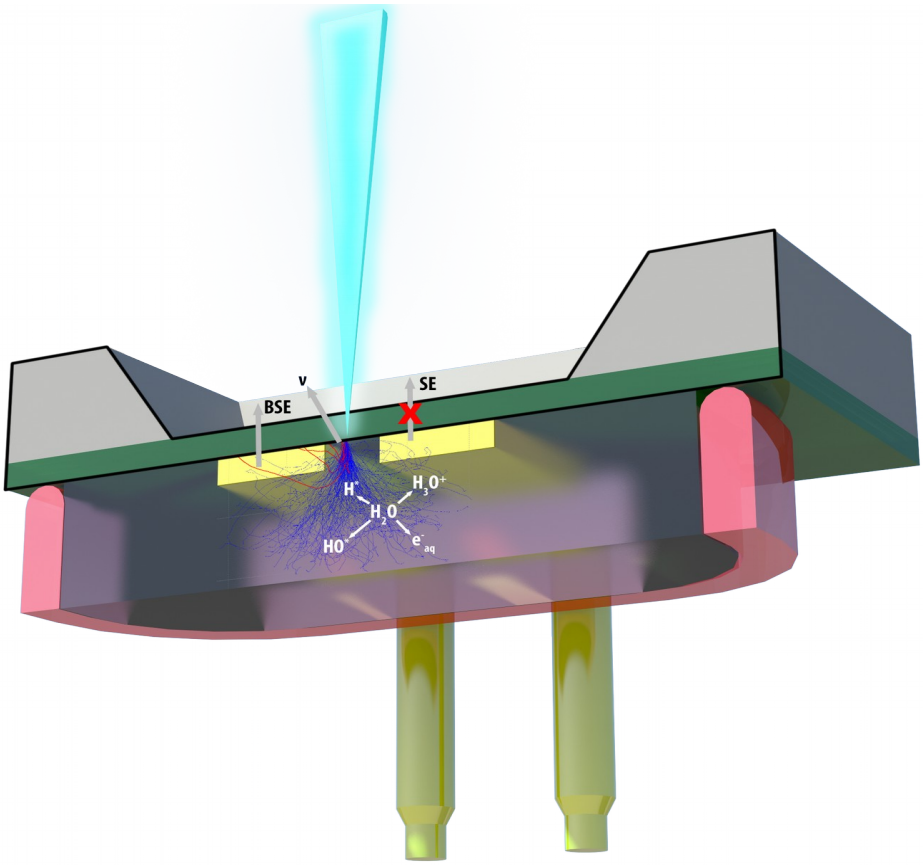

DTU Nanotech
Department of Micro- and Nanotechnology

Table of contents

Table of Contents

Preface

This thesis describes the main results from my PhD project on the topic of bean induced effects in in-situ electron microscopy cells. The majority of the work has been carried out at DTU Nanotech and DTU CEN. My work has been supervised by Associate Professor Kristian Mølhave (DTU Nanotech), Senior Researcher Poul Norby (DTU Energy) and Professor Jakob B. Wagner (DTU CEN). The project was funded by DTU Nanotech, DTU Energy and DTU CEN.

I would like to thank my supervisors for their generous patience and guidance. In particular Kristian who throughout the project has been keen on pitching in with interesting ideas for new studies and problem solving. His critical questions have also been instrumental in shaping the various chapters, a help I am very grateful for. Poul, for guiding me through electrochemistry. And finally Jakob who together with the lab responsible, Adam Fuller, have supported us when we have put unusual and potentially corrosive liquids in the electron microscopes at CEN.

My work would not have been possible without the help from my fellow group members in Molecular Windows: The experiments described in this thesis I have relied on the liquid cell developed by Eric Jensen. Several of the experiments in this thesis have been made possible by Silvia Canepa with whom I have spent many hours in the lab, at the microscope, and trotting the path in-between carrying cases upon cases with equipment. Hongyu Sun, who despite his relatively recent arrival has still been very valuable to form the conductivity-study. All the members of the group have been positive and helpful, and I am very grateful to have had the opportunity to work with them.

Finally I would like to thank the collaborators I have had on several smaller studies during my project, including; Izabela Kondratowicz from Gdansk University, Alexei Zhakarov and Anders Mikkelsen from Maxlab at Lund University.

Abstract

Electron microscopy is a ubiquitous technique to see effects which are too small to see with traditional optical microscopes. Recently it has become possible to also image liquid samples by encapsulating them from the vacuum of the microscope and a natural evolution from that has been to include microelectrodes on the windows to enable studies of electrohcemical processes. In this way it is possible to perform in-situ electrochemical experiments such as electroplating and charge- and discharge analysis of battery electrodes.

In a typical liquid cell, electrons are accelerated to sufficiently high energies to traverse a thin window made by a silicon nitride membrane, and interact with the sample immersed in liquid. In transmission electron microscopy (TEM) the majority of the electrons continue through the sample to form an image. In scanning electron microscopy (SEM) a fraction of the electrons are backscattered and an image is reconstructed by the microscope. But the high energy electrons are a form of ionising radiation which can significantly affect the chemistry in liquid experiments. Ionising radiation can split water, produce radicals, reduce dissolved metal ions to metal particles, and more. It is therefore essential to understand and control the radiolytic processes that results from in-situ electron microscopy experiments.

Although radiolysis has been studied extensively in connection with the advent of e.g. nuclear reactors the information obtained for that purpose often has to be extrapolated many orders of magnitude to reach the radiation conditions of the extremely focused beam of typical electron microscopes. To date there is a distinct lack of direct measurements and quantification of the radiolytic conditions for in in-situ liquid cells.

In this thesis an electrochemical in-situ SEM cell is used to study the radiolytic effects of the electron beam. Potentiometric measurements in-situ demonstrate that the electrolyte contains

hydrogen upon irradiation, and that the ratio of H_2O_2 to H_2 is only 1:2.5, much less than the predicted ratio of 1:1.1. Electrochemical impedance spectroscopy (EIS) measurements between two electrodes when irradiating at an average intensity of 6 MGy/s indicate that the conductivity may be at least 200 µS/cm, two orders of magnitude higher than what would be expected from H^+ alone. Finally, the radiolytic yield of copper is measured by gradually increasing the radiation intensity until copper precipitated. Based on the amount of backscattered electrons it has been possible to quantify the amount of reduced copper, resulting in an average radiolytic yield per 100 eV of deposited energy (g-value) of 0.05, lower than the value of 4.4 seen in pulse radiolysis experiments.

During the course of these studies it has also been possible to improve on the EC-SEM system. This has resulted in pyrolysed carbon electrodes, which offer the benefit of stability at 0.75 V higher potentials than traditional gold thin-film electrodes.

With the quantitative insight into the radiolytic conditions in liquid electron microscopy cells that this thesis provides it may be possible to design and analyse experiments where such effects are correctly accounted for. The results are therefore of high value for the in-situ community who until now have had to rely on only limited experimental data in combination with theoretical predictions that have been extrapolated several orders of magnitude.

Resumé

Elektronmikroskopi er udbredt metode til at se effekter der er for små til at se med almindelige mikroskoper. For nyligt er det blevet muligt også at observere prøver bestående av væsker ved at indkapsle dem fra mikroskopets vakuum. En naturlig udvikling derifra har været introduktionen af mikroelektroder på indkapslingens vinduer for at muliggøre studier af elektrokemiske processer. På denne måde er det muligt at udføre elektrokemiske forsøg så som elektroplattering og op- og afladningsanalyser af batterielektroder.

For at analysere prøver i en typisk væskecelle bliver elektronerne accelereret til så høj en energi, at de kan passere vinduet bestående af en siliciumnitrid-membran, hvorefter de kan interagere med væskeprøven. I et transmissionselektronmikroskop (TEM) passerer størstedelen af elektronerne igennem prøven og danner et billede på en passende sensor. I et scanning-elektronmikroskop (SEM) bliver en lille andel af elektronerne spredt tilbage gennem membranen, hvor de kan detekteres, og et billede rekonstrueres af mikroskopet.

Men fordi de accelerede elektroner er en form for ioniserende bestråling kan de påvirke kemien i væskeforsøg væsentligt. Ioniserende bestråling kan opdele vand, producere radikaler, reducere opløste metalioner til metalpartikler, med mere. Det er derfor meget vigtigt at forstå og at kunne kontrollere de radiolytiske processer der resulterer fra bestrålingen i in-situ forsøg.

Selv om radiolyse er blevet studeret i forbindelse med den voksende interessen for atomreaktorer i det forrige århundrede, er information fra den forbindelse ofte blevet ekstrapoleret mange størrelsesordener for at kunne beskrive strålingsforholdene der resulterer fra den ekstremt fokuserede elektronstråle i elektronmikroskoper. Til dags dato er der en væsentlig mangel på direkte målinger og kvantificering af de radiolytiske betingelser der er i in-situ væskeceller.

I denne afhandling bliver en elektrokemisk in-situ SEM-celle anvendt til at studere de radiolytiske effekter fra elektronstrålen. Potentiometriske målinger udført in-situ viser at elektrolytten indeholder hydrogen efter bestråling, og at forholdet mellem H_2O_2 og H_2 kun er 1:2,5, meget mindre end det forventede forhold på 1:1,1. Målinger med elektrokemisk impedansspektroskopi (EIS) mellem to mikroelektroder, hvor arealet mellem dem bestråles med en intensitet på 6 Mgy/s, indikerer at væskens ledningsævne sandsynligvis er mindst 200 µS/cm, to størrelsesordener højere end hvad man kan forvente fra radiolytisk H^+ alene. Afslutningsvis er den specifikke radiolytiske produktion målt ved gradvist at øge bestrålingsintensiteten indtil kobber udfældes. Baseret på mængden af tilbagespredte elektroner har det været muligt at bestemme mængden af reduceret kobber (g-værdien) til 0.05 kobber-atomer per 100 eV afsat energi, hvilket er lavere end den publicerede værdi fra puls-radiolyse på 4,4.

Som et led i disse studier har det også været muligt at forbedre systemet benyttet til væskestudier i SEM. Dette har resulteret i pyrolyserede karbonelektroder, der har den fordel at de er stabile til potentialer 0,75 V højere end traditionelle tyndfilmelektroder af guld.

Den kvantitative indsigt i de radiolytiske forhold i elektronmikroskopers væskeceller, som denne afhandlinger bringer, bidrager til at muliggøre design og analyse af forsøg der tager højde for de radiolytiske effekter der uundgåeligt vil være. Resultaterne er derfor af stor værdi for brugere af in-situ elektronmikroskopi som indtil nu har været nødsaget til at basere analysen på begrænsede eksperimentelle beskrivelse af radiolyse kombineret med teoretiske forudsigelser der har været ekstrapoleret flere størrelsesordener.

Chapter 1: Introduction

This thesis discusses important issues that have to be understood with electrochemistry in-situ electron microscopy, which is one of the tools currently used to improve our understanding of electrochemical systems. An example of such experiments is the nanoscale electrochemical plating and dissolution of copper in miniature electrochemical cells, in order to understand details that would otherwise remain unseen.

We rely heavily on electrochemical processes in everything that we do in today's society: Our phones and laptops are powered by batteries. The processors within them were made in part with electroplating of copper. Cars are becoming electrified, also those with the use of batteries, and the aluminium that is used in their production is refined by means of electrolysis. In some markets small fuel cells are even offered for sale as residential heat and power units. And yet, people are hassled by the fact that they have to recharge their phones too often, and the cars don't drive as far as people would like.

In-situ electron microscopy enables targeted research which can lead to improvements in electrochemical processes, whether that is electroplating, battery technology or fuel cells. Promising and revolutionary materials depend on such targeted research to become viable technologies. For example, lithium-based batteries have the highest voltages of common battery chemistries, which results in the highest energy densities. But lithium-ion batteries would not have become prevalent without the transition away from metallic lithium anodes, where dendrites formed during charging create an imminent risk of short circuits, fire, or worse. In the present and the future such advances may happen faster because of the additional power that comes from direct observation with in-situ electron microscopy.

The electron beam used for imaging in electron microscopes causes significant changes to the electrochemical environment being studied, and can make observations unreliable. Since the electron beam used for in-situ electron microscopy is a form of ionising radiation it will break bonds of the molecules present in the electrolyte to form new molecules including charged species and radicals. This process is called radiolysis. In order to correctly account for the radiolytic influence from the beam it is necessary to set up experiments which can quantify the changes to the electrolyte and electrochemical environment.

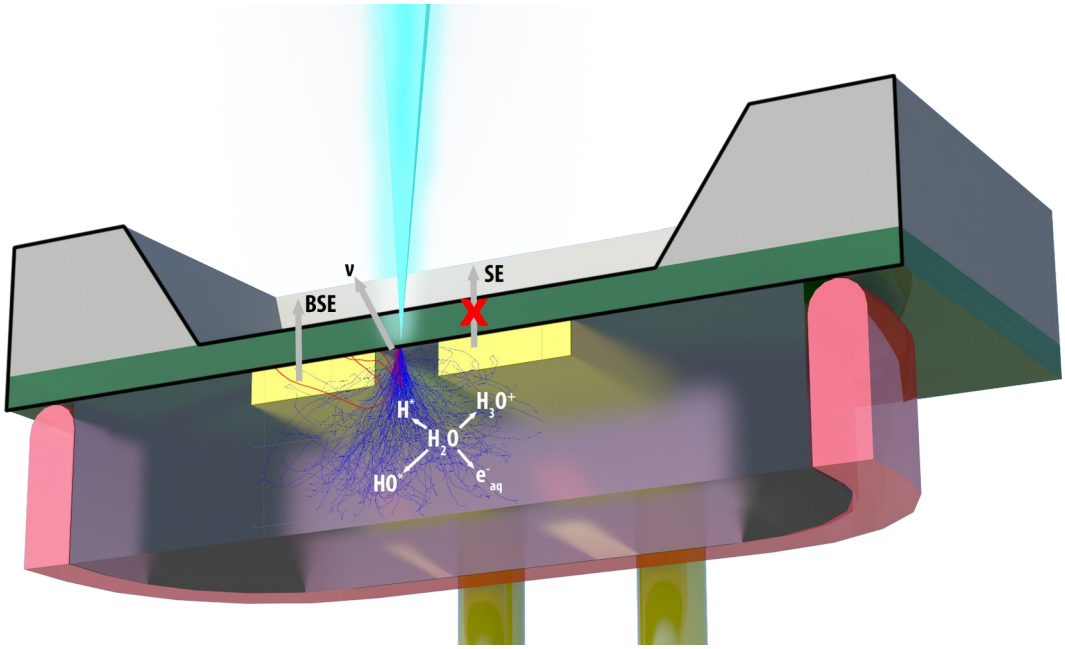

Figure 1.1: Artistic rendition of the EC-SEM system showing the microchip with two gold electrodes connected by the pins in the back, the PDMS gasket (red) and electrolyte. Because secondary electrons have too short a mean free path they are unable to traverse the membrane, which limits the detectable signal to backscattered electrons and x-rays greater than a few hundred eV. The electron beam can cause the electrolyte to decompose, here illustrated with some of the radiolytic products of water.

In this thesis there will be a focus on characterising the beam induced radiolytic processes that occur during electron microscopy (Figure 1.1), specifically the splitting of water in aqueous solutions into long-lived species such as H_2, H_2O_2, O_2 and others; changes in electrolyte conductivity by charged long-lived and transient species introduced by the beam; and finally beam-induced reduction of copper ions to nanoparticles from an electroplating solution of sulfuric acid and copper sulfate.

Why perform electrochemistry in-situ electron microscopy

Electron microscopes offer a very high resolution compared to their conventional optical counterparts, being able to resolve down to the ~5 nanometer-scale, and for some transmission electron microscopes as far down as beyond the atomic lattice (50 pm) for suitable samples. In-situ experiments eliminate sample preparation steps between different treatments of a sample, such as before and after electroplating. In the case of electroplating, such steps may dislodge the nucleation

seeds if they are not well adhered, damage a porous structure or even etch them away if left in a corrosive solution for too long. Similarly, when investigating battery materials a significant sample degradation can be seen if steps are not taken to avoid exposure to ambient air and moisture (Figure 1.2). With in-situ electron microscopy such sample transfer is not necessary.

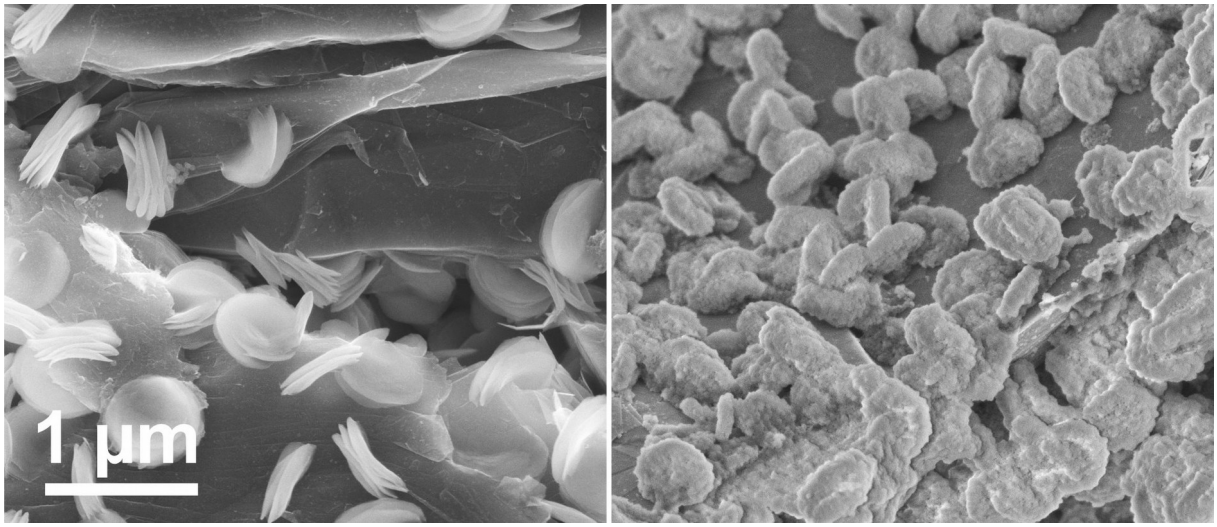

Figure 1.2: Example of sample degradation upon exposure to air. Both figures show Li_2O_2 toroidal structures[x] which were formed on graphite cathode during discharge of a lithium-oxygen cell. But where the left sample was exposed to air for less than a minute the right sample was exposed for 24 hours. The changes in toroid surface quality are thought to be mainly due to ambient moisture. Differences in the size of the structures is related to the discharge conditions (identical scale). Gamma adjusted for clarity. Electrochemical discharge performed by Ali Rinaldi.

*[x] For a description of the peculiar morphology of Li_2O_2 see Mitchell et al. Growth. J. Phys. Chem. Lett. **4,** 1060–1064 (2013).*

In-situ allows one sample to be tracked through the experimental treatment. When performing measurements on a large number of representative samples variations between the individual samples might be larger than the change induced by the experiment. This is not a problem if a specific sample – e.g. the same set of particles – is identified before, during and after: The change can be directly observed.

Some electrochemical processes are more suitable for in-situ electron microscopy because the electrochemical change gives rise to a change in observable contrast. In most cases the contrast mechanism used for in-situ experiments is Z-contrast, which originates from the difference in atomic number (Z). This means that there are some electrochemical processes that are more suitable for in-situ electron microscopy studies than others, such as different types of heterogeneous (electro-)chemical reactions:

- Corrosion, which often results in pitting and localised dissolution which can be resolved by the electron beam.
- Battery materials, which often exhibit volume change or changes to the crystallography. Electron microscopy can be used to see how cracks are formed in anode materials during charging as volume increases. These cracks lead to pulverisation during discharge.[1] In-situ electron microscopy is one way to image the root cause of expansion during charging and

link it to the degradation during discharge.

- Fuel cells, in which the active catalytic particles can agglomerate or in other ways be degraded. This change in nanoparticle distribution (both number and size) is visible in electron microscopy.
- Electroplating, where the creation of a new phase on top of the electrode is easily discernible and which conveys information about how the quality of the plating depends on electrolyte and plating conditions.

In-situ electron microscopy combines the high resolution and analytical capabilities of an electron microscope with electrochemical processes in liquid. It avoids some types of wrong conclusions because sample preparation steps that degrade the sample are avoided. Processes that are particularly suited for in-situ analysis cause a visible change in contrast, such as a change in particle size, or alternatively a change in composition to include either a higher or lower content of high atomic number atoms.

State of the art: in-situ combinations of electron microscopy and electrochemistry: SEM vs TEM

The idea of studying liquid processes and electrochemistry in electron microscopes is not new – it was first demonstrated in 1944 – but encapsulating the liquid to prevent desiccation and at the same time obtain high resolution has traditionally been impractical.[2] With recent advances in thin-film electrodes and encapsulation it has become possible to perform a lot more in-situ experiments, and there is now a need to understand the beam-induced effects.

A lot of focus has been dedicated to various implementations of in-situ TEM electrochemical cells,[3,4] in part due to the promise of very high resolution which a TEM can provide under ideal circumstances. But because TEM cells have to be extremely compact to fit in the TEM holder it is a recurring problem to include a proper electrochemical reference electrode. In this thesis an SEM is used instead of TEM in part because it includes a more stable reference electrode, which is necessary to quantify the beam-induced effects. To better understand how beam effects studied in SEM can be used to make predictions for TEM it is necessary to describe the current state of art for both SEM and TEM techniques.

An open cell is the simplest form of electrochemical cell because it does not make use of any form of encapsulation. Instead it exposes the sample directly to the vacuum of the microscope (Figure 1.3), which is possible when using a solid electrolyte. Such a cell has been used to study the lithiation of silicon when brought into contact with metallic lithium, where the native oxide on the lithium acted as the electrolyte.[5]

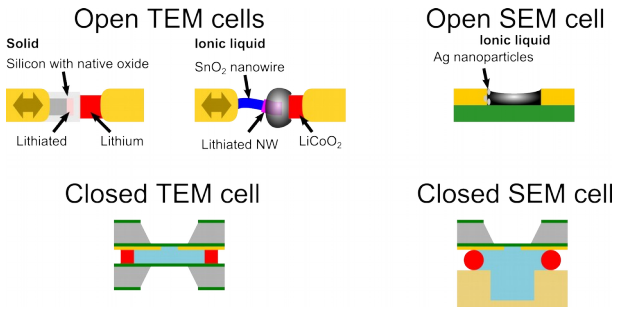

Figure 1.3: In order to study electrochemical processes in an electron microscope it is necessary to maintain microscope vacuum. With the use of micromanipulators it is possible to use either solid electrolytes or vacuum-compatible ionic liquids. In order to study aqueous and other conventional electrolytes it is necessary to have a closed cell which encapsulates the liquid.

In order to have a liquid electrolyte in an electron microscope the vacuum has to be secured by some means, and one way to ensure that is to use a liquid with no appreciable vacuum pressure (Figure 1.4). Room temperature ionic liquids fit that description, and when mixed with a lithium salt they are able to operate in lithium-ion cells. An example of such a battery cell isan open TEM-cell with an ionic liquid as the electrolyte where the lithiation of SnO_2 nanowires was studied.[6] One issue with such cells is that they rely on mechanical manipulation inside the TEM to combine the two parts of the cell and to pull it apart again for imaging. An open cell for SEM has also been made that takes advantage of the low vapour pressure of ionic liquids, where three electrodes were used to demonstrate nucleation of silver by electroplating.[7]

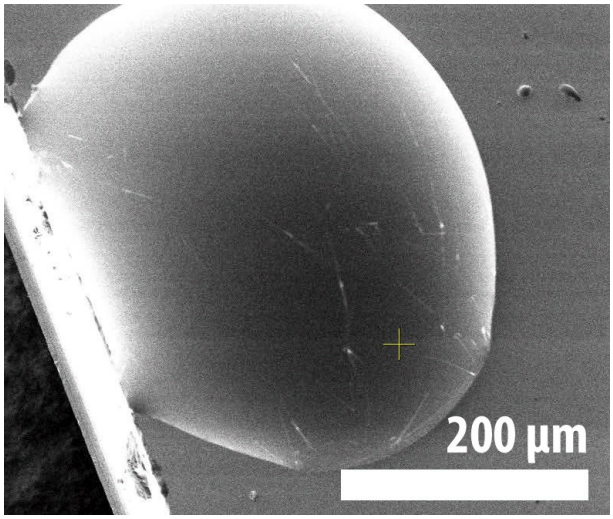

Figure 1.4: Some ionic liquids have a UHV-compatible vapour pressure. Here is a droplet of ionic liquid on the edge of a silicon chip in a conventional SEM. The bright fibres in the liquid originated from the paper used to blot away excess liquid, and were seen to float around independently when irradiated.

Conventional electrolytes, whether aquatic or organic, require an encapsulation in order to not dry out and contaminate the microscope in the process. One of the first liquid SEM cells that was demonstrated used a piece of polyimide as a membrane to encapsulate water and used backscattered electrons to record a usable signal.[8] A method that has proven popular in more designs is the use of silicon nitride membranes, which can be prepared by common microfabrication techniques.

Currently there exists both SEM and TEM devices that use silicon nitride windows for the encapsulation. SEM devices only need vacuum on one side, and by using a silicon nitride membrane Nishiyama et al. combined a high-vacuum SEM side with an atmospheric optical microscope-side on the same sample.[9] Devices which can be used in a TEM can be made by bonding two silicon wafers with opposing electron transparent windows of silicon nitride. In this way it is possible to create a vacuum-proof encapsulation which enable the study of aqueous or other challenging electrolytes.[10–12]

The common microfabrication techniques used to prepare the silicon nitride windows also allow for the integration of thin-film electrodes and other features. Systems for TEM are currently commercially available from at least three vendors; both Hummingbird Scientific (USA) and Protochips, Inc. (USA) have liquid cells featuring two opposing microchips which are kept at a specific distance by means of a spacer-layer and sealed off with O-rings.[13] In addition DENSSolutions (the Netherlands) have recently launched a product dedicated to liquid encapsulation.

None of the commercial TEM systems have integrated reference electrodes. In practice this can be worked around by forming a pseudo-reference electrode in devices with at least 3 electrodes. But because such electrodes may not always be sufficiently stable, and because they share the electrolyte completely with the irradiated volume they are not preferable when studying radiolytic effects.

In SEM-systems there is enough room to include a proper reference electrode. Currently it is only possible to buy SEM-adaptations of TEM systems, with little improvement in available reference electrodes. Instead this project uses instead the microchip-based system presented by Jensen et al. Compared to the preceding cells this system allows for multiple individual working electrodes on a chip, a dedicated proper reference electrode (Ag/AgCl-based) and a Pt-wire counter electrode.[14]

Techniques used to prepare samples for in-situ electron microscopy can of course be adapted for use in other characterisation tools, such as x-ray photoelectron spectroscopy which also requires a vacuum and a very thin encapsulation. One such example is the use of a polysilicon membrane to obtain an XPS-measurement of the core-electrons, which was used to quantify the electrochemical formation of SiO_2 where the silicon membrane was in contact with the water electrolyte.[15]

In summary, silicon nitride can be used to form electron-transparent windows which encapsulates liquid electrolytes. Devices for electrochemistry can be made by including thin-film electrodes on the windows. TEM devices are very limited in space, which prevents the inclusion of proper reference electrodes. Such constraints are not the case for SEM, which makes the SEM-cell a better choice for studying complex electrochemistry.

Radiolytic effects from the perspective of electron microscopy

In electron microscopy charged electrons are used to probe the sample in a very small region, either with a focused rastering beam (SEM and STEM) or with a homogeneous irradiation to form an

image (TEM). The electron beam causes some of the electrolyte to decompose in a process called radiolysis. Although radiolytic effects have been studied in relation to nuclear energy, there are many open questions relating to the environment in in-situ liquid cells because the radiation dose and intensity is extremely high. In the following paragraphs the essential building blocks for understanding radiolysis are explained.

Introduction to radiolysis

Radiation with sufficient energy is ionising, meaning that it can remove electrons which are tightly bound to an atom. Many will be familiar with the three most commonly mentioned forms of ionising radiation, originating from either radionuclides or accelerated particle beams:

1. Alpha-radiation in which helium cores with high kinetic energy are ejected in a fission process.
2. Beta-radiation resulting from a neutron splitting into a proton and electron – and where the resulting electron is ejected with high kinetic energy. Beta-radiation can be studied in accelerated electron beams, such as those in electron microscopes.
3. And finally gamma radiation, which is how a nucleus can return to its low-energy from an excited state (e.g. caused by nuclear decay) by sending out a high energy photon.

The difference between radiation from radionuclides and electron microscopy is that although radionuclides have higher individual particle energies at around ~MeV, the sustained intensity obtained in the focused electron beam can be several orders of magnitude higher.

The electrons in an electron microscope have more than enough energy to break chemical bonds: Typical acceleration voltages are on the order of 10^3 – 10^5 eV, while molecular bonds are on the order of 10^0 eV. Due to the very intensive research into nuclear physics with applications in energy production, weapons and medical purposes in the 1960's we have a good idea of what happens when for example water is struck by ionising radiation: In a process called radiolysis water molecules are broken up and recombined in a series of steps to form many different new radicals and molecular species containing hydrogen and oxygen, such as $H^{\bullet}$, H_3O^+, H_2 and H_2O_2.[16]

Elliot and McCracken presented a collection of more than 70 chemical reactions with rate constants for radiolytically split water. This set illustrates the many permutations and pathways radiolytic products of water can follow as the transient species recombine to the longer lived radiolytic products.[17] The purpose of their study is to predict the radiolytic reactions in the fusion tokamak ITER[a] based on existing pulse-radiolysis studies.

Although this is the most comprehensive overview of radiolytic reactions we have, it is important to note that the radiation intensity in ITER is expected to be at least 4 orders of magnitude lower than

a A tokamak is a device in which plasma is confined by a toroidal magnetic field. The goal with ITER is that this confined plasma will undergo nuclear fusion. As this is essentially the inside of a nuclear reactor the radiation intensity will be very high by most standards, yet still very low compared to the focused beam in electron microscopy.

in electron microscopy cells.[17] The authors emphasise that experimental results are needed to verify the exact outcome. This caution is even more prudent when extrapolating the results over many orders of magnitude in order to predict the radiolytic conditions in electron microscopy.

Schneider et al. modelled the concentration of different radiolytic species in an in-situ TEM cell during irradiation by applying the set of equations presented by Elliot and McCracken.[18] According to their prediction H_2 and H_2O_2 are the main detectable radiolytic species at low pH-values (Figure 1.5). It is worth noting that although radiolytic H^+ is formed, it is the initial pH that is the most significant driver behind the increasing H^+ concentration with decreasing pH.

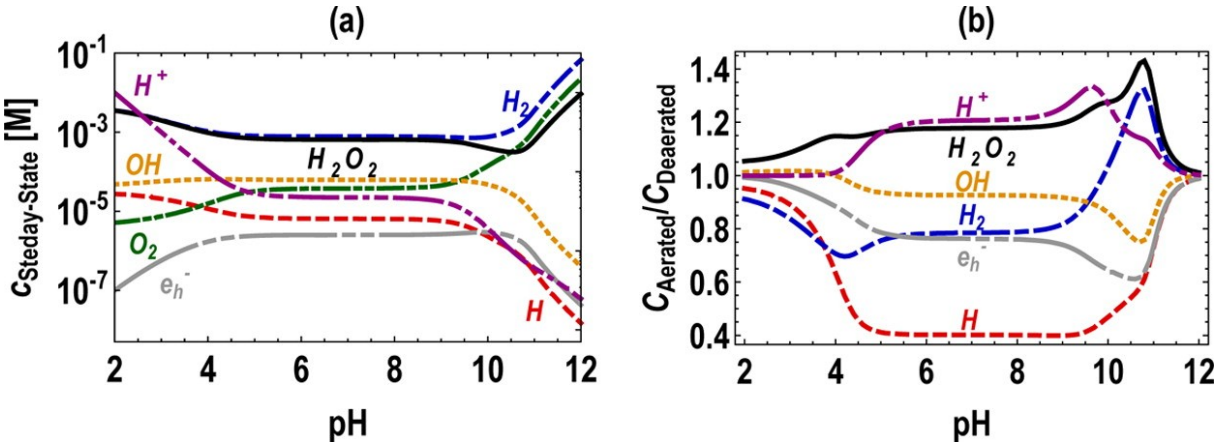

Figure 1.5: Expected steady-state concentrations of radiolytic products within the irradiated spot as a function of pH before the experiment. This plot assumes a typical irradiation intensity for a small TEM cell. (Schneider et al. 2014)

Formation of radiolytic bubbles and precipitation of metal particles due to radiolytic beam influence was documented in TEM experiments by Grogan et al.[19] Woehl et al. presented a review of some of the many challenges associated with liquid TEM, including sealing issues and window bulging. They also discuss the radiolytic splitting of water during STEM irradiation and demonstrate the reduction of residual traces of gold precursor to gold crystals due to the beam influence.[20]

In their discussion of radiolysis issues applying to in-situ cells Woehl et al. concludes on the basis of Caër's review that >35% of the primary radiolytic products is hydrated electrons, exceeding that of species like H_2.[16,20] Woehl et al. further predict that acidic solutions will inhibit the formation of hydrated electrons due to the recombination with readily available H^+. Although Schneider et al.'s simulations agree that hydrated electrons should recombine at low pH they predict that e.g. H_2 should have a much higher concentration. This discrepancy might be attributed to Schneider et al. calculating the many ways in which the many products react to combine into a set of final radiolytic products, but nonetheless highlights that there is a need to experimentally verify the conditions in which in-situ liquid cells operate.

Many different radiolytic effects have been observed and predicted. The predictions are based on experimental conditions relevant for traditional nuclear research, which means that the typical radiation intensities are several orders of magnitude less than what the focused electron beam

delivers in electron microscopes. It is therefore necessary with experimental data in electron microscopy-conditions to verify the validity of existing predictions.

Dosimetry

An important aspect of quantifying radiolytic effects is to have an accurate measure of the dose to which one can normalise the observation. While it is often possible to estimate or calculate the radiation dose based on the energy of the incoming beam, there are experimental cases where an experimental measurement is needed instead. One example is pulse radiolysis which is one of the more common ways to determine the radiolytic yield per radiation dose. In order to correctly quantify the radiation dose contained in the radiation pulse the radiation intensity is determined experimentally.

Radiation intensity is often described in the unit Gray per second (Gy/s), which is a measure of the amount of energy absorbed per mass of solution per time (1 Gy/s = 1 J/[kg·s]). 1 Gy/s is equivalent to approximately 6 keV/[μm^3·s] in water. The intensity in electron microscopy depends on many factors described later, but is often much more than 10^6 Gy/s.

Fricke dosimetry is one of the most established methods of determining the radiation dose. It is a chemical dosimeter consisting of a solution of sulphuric acid and $FeSO_4$ (or some variation thereof). The dissolved Fe^{2+} is oxidised by the electron beam to Fe^{3+}, which induces a colour change that can be quantified. This change is linear for low doses, but for high doses the dissolved oxygen in the solution becomes depleted, and the sensitivity drops. Depending on which variant of the solution in use the maximum measurable dose is between 350 and 2000 Gy.[21] The response remains linear up to approximately 2 MGy/s, above which the sensitivity drops rapidly.[22] As will be discussed in detail in chapter 3 neither of these are sufficient for use with electron microscopy, where typical sustained doses are on the order of 100 MGy/s. As a result the maximum dose would be reached in tens of microseconds.

Despite its shortcomings for electron microscopy, the Fricke dosimeter has been very important to establish the yield of the radiolytic products of different solutions, water included. During electron microscopy the dose is estimated based on the energy-dependent ability of the beam to traverse the sample, combined with measurements of the beam current.

How exactly is the radiolytic yield commonly measured – and are such measurements representative for electron microscopy?

When discussing radiolysis it is impossible to avoid a discussion of the radiolytic yield, that is to say the number of molecules of a specific type produced per 100 eV the beam deposits into the electrolyte. This property, called the g-value, is commonly measured by means of pulse radiolysis. It is in part based on the g-value that it is possible to predict which effect the electron beam will have on various electrolytes.

The g-values of alpha and beta particles usually entails a linear accelerator which sends a short pulse of high energy particles into the electrolyte. The exact duration of the pulse varies with the

capabilities of the available equipment, but some sources cite pulse lengths on the order of 10^{-7} – 10^{-5} s.[23,24]

Although high transient beam currents of 10^{0} A can be seen, the large spot size (10^{-3} – 10^{-2} m) means that the localised dose rate does not reach levels comparable to electron microscopy.[25] Even more so, because of its transient nature pulse radiolysis has a very low total dose compared to the continuous high radiation intensity an electron microscope deposits into the liquid: Where pulse radiolysis uses single pulses of ~10^{0} Gy, electron microscopy is usually not less than 10^{5} Gy/s continuous (further details discussed in chapter 3).

Individual species can be detected in different ways. Many, such as the hydrated electron, H and OH radicals can be detected by optical spectroscopy.[26–28] OH can be detected by its gaseous reaction products when a suitable electrolyte is purged with oxygen gas. Radiolytic oxygen can similarly be detected by bubbling the solution with argon and passing the gas over a selective electrochemical sensor.[29] Radiolytic changes in conductivity can be measured electrochemically, for example by biasing the electrochemical cell and looking at the current transient formed by the irradiation pulse.[25]

With the advances brought on by silicon microfabrication techniques it is now possible to create microdevices with integrated electrodes to measure the radiolytic yield. In a device similar to the encapsulation for SEM Liedhegner et al. demonstrated the detection of radiolytic oxygen and hydrogen peroxide by means of a thin silver electrode on a suspended silicon carbide window.[30] The electrochemical detection was performed by observing the change in current at fixed potential bias, and the radiolytic g-value for hydrogen was calculated based on the observed values for oxygen and hydrogen peroxide.

Historical measurements of g-values have been essential when current models for radiolytic effects have been formed. But because there is a large difference in the radiation intensity and dose between the pulse radiolysis experiments traditionally used, it is not given that these historical measurements scale up to the radiation intensity levels in electron microscopy.

Are published g-values representative for focused electron beam microscopy (SEM/STEM)?

In literature g-values vary significantly with electrolyte composition, radiation type and energy, and measurement technique. It is worthwhile to outline some of these measurements because the majority of the measurements which are used to form predictions for electron microscopy conditions are recorded at very low intensities.

Different radiolytic species have different g-values: Christensen and Bjergbakke list g-values at very low dose rates (<10^{-3} Gy/s) for various products of water in the range of 0.1 to 2.8.[31,32] The extrapolated the g-value for H_2O_2 by Burns and Sims to a 25 kV electron beam dissipated in 10 µm deep water is approximately 0.7.[29] At the same time their g-value for HO_2 is vastly lower, in the

range 0.01 to 0.3. G-values for the most common radiolytic products under traditional radiolytic conditions are thus typically on the order of 10^{-2} to 10^{0}.

Le Caër sketches up three stages in the generation of radiolytic products (Figure 1.6),[16] (1) ionisation and relaxation during the first femtosecond; (2) a physico-chemical stage (1 femtosecond – 1 picosecond) in which a number of transient species are generated by splitting of the excited molecules; and (3) a chemical stage (1 picosecond – 1 microsecond) in which the transient products diffuse and react with other species in the same irradiated track. With a beam current of 0.2 – 1.0 nA the time between individual electrons is nominally 1 – 0.1 nanosecond, which precludes recombination at the physico-chemical stage, but may affect effective chemical reaction rates and equilibrium concentrations in the chemical stage. It is worth noting here that the solvated electron survives into the beginning of the chemical stage.

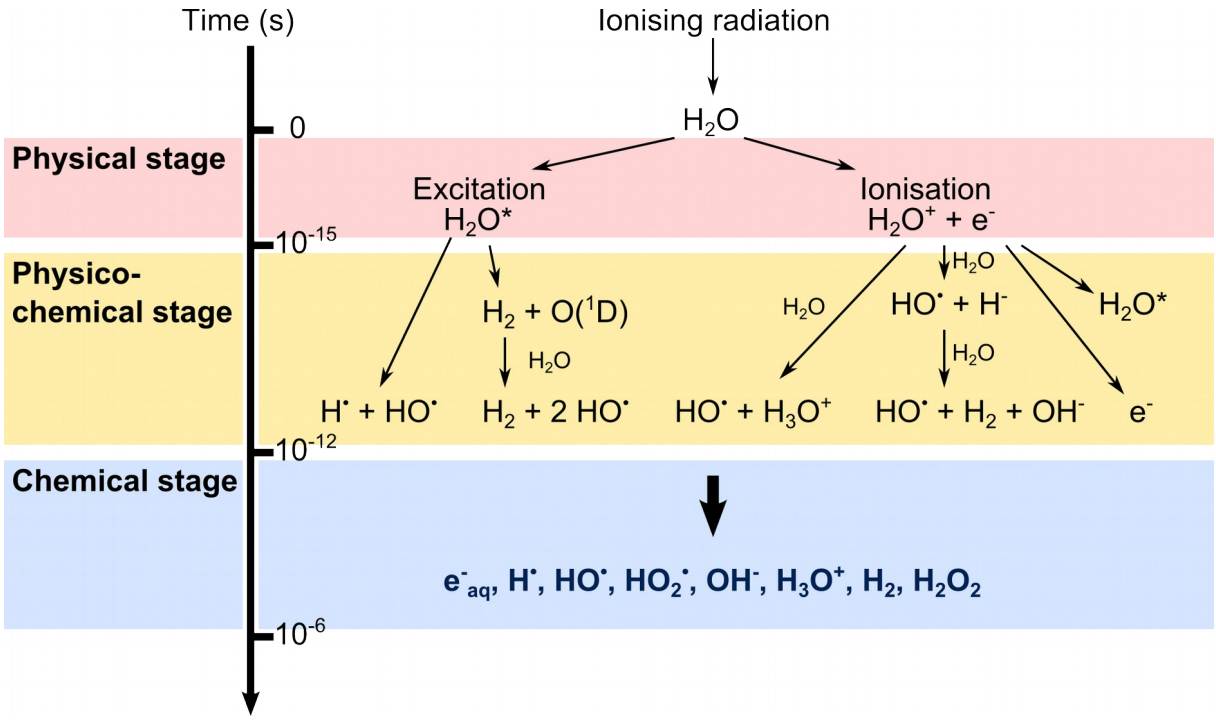

Figure 1.6: The three stages of water radiolysis sketched out by Le Caër. The physical excitation and ionisation leads to a cascade of molecule destabilisation and recombinations. At the end of the chemical stage only some of the longer lived species remain, which continue to react and recombine beyond 10^{-6} s. Figure adapted from Le Caër (2011).

Unlike pulse radiolysis, the continuous high-intensity irradiation in an electron microscope may promote recombination because of the high number of radiolytic products created in the same location. This effect is even more prominent in a scanning microscope because the beam remains focused in the same spot for ~10^{-6} s. In this time radiolytic product is not able to diffuse very far: Different chemical species differ in their diffusion constants, but using OH^- as an example a 1 nanosecond diffusion time corresponds to a characteristic distance of 3 nanometers, and 1 microsecond 80 nanometers.[33]

The diffusion distance over the course of one microsecond is similar to the beam spot size after passing through the silicon nitride membrane. For a thermionic emission SEM looking through a nitride membrane it is likely that the beam size is on the order of 25-50 nanometers. Even with a well-tuned field emission microscope the spot size is not likely to be much smaller than 5-10 nanometers due to the influence of the silicon nitride membrane. Because of the high irradiation intensity there is a high concentration of radiolytic products formed in this spot, increasing the probability of recombination before the species diffuse far enough away to become long-lived species. As a result of this recombination it is reasonable to expect lower radiolytic yields, g-values, in electron microscopy than in pulse radiolytic measurements.

Problem formulation and thesis outline

In-situ electron microscopy provides a technique that allows electrochemical systems to be studied with a resolution otherwise not available. This is particularly interesting in applications such as electroplating and battery materials, since the quality and performance of such devices depend on the nanostructure.

But one of the key issues with current in-situ electron microscopy studies is the influence of the electron beam, which despite obvious evidence of its ability to affect experiments has not been quantified directly. Current predictions are based on measurements of radiolytic yields at irradiation intensities many orders of magnitude lower than the sustained irradiation in electron microscopy. The higher irradiation intensity is likely to cause changes in the radiolytic yield, and may also cause changes in the relative concentrations of radiolytic species.

In order to continue with electrochemical experiments in-situ electron microscopy it is important to fully understand the radiolytic environment so that the beam effect can be correctly compensated for during both the experimental stage as well as during data analysis. But TEM cells are limited by their small volume, are finicky to use and have a limited set of electrodes without a proper reference electrode capability. They are therefore not ideal for measuring radiolytic effects.

In-situ SEM differs from in-situ TEM in the versatility offered by the larger chamber volume. Our cell, initially developed by Jensen et al.,[14] includes a dedicated reference electrode and an array of working electrodes. In this work I use different material choices for the working electrodes depending on the electrochemical process, and take advantage of the reference electrode included in the system in order to elucidate the influence of the electron beam on electrochemistry in the following ways:

1. *How does the electron beam affect the electrolyte composition?*
   Schneider et al. presented a model of the radiolytic environment in TEM, based on conventional pulse radiolysis.[18] How accurate are their predictions? By measuring how the electron beam affects the electrolyte composition it will be possible to tell if historical measurements for radiolysis are still valid for electron microscopy.
2. *How does the electron beam affect the electrolyte conductivity?*
   Radiolysis forms ionic species which change the ionic strength of the electrolyte, which can

affect many electrochemical systems by e.g. providing a pathway for corrosion, changing double layer thickness and more. But despite the increasing interest in performing electrochemistry in-situ electron microscopy we do not yet have experimental measurements of the beam-induced changes in electrolyte conductivity.

3. *How does radiolysis affect electrochemical metal deposition? How much metal is reduced radiolytically by the beam?*
   Electroplating is a popular topic to study with electron microscopy because the plating quality is in part determined by the initial nanometer-sized seeds, and because metal particles with high atomic numbers are readily visible with electron microscopes. In order to benefit from in-situ studies of electroplating it is important to understand in which ways the beam influences electrodeposition. The high visibility of metal nanoparticles in electron microscopy also means that such particles serve as a good quantitative measurement of the radiolytic yield of metal ions converted to metal, allowing the g-value to be compared to traditional pulse-radiolysis measurements.

My work in addressing these questions is described in the chapters 4, 5 and 6, respectively.

Some background information and theory is applicable to all of the three experimental studies. This information is provided in the following two chapters:

Chapter 2. An introduction to electrochemical measurements and a discussion of the peculiarities of in-situ electrochemistry.

Chapter 3. In-situ electron microscopy: Moving beyond the historical overview presented in this chapter, chapter 3 offers a technical discussion of the differences between in-situ SEM and TEM, and an introduction to the cell and devices used for the work in this thesis. Here I also present the fabrication of an improved device with carbon electrodes which can sustain higher potentials than thin-film gold electrodes.

Finally, the work is summed up in chapter 7, where an outlook is provided together with the proposition of a few additional adaptations of the present studies to better link results from SEM and TEM together.

Chapter 2: The basics of electrochemical measurements

In this work electrochemical measurements are used to quantify radiolytic processes. The same techniques used for quantification of radiolysis may also be affected by the electron beam when they are used to quantify electrochemical processes. In the following chapter the basics of electrochemistry is presented in order to understand the electrochemical methods needed for the experimental measurements. This chapter also discusses the equipment used to perform electrochemical measurements, the potentiostat, because the electron beam acts as an additional current source not taken into account in most electrochemical literature.

Electrochemical reactions

Many important chemical reactions are *redox*-reactions, where the oxidation numbers of the involved elements are different after the reaction has taken place. One example could be the formation of rust on steel, where the iron changes oxidation state from Fe(0) to Fe(+III).

Electrochemistry is the term used for reactions where the electrons participating in such a redox reaction takes a separate path from the ions, and electroplating is a perfect example of this: A positive potential is applied to the anode, e.g. a copper wire, which causes copper atoms to change from a metallic state, Cu(0), to an ionised state, Cu^{+2}. These copper ions are dissolved in the electrolyte, for example water in which a copper salt is already dissolved. A negative potential is applied on the cathode, which causes copper ions to return to a metallic state where they are in contact electrode. To make this possible Cu^{+2} ions are conducted through the electrolyte, while simultaneously two electrons are conducted through a wire and power source between the anode and cathode. This separation of ionic path and electrical path is the crux between traditional redox reactions and electrochemical redox reactions.

The electrochemical reactions take place on the surface of the electrically connected electrodes and in contact with the electrolyte. It then follows that the rate of the reactions may be limited by the electrical connection; by the depletion of active material and diffuse resupply, if for example electroplating is performed too quickly; or by the kinetics of the chemical reaction itself. How these different phenomena present themselves is essential to fingerprint the reaction that takes place.

The net electrochemical reaction is limited by the current through the electrical circuit. However, a constant exchange between the oxidised and reduced species is taking place spontaneously at the surface of the electrode at a rate described by the exchange current density. At equilibrium the anodic (e.g. dissolution) and cathodic (e.g. electroplating) currents are equal and the net current is zero. In the case of electroplating copper it means that the plated copper is constantly being simultaneously dissolved and plated, but since no net current is flowing the total amount of solid copper remains constant. A higher exchange current density corresponds to a faster electrochemical process which will lead to a lower electrode polarisation for a given net reaction rate. When a potential is applied the net current describes the difference between the anodic and cathodic current.

When an electrode is in contact with an electrolyte the charge in the electrode (whether positive in the form of holes or negative in the form of electrons) is screened by ions in the liquid which take place in the immediate vicinity of the electrode. The electronic charge in the electrode and the ionic charge in the electrolyte form a double layer, very much like a capacitor. In the case where the potential of the electrode is changed the resulting current is a superposition of the transient rearranging of the double layer (charging of the capacitor) and the faradayic reaction (electrochemical reaction).

The electrochemical cell

In order to measure accurately the contribution of one particular electrode it is common to have electrochemical cells with three electrodes (Figure 2.1): The working electrode (WE), which either contains or interacts with the material one is interested in; a reference electrode (RE) through which (ideally) no current passes, and against which the potential of the WE is measured; and an auxiliary electrode called the counter electrode (CE) which is used to drive the current to a level where a suitable potential between the WE and RE is achieved. It does this by forcing a current to run between the WE and CE in the direction needed for the measured potential to match the command. In another mode it can also be used to drive a specific current, in which it is the potential that is the property which is measured.

Measuring the potential between the working electrode and reference, as compared to between WE and CE, has a few very important advantages: First, it means that the polarisation of the counter electrode needed for any given current does not falsely affect the potential reading of the WE. Second, with a small RE close to the WE the ohmic voltage-drop through most of the electrolyte can similarly be cancelled out. Lastly, the reference electrode is usually chosen such that it has a known absolute potential, for example with respect to the standard hydrogen electrode (SCE). A known absolute potential is essential in order to identify the specific reaction that takes place.

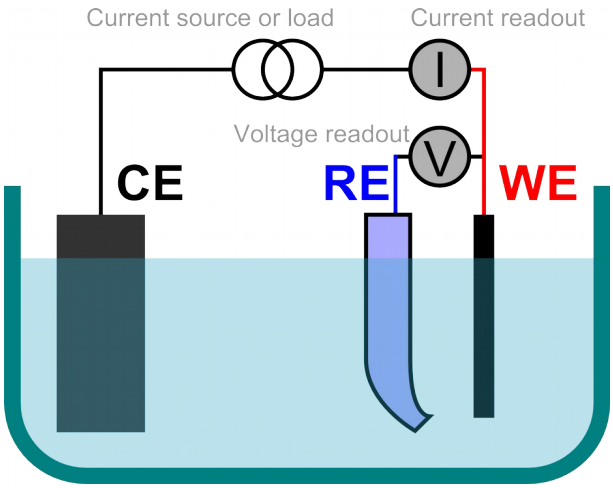

Figure 2.1: A typical electrochemical cell has three electrodes: The main electrode, called the working electrode (WE); its potential is measured against the reference electrode (RE); and a counter electrode (CE) to make a complete circuit through which current can flow.

Electrochemical measurement techniques

There's a plethora of different electrochemical measurement techniques and variations of them. However, there are three that stand out in particular as especially common and which are used extensively in the following:

- Open Circuit Potential (or -Voltage)
- Chronoamperometry and chronopotentiometry
- Cyclic voltammetry

The open circuit potential, OCP, measures the stable potential between the working- and reference electrode when the counter electrode is disconnected. Consequently there is no net current flowing, although depending on the material a small or large exchange current may take place on the surface of the electrode. OCP is often used to determine the state of charge in a battery, or to determine if there is a change in the surface chemistry or if the system is in equilibrium. It often precedes other techniques as validation that the conditions of equilibrium are met, and to determine the DC bias needed to stay in equilibrium.

Chronopotentiometry is similar to OCP; it measures the potential of the WE with respect to the RE while a fixed current is being forced through the WE to the CE. If this current is set to zero it is – within the precision of the control loop – the same as OCP. The technique is often used e.g. to characterise batteries at a fixed rate of charge or discharge. Chronoamperometry is similar, but here current is being measured at a fixed potential. Many (gas) sensors operate in this mode, where the presence of certain species gives rise to a current proportional to the concentration.

Cyclic voltammetry is a technique widely used to identify the presence of specific active species, as each redox-couple has a characteristic set of potentials for oxidation and reduction. By sweeping the potential linearly in one direction, then immediately after sweep it back (a full cycle) it is possible

to deduce the presence of active species, which potential they are active at, and whether there are other relevant reactions (e.g. purely chemical reactions which consume reaction product).

Potentiostat operation when irradiating with e-beam

During normal operation the potentiostat controls the potential between the working- and reference electrode by introducing a current through the counter- to the working electrode. During open circuit potential measurements the counter electrode is disconnected, and the working electrode is measured with respect to the reference electrode.

When performing experiments in an electron microscope there is the issue of the beam injecting charge into the cell. This charge must be dissipated by leading it to ground to prevent build-up of high potentials and erroneous data being recorded from non-faradaic capacitive effects and discharges. Some of the problems associated with charging include degradation of cell components, image distortion, membrane failures – and potentially also damage to the potentiostat if not correctly grounded.

Under normal circumstances most potentiostats have the cell grounded through the working electrode. In this configuration the cell is only conditionally safe from overvoltage resulting from accumulating beam charge, as it requires the potentiostat to be connected and turned on to be sure that no charge is being accumulated and the computer ground should be connected to earth.

It would be preferable if the cell was unconditionally safe – i.e. that there is an electrode that is always connected directly to ground. However, attempts to operate the potentiostat in floating mode with a grounded counter electrode proved that this was not possible, as the potentiostat became excessively sensitive to interference and no clean image could be recorded on the SEM. The only configuration that proved satisfactory was with the WE grounded normally with the potentiostat ground connector connected to the SEM chassis, which is in turn grounded to the building's safety earth.

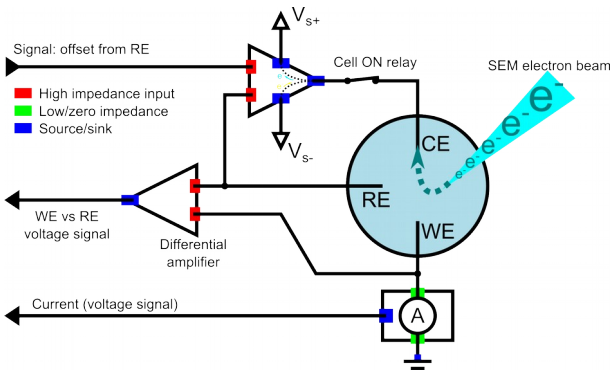

Figure 2.2: Schematic of potentiostat operation during electron beam irradiation. Active regulation of the working electrode current ensures that the electron beam current is deflected to the counter electrode. During normal open circuit potential measurements the electron beam current would inevitably end up as a faradayic reaction through the working electrode, violating the principle of an OCP measurement.

The schematic of a typical potentiostat in Figure 2.2 illustrates how to overcome this issue in a system irradiated with an electron beam. As stated, it is common convention to ground the working electrode through the ammeter (which either works by measuring the voltage over a resistor, or – in the case of virtual ground/zero-resistance ammeters – by a feedback loop). When measuring the OCP under normal circumstances the working electrode is in equilibrium with the electrolyte and there is no net current through the electrode, while the counter electrode is disconnected by means of a relay.

During normal operation, for example during chronoamperometry (a digital/staircase CV can be viewed as a series of such measurements), the potentiostat is set to apply a potential on the counter electrode which drives a current between the working and counter electrode. The magnitude of this potential is adjusted to drive a current such that the measured potential between the working- and reference electrode reaches the potential V_{set} set in the technique (could e.g. be +0.7 V for chronoamperometry). Depending on the V_{set} potential the counter electrode can either source or drain any current needed. After a short time to settle the potentiostat reads out the magnitude of the current and stores it in the data file. In galvanostatic mode this signal is also used as part of the control loop.

The important realisation is that the net current is being sourced/drained to GND through the working electrode, and at the counter electrode the current is obtained from the amplifier source/drain supply voltages which enable the counter electrode to be regulated up to V_{s+} and down to V_{s-} to meet the target V_{set}.

When an electrochemical cell is set up in an SEM there is an additional source of electrons which is injected into the cell regardless of whether the cell (i.e. CE) relay is ON or OFF. In an OCP measurement the working electrode is no longer in equilibrium since the electron beam current is being drawn to ground, something the potentiostat does not correct for.

To avoid this issue chronopotentiometry with a very low current range is used to measure the open circuit potential. The applied WE current is set to zero, and the potentiostat actively regulates this by monitoring the ammeter that connects WE to GND. During this regulation the CE potential is adjusted so that the net beam current is sunk there without affecting the WE.

Chronopotentiometry may not be as precise as true OCP, since the accuracy of applied potentials is lower than if it is just measured (<2 mV for Ivium CompactStat), and because the actual applied current depends on the current resolution (current range). During testing we used a current range of 100 nA (resolution 13 pA) on an electrode which had a typical CV peak current of 1-2 µA, which provided a signal to noise ratios suitable for the experiments.

During cyclic voltammetry there is not the same concern of which path the injected electrons will take, since the current needed to polarise the WE with respect to the reference electrode is correctly measured, and it does not matter if the current is sourced by the electron beam or the CE. Should the electron beam exceed what is needed the CE will sink as much as is needed.

Chapter 3: In-situ electron microscopy

Although the term in-situ electron microscopy is starting to become well established, there are some caveats. In some instances “in situ SEM” has been used to describe experiments where samples are treated electrochemically in one cell, after which the sample is rinsed and transferred to an SEM. The sample is then moved back and forth, enabling the same particle to be studied at various stages of treatment.[34,35] Such a technique also goes by the name “identical location electron microscopy”.[36]

Having a liquid sample inside the electron microscope and perform electrochemistry on it directly was believed to be impossible due to the requirement of high vacuum.[37] However, effective encapsulation in the form of electron transparent silicon nitride membranes has overcome this obstacle.[3]

The following chapter will explain the basics of electron microscopy as well as the important differences between SEM and TEM, followed by a thorough description of the EC-SEM system and the improvements introduced during this project. The description of the improved electrodes has been submitted to Microelectronic Engineering, and is included here in its original form.

Description of Transmission Electron Microscopes

Since Ruska initially invented the electron microscope[38] the use of such microscopes have expanded from originally being used to study metal films,[39] to more diverse samples such as changes in crystallinity due to temperature,[40] organic (life) samples such as the archetypical T4 virus,[41] cross-sections of integrated circuits,[42] gaseous catalysis processes,[43] and – of particular interest in this thesis: in-situ electrochemical measurements such as batteries.[6]

This thesis is mainly concerned with in-situ SEM because this cell allows for a more stable reference electrode and a greater number of working electrodes. But because most of the prior

results have been obtained in a TEM, and because results obtained here are potentially of significant impact also for TEM it is necessary to outline the essential parts of both types of microscopes, as this illustrates to what extent results from one can be relevant for the other.

Basic construction of a TEM

A TEM is built up very much like a light-microscope, consisting of the following main sections (Figure 3.1A): First there is the “gun” in which electrons are obtained either by heating a filament or by field emission, or a combination of the two. An extraction voltage aids in this process, and the electrons are then accelerated with an additional acceleration voltage until the desired kinetic energy has been reached. Typical acceleration voltages are between 80 and 300 kV, with typical beam currents on the order of 0.1 – 10 nA.

Second is the condenser optics which ensures a homogeneous and coherent illumination of the sample. It typically consists of several electromagnetic lenses and apertures and optionally with aberration correcting optics. The apertures can be used to reduce for example chromatic and spherical aberrations which would otherwise reduce the quality of the illumination. Using such an aperture would simultaneously reduce the current which reaches the sample, which depending on the application may be an advantage in itself. The stigmatism of the condenser optics can be tuned to ensure a circular illumination of the sample. Finally there is the last condenser lens which determines the diameter of the electron illuminated area, and thus the current density.

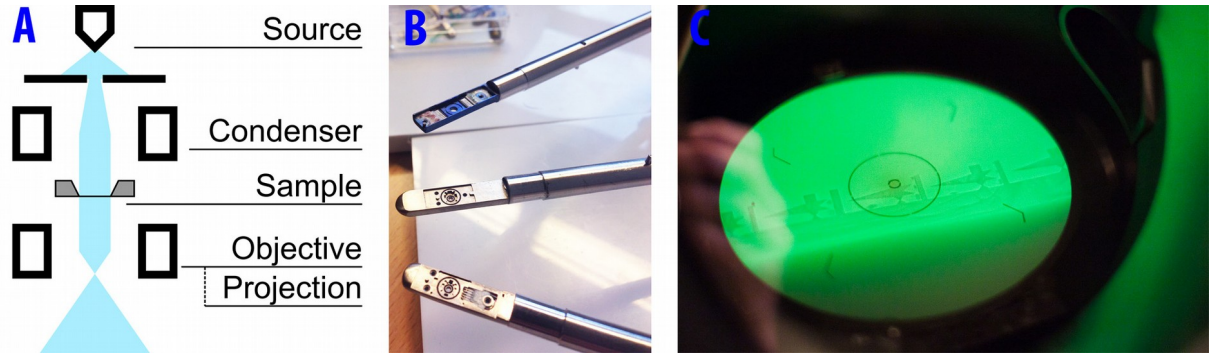

Figure 3.1: A: Simplified schematic of the optics in a TEM. A homogeneous irradiation strikes the sample. By focusing the objective lens on the sample an image can be projected onto a screen below. B: Three variations of modern chip based TEM-holders (designed, built and photographed by Murat Yesibolati). C: The projected image can be visualised by means of a phosphor-screen at the bottom of the TEM. Here a set of MEMS devices being characterised by Alexey Savenko.

Between the condenser lens and the next element – the objective lens – there is a narrow gap in which the sample is placed. In today's TEMs the sample holder which fits in this gap is of very high importance. Traditional TEM holders consist of a metal tip in which a 3 mm diameter disc, typically called a grid due to its support structure, can be placed. More modern TEM holders, however, allow for liquid and electrochemical TEM to be performed. This is possible because of liquid and electrical feed-throughs, as well as a means to contain a liquid cell typically comprised of two chips and O-rings (Figure 3.1B).

After the sample there is the objective lens and projection optics. It is the combination of the objective lens – which forms a virtual image of the specific region of interest, i.e. controls the magnification – and the projection optics which take the virtual image and projects it onto the camera or phosphorescent screen (Figure 3.1C). As is the case for the condenser optics, it is also necessary to tune the objective lens stigmatism.

Irradiation in TEM and radiolysis of electrolyte in liquid samples

When imaging in a TEM the electron irradiation is homogeneous over the entire region of interest defined by the condenser lens, and each successive electron strike the sample at a random location. Between electrons there is a temporal gap on the order of 10^{-10} s, which is such a short time that typical species with diffusion coefficients on the order of 10^{-5} cm^2/s have spread less than 1 nm.

Le Caër stated that physical processes such as ionisation and physico-chemical processes such as decomposition of excited molecules happen at timescales less than 10^{-12} s.[16] Between 10^{-12} and 10^{-6} s chemical reactions (including recombination) take place along with diffusion into the bulk.

The higher the relative amount of overlap, the higher the amount of recombination. A higher amount of recombination would likely mean that the literature values for radiolytic yield differ from the experimental condition in the TEM. In order to determine the extent of overlap in 2D for a thin sample between successive electrons in relation to the time-scale presented by Le Caër it is necessary to set up an equation which finds the probability of an electron striking an area which does not contain any radiolytic species. This equation also represents an important difference between TEM and SEM, since in SEM and STEM the electron beam is directed to the same spot for an extended time. The final expression in Eq. 3.4 can be obtained by combining the following expressions:

By dividing the electron charge, q_e, by the beam current, i, we obtain the typical time between individual electrons. The total time, t, is the time per electron multiplied with the number of electrons – minus one, so that the first electron constitutes t=0:

$$t = (n-1)\, q_e\, i_{beam}^{-1} \tag{3.1}$$

Because of diffusion (diffusion constant D) the circular area affected by radiolysis from a specific electron (A_{single}) increases with time, here described by using the characteristic diffusion length as the radius.

$$\begin{aligned} A_{single} &= \pi D t \\ A_{single} &= (n-1)\pi D q_e i_{beam}^{-1} \end{aligned} \tag{3.2}$$

If one assumes zero overlap between the affected areas the probability of an electron hitting the unaffected area is simply one minus the ratio of affected area (summing up the area each specific electron has affected) to the total area (i.e. the beam spot size, $A_{beam} = \pi \cdot r^2_{beam}$). The total time is here dictated by the total number of electrons in the sequence, N.

$$\begin{aligned} P_{single} &= 1 - \frac{A_{TotAffected}}{A_{beam}} \\ P_{single} &= 1 - \frac{\sum_{n=1}^{N} A_{single}}{A_{beam}} \\ P_{single} &= 1 - \frac{\sum_{n=1}^{N} \pi (n-1) D q_e i_{beam}^{-1}}{\pi r_{beam}^2} \end{aligned} \tag{3.3}$$

The probability that every single electron in the sequence hits an unaffected area, the compounded probability, can be expressed by multiplying together the probabilities for each successive electron. In this equation *m* is used to describe the total number of electrons *so far*, until it reaches the total number of electrons in the sequence, *N*.

$$P = \prod_{m=1}^{N} \left[1 - \sum_{n=1}^{m} \left(\frac{(n-1) D q_e i_{beam}^{-1}}{r_{beam}^2} \right) \right] \tag{3.4}$$

In reality this formula underestimates the probability of *N* electrons in a row hitting an unperturbed site for two reasons: It does not consider any overlap between past spots and it does not consider that some of the radiolytically affected area is outside the region of interest. However, since the probability function drops off very rapidly due to compounding probability these errors are not sufficient to alter the conclusion, and at any rate, the equation gives a reasonable lower bound on how many electrons are needed.

Using typical numbers, such as a diffusion constant of 10^{-5} cm^2/s, 1 nA current, and a beam diameter of 2 µm we find that it takes 430 electrons for the compounded probability of each electron hitting a new area to fall to 50%. Far more is of course needed for a given electron; it takes 4400 electrons before the probability that an electron strikes an unaffected area drops to 50%, but at that time the compounded probability is infinitesimal. While 4400 electrons correspond to 700 ns, 430 electrons are reached in 70 ns. In both cases the time is much longer than 10^{-12} s, which places them in the chemical regime between 10^{-12} and 10^{-6} s.

The energy transfer from the electron beam to the liquid is determined by the thickness of the liquid layer and its *stopping power.* Since most TEM chips to date have had thick liquid layers due to large spacers and bulging a reasonable thickness to make calculations for is 1 µm. This is so thick that the additional 2x 50 nm from the nitride membrane can be ignored. For electrons accelerated to 300 keV the stopping power of water is 236 eV/µm, or approximately 0.1% of the beam energy in a 1 µm sample.[44] Because TEM samples are so thin and because the energy loss is so low relative to the incoming beam one may assume that there is no change in stopping power as the beam traverses the sample and thus that the energy is absorbed evenly.

$$I_{rad} = \frac{S(E)\, i_{beam}}{A_{beam}\rho} \tag{3.5}$$

Because such a small amount of the energy is absorbed the equation to calculate the radiation intensity absorbed by the sample reduces to Eq. 3.5, where I_{rad} is the absorbed intensity in Gy/s (equivalent to W/kg); $S(E)$ is the energy dependent stopping power of the medium, here water; i_{beam} is the electron beam current; A_{beam} is the irradiated area (i.e. spot size); and finally ρ is the density of the electrolyte, which for water is 1000 kg/m^3. Using this equation and factoring in a 1 nA current hitting a 2 µm region of interest this equates to 75 MGy/s, a number used by Schneider et al. and others for radiolytic calculations.[18]

Summary

Transmission electron microscopes are image-forming microscopes used with samples that are thin enough that essentially the entire beam is transmitted. The sample is irradiated homogeneously in a selected region by the condenser optics, and the objective- and projector optics produce a magnified image on a screen or image sensor (e.g. CCD). Acceleration voltages are typically high, for example 100 – 300 kV, which reduces the stopping power of the sample sufficiently for the beam to pass through the sample.

Such microscopes are currently being used for in-situ liquid electrochemical experiments Although TEMs are known for being able to attain very high resolution, liquid samples often have problems with sample thickness due to the encapsulation which adds thickness and which may bulge to increase thickness even more.

Irradiation intensities are high, for example 75 MGy/s in water, depending mainly on the beam current and irradiated area. Because electrons strike the sample at random locations within the irradiated region it can be calculated how many electrons (or how long time) there is between the same area, which for the same typical parameters end up being 300 electrons. As a consequence the individual spurs in which radiolysis can occur operate in the chemical regime.

Description of Scanning Electron Microscopes and STEM

Scanning electron microscopes contain only the top half of the TEM – the part which precedes the sample. Here the electrons are extracted, accelerated and condensed to a very small spot – the probe. Microscopes with field emission filaments are typically able to obtain a higher resolution due to a smaller probe size. Such microscopes are also often fitted with in-lens electron detectors and may use shorter working distances, both of which results in a higher collection efficiency which in turn makes it easier to tune the beam in cases where the irradiation intensity has to be kept low (whether that is required e.g. to attain high resolution, or because of concerns of beam damage and radiolysis).

In connection with the objective lens in the SEM – which is essentially creating a focussed spot from the demagnified image of the virtual electron source – the microscope has a set of scanning

coils.[45,46] These deflect the beam and create the on-screen image by rastering across the region of interest. Except for some edge effects which depend on the quality of the scan-generator electrons only irradiate the region of interest. Also of note is that the electron dose is not distributed evenly and randomly as in the TEM, but rather each pixel receives its entire dose before the beam moves on to the next point.

Scanning Transmission Electron Microscopes (STEM) are often conventional TEM microscopes where the condenser optics focus the electron beam to a very small spot, and where there is a scan-generator which can raster this spot across the sample just like an SEM. However, since such microscopes require thin TEM samples and are typically operated at TEM acceleration voltages (10^5 V) which are much higher than typical SEM acceleration voltages (10^4 V) most of the beam current passes through the sample, just like a normal TEM.

Detector types

There are three types of detectors that are relevant to this thesis: The Everhart-Thornley Detector (ETD) for secondary electrons, a traditional backscatter detector (BSD), and finally the FEI Large Field Detector (LFD) for detection of secondary electrons in environmental SEM (E-SEM) (Figure 3.2).

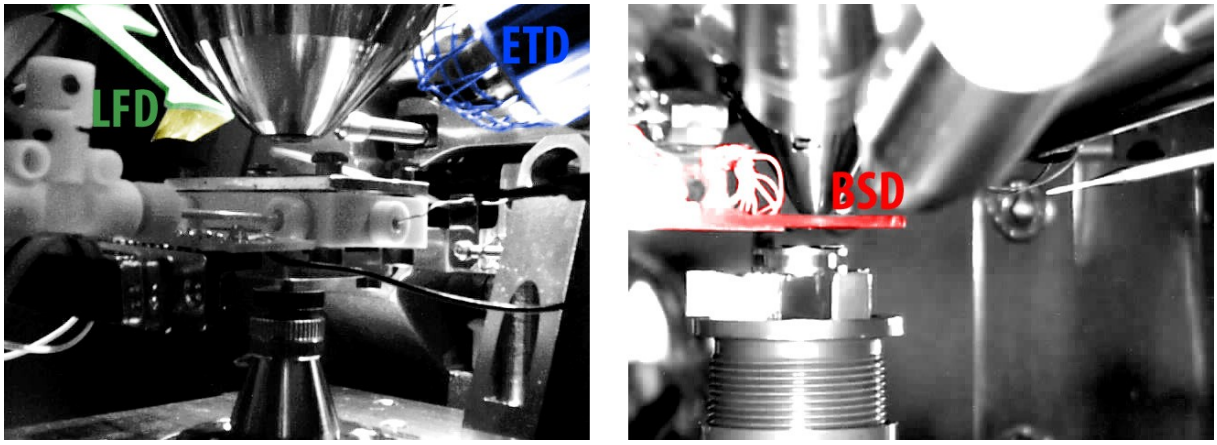

Figure 3.2: Left: Image of an SEM chamber during an experiment with the electrochemical liquid cell. The ETD is the conventional secondary electron detector used in high vacuum. The LFD detector is a gaseous electron detector which detects the amplified signal resulting from the collision cascade of electrons passing through the water vapour present in low-vacuum mode. Right: On this microscope the backscatter detector is inserted when needed, and is positioned such that it closely surrounds the pole piece in order to maximise collection efficiency.

The ETD is one of the most commonly used secondary electron detectors, and is typically placed in one of the sides of the SEM chamber where it is outside the direct path of the beam, but still with an unobscured line of sight to the sample. It functions by applying a small attraction voltage on the detector. Since secondary electrons have a very low energy, below 50 eV, they are collected at the detector where they can be detected by means of a scintillator. On the microscopes in use here the ETD-detector is only active in high vacuum.

Edges in the geometry of the sample are able to emit more secondary electrons than flat surfaces. When combined with a side-mounted ETD this results in images with highlights and shadows coming from edges that are facing towards or away (respectively) from the sensor, giving a familiar look from which it is easy to interpret the geometry. Charging and other effects may alter the shading, much like different materials can alter the brightness of surfaces in a photo (Figure 3.3).

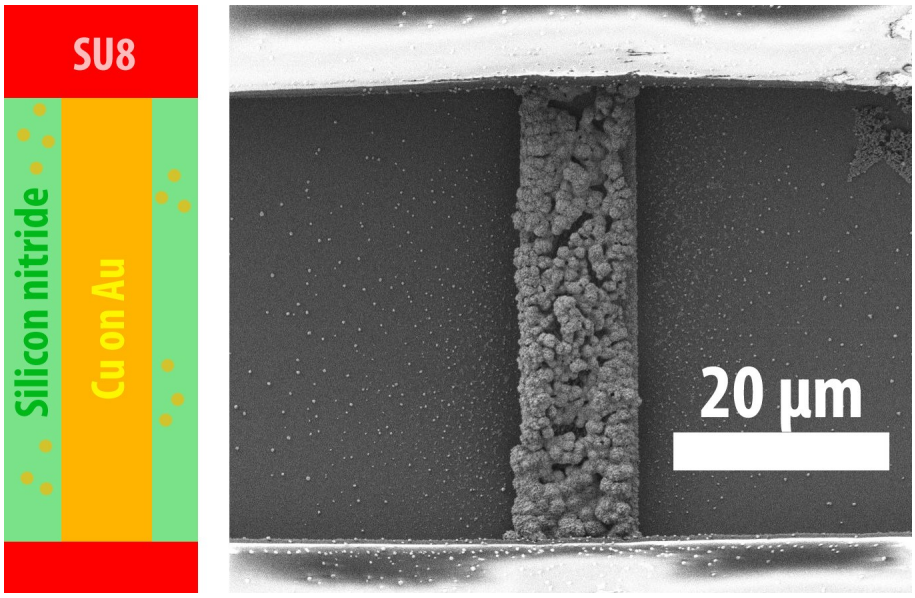

Figure 3.3: Image of an electrode after electroplating of copper. The acceleration voltage of the microscope was tuned to minimise charging effects such as severe drift and image distortion, but some such effects remain visible in the non-conductive SU8. Shadows and highlights indicate that the detector (ETD) is positioned to the top-left. Small structures such as the fragments that surround the electrode have an exposed surface surrounding the particle, which increases the escaping (i.e. detectable) yield of secondary electrons.

Backscattered electrons can be detected by means of a semiconductor detector placed either inside the pole piece or just around it. They can be biased to a negative voltage to repel secondary electrons, since SE have a lower energy than backscattered electrons. One of the main contrast mechanisms for a backscatter detector is the atomic number, and as such backscattered electrons are particularly suitable to distinguish light vs. heavy elements.

For liquid studies in SEM E-SEM mode is often used because the water vapour in the chamber helps reduce charging on the outside surface of the liquid cell. Such charging may lead to burst membranes.[14] Since a significant secondary electron signal cannot traverse the silicon nitride membrane it is the backscattered electrons which contain interesting information. Normally the FEI Large Field Detector (LFD) is considered a gaseous secondary electron detector. But since the LFD detects the cascade resulting from an electron ionising the gas in the chamber only electrons exceeding 10-20 eV contribute.[47] Secondary electrons (defined as electrons with less kinetic energy than 50 eV) in this energy range have a mean free path on the order of 0.5 to 5 nm, much too short to escape the silicon nitride membrane.[48] It has already been reported that backscattered electrons take part in this ionising cascade, converting the backscattered electrons into detectable secondary electrons by interacting with the membrane, amorphous carbon or water vapour.[49]

Beam rastering, and the applicability of TEM simulations of radiolysis for SEM

To date the analysis on radiolysis for in-situ electron microscopy has been considering typical TEM conditions. The even irradiation in the entire exposed region is vastly different from the rastering electron beam in an SEM, which delivers an extremely high irradiation intensity for a very short time, then proceeds to irradiate the next pixel until all pixels have been irradiated and the cycle starts over. In an SEM the entire beam energy is absorbed, and because of this there are also variations in absorbed dose depending on depth, unlike a TEM. Because of these significant differences a thorough description of the conditions in an SEM is required before comparing to the published estimates for TEM.

Not only is the energy of the beam absorbed in an SEM, the current itself is as well. This differs from a TEM where the current passes largely uninhibited through the sample. Although the absorbed current makes it necessary to make some adjustments to how the potentiostat is used, it does not greatly affect the radiolysis. Because the g-value for the hydrated electron is 2.6 per 100 eV, a 25 keV electron causes the formation of 650 hydrated electrons. Since the radiolytic electrons outnumber the added charge by almost three orders of magnitude it is reasonable to expect that the charge from the primary electron is dissipated via any grounded electrode in the cell, without constituting a significant change in the electrochemical condition relative to the TEM.

The simulations by Schneider et al. of TEM radiolysis take into account the conditions of a bright field TEM, in which a 2 µm wide electron beam of 1 nA at 300 kV irradiates a 1 µm thick sample of water through which 99.02% of the electrons are transmitted. This is very different from the conditions typical in SEM where a 25 kV rastered spot is fully absorbed by the liquid. And yet, by carefully looking at the assumptions made for the simulations we find that they can be extrapolated to also describe the SEM.

The source code for the simulation has been made freely available,[18] and it is based on the G-values, i.e. yield of radiolytic molecules per 100 eV energy per electron, which do not change significantly in the range between 1 kV and 1 MV for the different species involved.[50] Apart from these parameters the simulation makes use of pH and the dose rate in Gy/s – deposited power (J/s) per kg of solution.

Despite the differences in how the dose is achieved the SEM and TEM case can be compared since the radiolytic yield is linear with dose,[51] and since pulse- and steady state radiolysis are not treated differently when studying long-lived radiolytic products.[26]

For the TEM simulations Schneider et al. find that within the 2 µm irradiated region the final radiolytic product concentration is reached in about 1 ms, while it can take on the order of 10 seconds before their entire region of interest (50 µm diameter) has reached a stable concentration.

A rastering beam behaves differently to a conventional TEM, and one has to consider both the instantaneous local irradiation intensity and the frame-average. And because the SEM cell is much deeper than the penetration depth of the electrons there is a depth-variance to the intensity as well, as opposed to the very thin TEM cell that is assumed to be evenly irradiated.

To see how this compares to the SEM experiment we can consider three different cases: (1) The stationary and focused beam inside a single pixel, (2) an average over the entire frame being scanned, or optionally (3) a defocused SEM beam to simulate brightfield TEM imaging conditions.

The first depends on how well focused the beam is and including scattering in the 50 nm nitride membrane, the focused beam size is probably on the order of 25 nm based on the highest resolution we can practically attain.

Case (3) was not experimentally tested as it is not representative of how an SEM will be used during imaging. Since case (1) only occurs for a very short time at any given spot, and since diffusion and recombination without the addition of further radiolytic products occur between individual exposures of the same pixel we shall consider case 2 in the following when we compare our SEM to the TEM simulations. This can likewise be compared to STEM when the beam is scanned such that the current per scanned area is equal to the conditions for the TEM simulations, i.e. 0.3 nA/μm^2, and for now neglecting details of raster pattern, dwell time and scan speed.

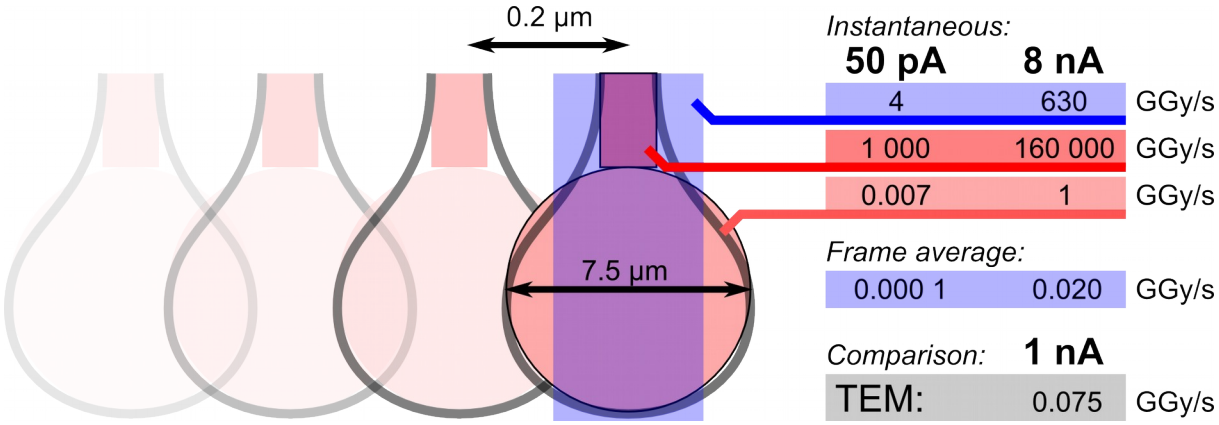

Figure 3.4: To estimate how the radiation intensity compares with TEM results from Casino-simulations were approximated as a straight cylindrical section and a sphere. The sphere, which is large enough to overlap several pixels, has an instantaneous intensity comparable to the TEM at low SEM beam currents, while the initial cylindrical region – which is only irradiated once per frame – is much higher. One can also look at the per-pixel average using a depth of 10 μm, which when performing a frame-average in the 40 μm x 25 μm region of interest records an average intensity 3.5x less than that of the simulated TEM conditions.

In SEM the entire beam is absorbed, and the depth it takes for this to happen defines the irradiated volume for determining the dose rate per mass [Gy/s]. A set of SEM CASINO simulations allow us to determine this teardrop shaped volume (Figure 3.4). Because the intensity of the dissipated power varies significantly within the volume we will section it to get a clearer picture of the localized intensity. From Figure 3.4 we can see that as the beam enters the liquid the first 50% of the power is absorbed during the first 2.5 μm by the well-defined beam which is only weakly spread by

scattering, which we model as a cylinder. A more diffuse tail extends some 7.5 µm from this point in which the next 40% of the power is absorbed, treated as a sphere. The last 10% reach further, but do not affect the conclusion.

For comparison we consider the average intensity in each pixel, since the pixel spacing of 200 nm is much larger (>5x) than the actual ~25 nm focused beam spot size. The irradiated depth of each pixel is set to 10 µm, at which depth CASINO simulations of electron range show that >90% of the energy has been dissipated (Casino 2.48, 25 kV). It is worth noting that the majority of the energy is dissipated in the first few micrometers, and the ratio of beam energy which is dissipated beyond 6.5 µm is only 1/e.

25 kV SEM	50 pA	8 nA	[Gy/s]
Instantaneous			
Per pixel (100%)	10^{9}	10^{12}	
Cylinder (50%)	10^{12}	10^{14}	
Sphere (40%)	10^{6}	10^{8}	
Frame average			
Per pixel (100%)	10^{5}	10^{7}	
Cylinder (50%)	10^{7}	10^{9}	
Sphere (40%)	10^{2}	10^{4}	
Schneider TEM	10^{8}		

Table 3.1: Sphere and cylinder sections refer to the simplified schematic in Figure 3.4, and correspond to the volume in which first 50% and the following 40% of the energy is absorbed.

Due to the rastering motion of the electron beam in an SEM there is a large difference in the instantaneous radiation intensity and the frame-averaged, depending heavily on the scan parameters such as dwell time, frame size and magnification. The parameters indicated here are representative of the experimental conditions used for our electrochemical measurements. TEM is likewise affected by the image parameters, except that the beam irradiates the e.g. 2 µm *spot size homogeneously without rastering. In the simulation by Schneider et al. they assume a TEM cell irradiated with 75* MGy/s, *which for the current range we use is comparable to the instantaneous power in the big sphere (extending across ca. 40* px *in width), and the frame-averaged intensity for an average pixel.*

From Table 3.1 we see that the instantaneous intensity of the initial cylindrical section exceeds the 75 MGy/s in the TEM by several orders of magnitude. However, this cylinder has no overlap with neighbouring pixels as it is much smaller than the pixel spacing. Looking then at the time-average intensity (which depends on the number of pixels^{-1}, and in our case is based on a frame of 40 µm x

25 µm with a pixel spacing of 180 nm) we see that the lowest- and highest beam currents reach intensities below and above the TEM, and that a beam current of 250 pA would match it. We can treat the whole pixel average in the same way, and find that it is a factor of 4 below.

Below the high intensity region there is the wider spread of the beam. The frame averaged intensity in this region is much lower than the reference TEM-conditions, reaching an average 13 kGy/s for the 8 nA beam conditions. However, this region is so large that it overlaps with the neighbouring 20 pixels in either side. This overlap means that the frame averaged value underestimates the actual intensity. If this overlap is instead used for the average (each sphere corresponds to 5% of the frame area) a more representative value is 0.12 MGy/s to 20 MGy/s depending on current.

In summary, TEM irradiates the sample homogeneously in the exposed region with individual electrons striking randomly in the exposed region and with a constant energy loss through the depth of the sample. Actual intensity varies with e.g. beam current and the area of the condensed beam, but for a 1 nA current striking a 2 µm spot at 300 kV it would be 75 MGy/s. In SEM the entire energy of the beam is absorbed, and the absorbed energy differs with depth. Although the energy transfer is immense at the entry-region of the beam in the liquid, the average intensity an SEM sample receives when averaging over the time per frame is comparable in magnitude. Since pulse- and continuous radiolysis is treated similarly in literature the predictions by Schneider et al. can be considered valid for the SEM, and the results obtained in the SEM are relevant for irradiation in TEM.

EC-SEM – the in-situ cell and devices

About the device and holder

The EC-SEM system was originally designed and fabricated by Jensen to study electrochemical and liquid processes in an SEM.[14,52] For such a system the key requirements were (1) a form of encapsulation which separated the vacuum of the microscope from the liquid, (2) an electron transparent window, (3) electrical contact to the liquid, and (4) be suitable for electrochemistry – i.e. it should have a proper reference electrode.

At the time papers describing such systems as the nanoaquarium were being published,[12] which gave an early insight into how the requirements for in-situ cells are still approached today. A low stress silicon nitride membrane, in our case 50 nm thick and nominally 50 µm wide, serves as the encapsulation and electron transparent window. The holder itself (Figure 3.5) is made out of PEEK, a chemically resistant and machinable polymer, and serves as the reservoir and host of the counter- and reference electrodes. Between the microchip and the PEEK holder a PDMS gasket ensures a secure seal.

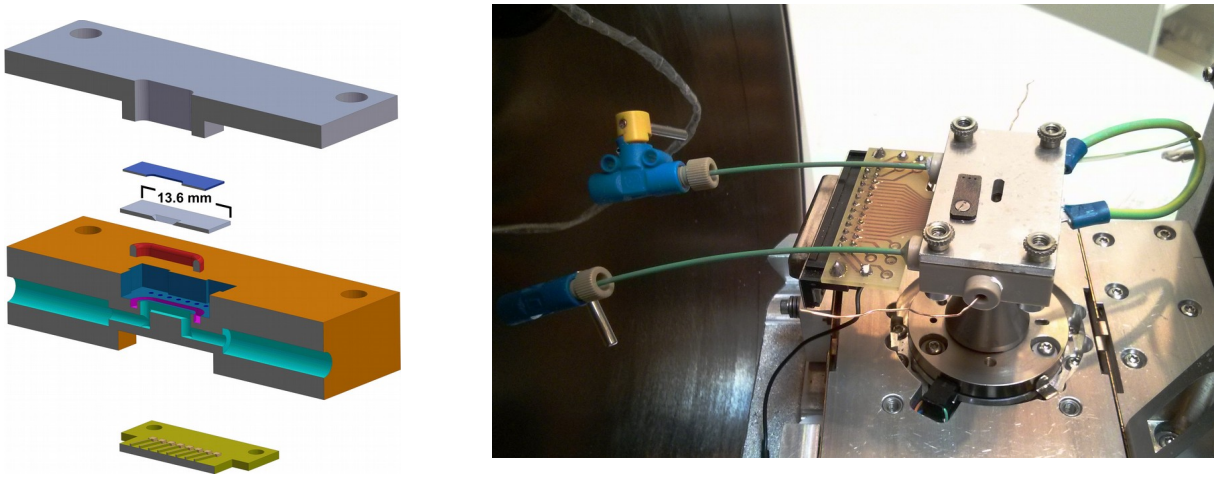

Figure 3.5: (Left): Cross-sectional view of the EC-SEM holder and chip system. An aluminium lid with a PDMS load-spreader clamps the chip firmly down on a PDMS gasket. A liquid chamber of PEEK combines the counter- and reference electrodes (side-mounted, not shown) into an electrochemical cell with the on-chip working electrodes. CAD drawing courtesy of Jensen. (Right): Typical configuration of the holder when installed in the electron microscope, showing the counter- and reference electrode out from the sides (for this experiment both are Cu-wires), and the two closed off tubes which serve as liquid inlet and outlet.

When configured for electron microscopy this cell is fitted with an aluminium lid which clamps down the chip.[52] An improved version of this lid was devised with a countersunk (conical) aperture to allow optimal illumination for dark-field optical imaging, with the sidewalls painted black to reduce glare (Figure 3.6). Most likely this change has also improved the collection efficiency of backscattered (and backscatter-induced secondary) electrons when used in the electron microscope as well, since such electrons are no longer being captured and conducted to ground by the lid.

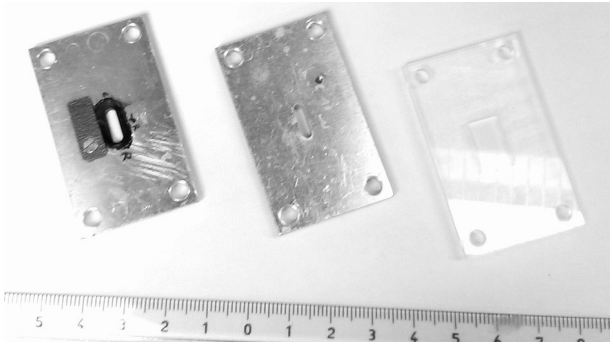

Figure 3.6: The original lid (center) provided good clamping of the chip and prevented charging in the SEM. The acrylic lid (right) was used to improve illumination in light microscopes, but resolution was limited due to glare. A conical cutout (left) with dark sides to eliminate glare provided an optically clear path to the chip, and is also believed to have increased collection efficiency of backscattered electrons in the SEM because of the geometry of the LFD detector.

Original and improved chip design

The original design inherited by this project (designated “v. 2”) has some key features: A silicon wafer serves as the base, on top of which the 50 nm silicon-rich nitride is grown. As is often the case, a KOH etch removes the silicon to form a suspended membrane. Metal electrodes are patterned on top of the nitride, and although gold (with an adhesion layer of titanium) is most

commonly used, this project has made use of such devices with both platinum and copper electrodes. In order to accurately quantify the electrochemically active area, and to ensure that electrochemical processes are confined to the observable region a layer of SU8 cross-linked photoresist is used everywhere except on the external contact pads and on the membrane.

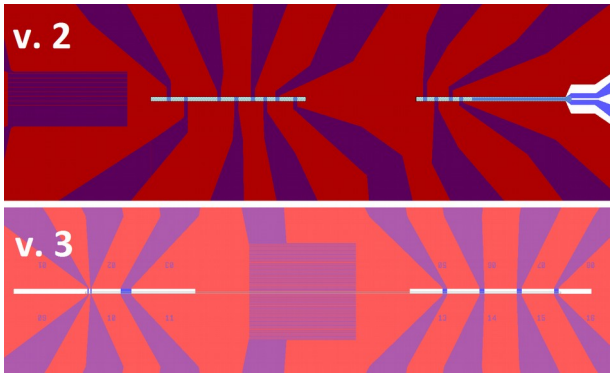

Figure 3.7: Different iterations of EC-SEM chips. The new design (v.3) contains electrical outputs for sense-connections on every electrode. In this way more accurate potential control is ensured, as well as the possibility to detect connection errors. Spacing within the meander structure has been increased to improve lift-off, and the individual electrodes have electrode numbers both on- and off membrane (only off-membrane can be seen at this resolution). The v3-design was co-developed with Jensen.

Besides some convenience features such as individual chip ID to track samples and microscope-visible electrode IDs, the new revised version 3 chips (Figure 3.7) improves the previous design in the following ways: First, every chip contains a miniature 3-electrode cell similar to TEM-chips. This is an excellent proving ground to develop experiments and enables e.g. custom on-chip reference electrodes to be calibrated towards a proper reference electrode, and also for their stability to be studied. Second, unlike the v.2 electrodes, each electrode is connected to two contact pads. This has the following advantages:

- Each electrode has a proper connection for the sense-electrode
- It is possible to test for continuity before performing an experiment, and thus rule out e.g. micro-cracks in the electrode
- Stress in the membrane is reduced, since electrodes are now placed symmetrically across the membrane

A sense electrode is an important part of the electrochemical cell. Like the four-point configuration for resistance measurements it allows the potential to be measured at the active part of the electrode, without any influence from the ohmic drop caused by e.g. poor contact resistance, cracks in the electrode and the resistive loss in the electrode itself. The latter is not of much relevance for a properly functioning metallic electrode (resistance ~10^0 Ω, current <10^{-4} A), but for e.g. carbon electrodes this may be of greater importance.

Being able to test for continuity is also of great value, since the spring-loaded *pogo pins* used for connecting the chip tend to corrode after some time. When they fail they often do so by

mechanically jamming, which in turn may result in a loss of contact. And even if not, then the corrosion itself often increases the resistance noticeably. Along the same line, the ability to test for continuity makes it possible to detect the presence of cracks in the metallic film which may be too small to detect by optical means. Such chips would otherwise be determined as fit for service, with possibly erroneous measurements being the end result.

Finally, the stress in the membrane is symmetric across the membrane, as opposed to the old design where electrodes stopped abruptly close to the edge. This should reduce the chance of the membranes breaking, since upon failure the observed crack sometimes weave from side to side indicating a very uneven stress (also in chips that have not yet been clamped).

Resolution

When performing electron microscopy of samples submerged in liquid the beam will be scattered by the liquid as well as the encapsulation (e.g. the silicon nitride membrane(s)). For this reason the maximum resolution attainable might be significantly lower than what the same microscope is capable of with dry samples.[3] When performing experiments in-situ SEM we generally expect that under ideal conditions with a suitable microscope the attainable resolution will be slightly better than the thickness of the silicon nitride membranes, such as a 100 nm resolution with 150 nm polyimide membranes in Quantomix capsules.[8]

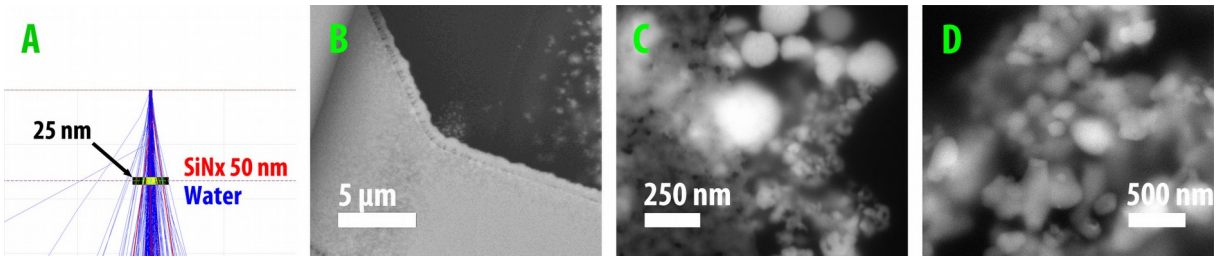

Figure 3.8: A: Casino simulation for a 1 nm *wide 25* kV *beam suggests that the majority of the beam has spread less than 25* nm *after passing through the 50* nm *silicon nitride membrane. This is an indication of the maximum resolution that is attainable with EC-SEM. B: In-situ copper electroplating with a tungsten filament SEM. The smallest copper particles are 100* nm *or less. (FEI Inspect S) C: When a similarly electroplated electrode is looked at after washing and drying – but sill through the membrane – with a high resolution field emission SEM much smaller structures are visible, here ~20* nm*. Working distance for this image was more than 9* mm*, similar to what is currently needed for the EC-SEM cell to not touch the pole piece. (FEI Quanta FEG 200) D: When particles of $LiFePO_4$ in a droplet of BMIM-BF_4 ionic liquid are likewise imaged through the membrane the smallest resolvable features are again 25* nm *or less. (FEI Helios)*

In-situ TEM is very sensitive to the entire thickness through which the beam is transmitted. Because of bulging the liquid layer thickness can become so thick that any inherent advantage that a TEM may have over SEM is quickly lost in practice. It is therefore not uncommon to see published TEM results where the resolution is on the order of tens of nm under typical circumstances.[53–56] Although we have not performed an exhaustive study on the resolution capabilities of the SEM system we have strong indications in the form of in-situ images that the resolution with a tungsten filament microscope (FEI Inspect) is on the order of or better than 100 nm when imaging copper structures in electroplating solution, and approximately 25 nm in a field emission-type microscope (FEI

Helios) when imaging $LiFePO_4$ particles in a solution of an ionic liquid (BMIM-BF4). In both cases it is reasonable to assume that the highest resolution is obtained by particles which are adhered to the membrane, surrounded by liquid (Figure 3.8). For samples imaged with FEG microscopes – whether that is dry samples without electrolyte or with an ionic liquid in place of an aqueous solution – we find that the practically attainable resolution closely matches what CASINO simulations would suggest.

Because the attainable resolution of the SEM system is very comparable to what is typically obtained with liquid TEM many of the studies which have been performed in-situ TEM could have equally well been performed in-situ SEM with all the advantages brought on by the more spacious chamber, such as proper reference electrodes, large area counter electrode, not to mention a less error-prone system where the risk of e.g. the sample drying out during the experiment is virtually eliminated.

Pyrolysed carbon electrodes on silicon nitride membranes with applications in electrochemical measurements in-situ electron microscopy

R. Møller-Nilsen, S. Canepa, K. Mølhave

Preface

An important aspect of in-situ electron microscopy is to be able to have suitable electrodes available. The electrodes are usually made by means of thin-film metal-deposition, and all it takes to get a new type of electrode is to exchange e.g. gold with platinum in the deposition process. Carbon electrodes are the de-facto standard in a lot of electrochemical processes because they are inert and have high electrochemical stability.

The following text describes the work performed to include patterned carbon electrodes in place of metal electrodes on chips for the EC-SEM system. This manuscript has been submitted to Microelectronic Engineering.

Abstract

Thin-film gold electrodes are often used in microchip systems in part due to their simplicity in fabrication, and in part due to the noble properties of e.g. gold. But such electrodes can rapidly degrade if they are used outside their stable potential window.

Carbon electrodes made by pyrolysis have already been demonstrated as good electrochemical electrodes, and are easy to pattern and fabricate. As such it is particularly well suited to chip-based electrochemical systems for e.g. in-situ studies in SEM and TEM. We find that pyrolysed carbon electrodes remain stable in dilute sulfuric acid at potentials at least 0.75 V higher than comparable gold electrodes. Despite an observed slow increase in electrode resistivity over months copper electroplating demonstrate reasonable electrical performance.

Introduction

In-situ electrochemical electron microscopy has been experiencing a significant increase in interest over the past few years[3] with applications in for instance battery research[54] with both users as well as commercial vendors making easy to use chip-based solutions to enable studies of complex processes with nanoscale resolution correlated with electrochemical measurements.[57] One key challenge is to have electrochemical electrodes that are both transparent to the electron beam and stable in a wide electrochemical potential range for the many varied applications the system can be used for, where some experimental conditions may cause normal lift-off patterned gold electrodes to fail.[58]

Carbon electrodes seem more robust than noble metal electrodes, such as the widely used glassy carbon electrodes for normal electrochemical cells, and the thin film carbon working electrodes marketed by some commercial vendors of chip-based TEM systems. One method by which to create carbon electrodes on a chip is by pyrolyzing an organic layer, which has been extensively studied as an alternative to glassy carbon electrodes for normal electrochemical cells.[59] Pyrolysis of photoresist is a particularly interesting method, since it allows microelectrode structures to be created with good pattern fidelity even after pyrolysis, as demonstrated by Larsen et al. on AZ5214E photoresist.[60] The process can be performed on wafer-scale and can yield electrodes with excellent electrochemical performance.[61,62]

Amato et al. studied the physical and electrochemical properties of pyrolysed carbon films extensively,[63] concluding that pyrolyesd carbon is an excellent material for electrochemical applications, although the material showed that the resistivity of pyrolysed carbon films increase in the days and months following pyrolysis. This degradation was attributed to contaminating adsorbents and a strong increase in oxygen content.

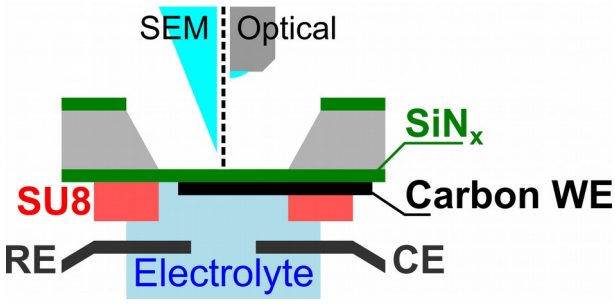

Figure 3.9: Cross section of the electrochemical cell.

A 50 nm *thin silicon rich nitride membrane serves as the transparent window in both optical- and electron microscopy. The chip has either carbon or Ti/Au working electrodes which are partly covered in SU8 such that the electrode area is known. Separate reference- and counter electrodes are in contact with the electrolyte from side channels in the PEEK holder.*

For SEM studies, we have developed an electrochemical cell with separate reference- and counter electrodes (Figure 3.9),[14] and with a chip providing an assortment of metal working electrodes which are used for a variety of different experiments, from electroplating to electrolysis and electromigration. A thin electron transparent silicon-rich nitride membrane separates the liquid

environment from the microscope vacuum. Such chips could with design layout modifications also be used in commercial TEM holders.

In this paper we compare our previous gold electrode electrochemical chip for SEM studies with pyrolytic carbon electrode chips (as illustrated in Figure 3.9). We study how the failure of gold electrodes at high potentials detrimentally affects electrochemical measurements, and how to make carbon electrodes which can withstand use in a larger potential window than gold electrodes. We test the chips for electroplating experiments. A process that can require large applied potentials is electrophoresis, and we use that as a test case for the comparison of gold and carbon electrodes. These results are of interest for those who intend to make chips for microfluidic electrochemical cells for in-situ SEM-, TEM- or related microscopy or spectroscopy, but also for e.g. electrochemical studies of biological samples due to the high bio-compatibility of carbon.[64]

Method

Chips were fabricated as discussed previously,[14] with microchips having low stress Si-rich silicon nitride membranes. Metal electrodes with a 10 nm Ti adhesion layer and 50 nm Au conduction layer were e-beam evaporated onto the wafer in a lift-off process. Separate wafers with carbon electrodes were prepared by patterning 1.8 µm AZ5214E photoresist on top of the membranes, then pyrolysing the layer at 900°C for 60 minutes in N_2. Lithographically defined holes in a layer of SU-8 photoresist were used to define the electrochemically active area in contact with the electrolyte. Until the time of use the individual chips were protected by covering them with approximately 10 µm AZ4562 photoresist. This layer was removed before use by immersing chips in acetone (two times 5 minutes) followed by isopropyl alcohol for an additional 5 minutes.

Electrochemical degradation measurements were performed in the microchip cell,[14] shown in Figure 3.9, using a commercial leak-free reference electrode (LFE) (Innovative Instruments, Inc, FL USA), Pt wire counter electrode and on-chip working electrodes. The reference electrode was measured to -37 mV vs a saturated calomel electrode. The electrolyte consisting of 0.1 M H_2SO_4 was degassed for at least 30 minutes in purified N_2. Cyclic voltammetry (CV) was performed with a PalmSense EmStat potentiostat at increasing potentials using a scanrate of 200 mV/s. CVs were performed with increasingly oxidative potentials until failure was observed with optical microscopy through the membrane.

Copper electroplating was performed in the same cell to compare the electrochemical properties of the carbon electrode with the similar gold electrodes. Two Cu-wires served as counter- and pseudo-reference electrodes respectively. The electrolyte was 0.46 M H_2SO_4 with 0.80 M $CuSO_4$. After electroplating on the electrodes, cyclic voltammetry was performed between +0.06 V_{Cu} and 0.3 V vs Cu (starting at 0 V_{Cu}) at 100 mV/s.

150nm citrate-stabilized gold nanoparticles (Sigma Aldrich) were mixed 1:1 with glycerol to reduce particle diffusion and to reduce particles adhering to the membrane. Manipulation was performed with an Ivium CompactStat by performing 2-electrode CVs between two adjacent on-membrane

electrodes at a rate of 2 V/s. Particles were observed through the membrane either with optical microscopy in dark-field mode, or with SEM.

An FEI Inspect tungsten-filament SEM was used for in-situ imaging, operated in low vacuum mode with a water vapour pressure of 10 Pa to prevent charging on the outside of the cell. Imaging was performed using the FEI LFD gaseous secondary electron (SE) detector. Due to the short mean free path of secondary electrons 12 (less than 50 eV by definition) compared to the membrane thickness it is most likely that the detected SE are produced in part by the backscattered electrons (BSE), and as such the information recorded at the homogeneous membrane surface is in reality a BSE signal. This is also indicated by the ability to vary the acceleration voltage between 15 kV and 25 kV to adjust how deep into the liquid the signal was probed, resulting in varying contrast of the carbon electrode and the gold nanoparticles in the liquid.

Results

The pyrolysis process reduced the layer thickness of the electrode photoresist from approximately 1.8 µm to 260 nm, consistent with earlier reports of pyrolytic electrodes with low resistivity.[65] Electrode pattern fidelity and dimensions were only marginally affected by the pyrolysis, resulting in a reduction in resist width from 9.6 µm to 9.0 µm after pyrolysis.

Conductivity of the pyrolyzed carbon was measured by electrical two-point measurements across a meander structure, recording a resistivity of approximately 15 µΩm shortly after pyrolysis. The resistance from contact pad to the electrodes was independently measured to 2.6 kΩ. On chips with gold electrodes the resistivity as measured across the same type of meander was 0.15 µΩm, i.e. 100 times less resistive. The carbon film appears hard, yet not too brittle, as no chipping or damage was observed from the conductivity probes contact points. The carbon electrode resistivity was found to increase significantly with storage time to 160 µΩm after 4 months and 220 µΩm after 9 months, despite the layer of protective resist.

Copper coverage during electroplating was used to assess the active area of the electrode. Plating on gold electrodes was performed by holding the electrode at -0.3 VCu for 30 seconds. Due to observed differences in the nucleation density the electrode preparation was different for carbon and gold electrodes: Carbon electrodes plated in a smooth homogeneous layer if first pulsed at -1.2 V_{Cu}, then plated at -0.3 V_{Cu}. If plated exclusively at -0.3 V_{Cu} only a few nucleation points dominated and created large structures, leaving most of the electrode bare. For gold the opposite was observed, and the best results were observed by plating at -0.3 V_{Cu} directly. During plating with these settings the edge of the electrode expanded homogeneously as copper was plated.

Visual inspection of the plated layer showed a homogeneous layer of copper covering the entire exposed electrode area, with no deposition where the SU8 was present (Figure 3.10). Cyclic voltammetry was then performed on this homogeneous copper layer, and the exchange current density was estimated from the cathodic part of the CV to be 25 mA/cm^2 and 16 mA/cm^2 for gold and carbon respectively. The difference observed might relate to e.g. a slightly different surface roughness of the film.

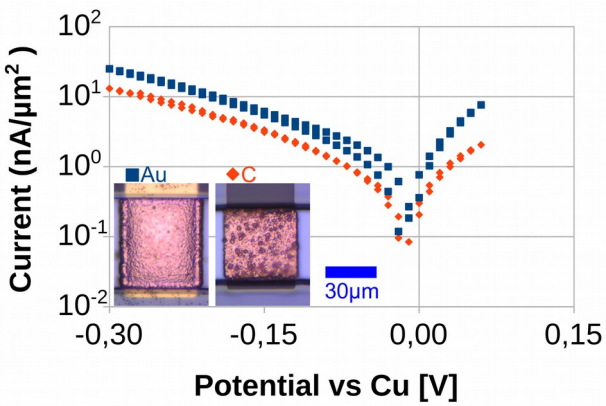

Figure 3.10: Electroplating of copper on gold- and carbon electrodes.

Copper was electroplated evenly on the entire exposed area of the electrode, without any exposure under the SU8. Subsequent CVs were used to obtain a Tafel-plot (double points correspond to the difference between sweep directions). A straight line through the four most negative potentials and the potential at which the current was zero was used to calculate a value for the copper exchange current densities for copper: 25 mA/cm2 on gold and 16 mA/cm2 on carbon electrodes respectively. In this estimate the projected surface area from the microscope images was used, which thus neglects surface roughness and the exposed sides on the left- and right side of the electrode.

To study the robustness, we performed CVs in 0.1 M H_2SO_4 extending to +1.25 V_{LFE} we and found that the gold electrodes gradually failed as the electrode was gradually etched from the outer perimeter of the electrode (Figure 3.11B). No such visual degradation was observed for carbon electrodes subjected to 2.0 V_{LFE} and CVs were reproducible after the first 2 cycles (Figure 3.11C). Carbon electrodes were seen to erode for each successive cycle when subjected to CVs up to 2.3 V_{LFE} (Figure 3.11D). As a consequence the carbon electrode had an onset of degradation at least 0.75 V higher than that of Ti/Au metallised electrodes. At the time at which these measurements were performed the recorded resistivity was 160 µΩm, which corresponds to an ohmic offset in the recorded potential of less than 30 mV from a current of 1 µA.

Both gold- and carbon electrodes eroded when subjected to high potentials until the entire exposed part of the electrode was destroyed. The part which was covered by SU8 remained intact, which shows that the increased stability of carbon electrodes is not due to residual contamination that insulates the electrode surface. This is further corroborated by the decline in the oxidative current of the CV as the electrode is gradually destroyed and surface area is reduced.

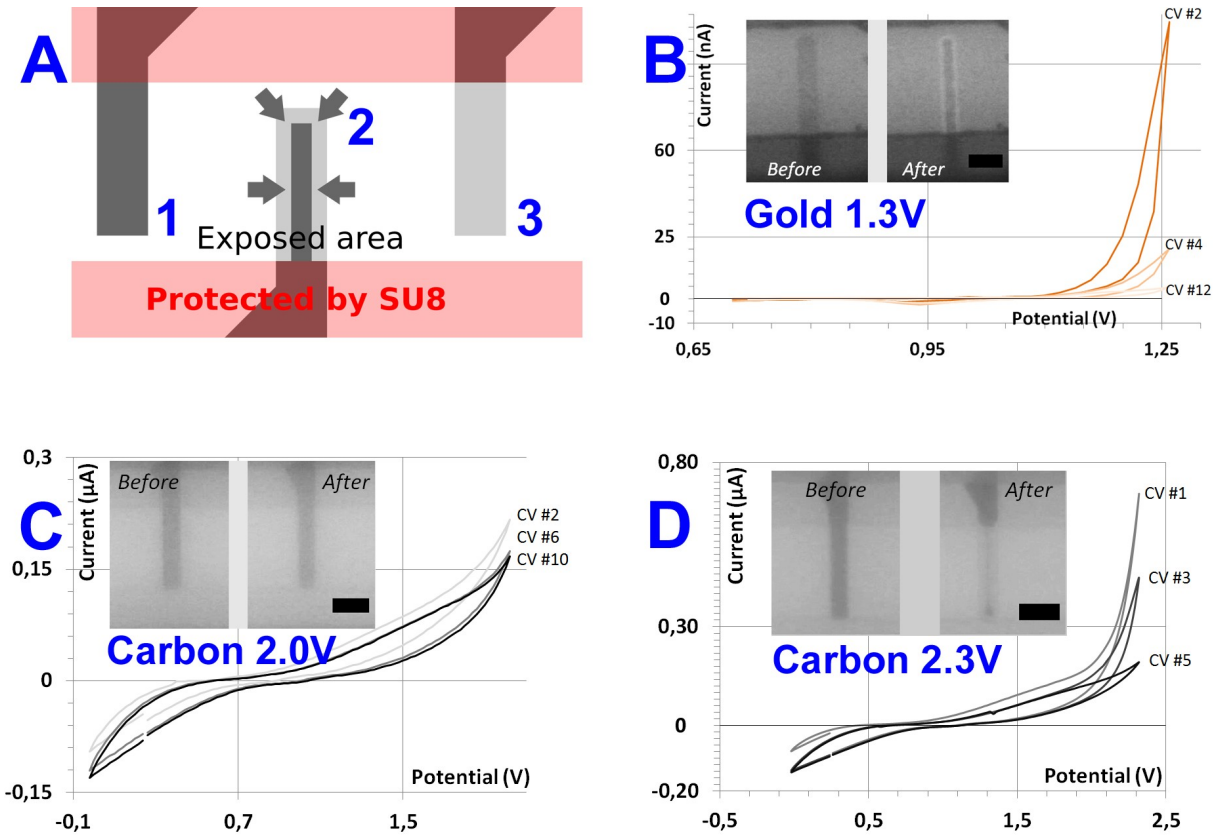

Figure 3.11: Comparison of degradation potential for Ti/Au- and carbon electrodes.

Gold electrodes were seen to degrade from the outer edges in CVs reaching 1.25 V_{LFE} and 1.3 V_{LFE} (Fig. B). The degradation process was seen to occur faster at higher potentials. Little to no degradation was observed for carbon electrodes cycled up to 2 V (Fig. C), neither in the CV nor in the optical images. At 2.3 V (Fig. D) the electrode was successively degraded for each cycle until all the exposed electrode material was destroyed. Insert: Before and after images for the respective electrode materials and potentials (scalebar: 20 µm).

The chips with carbon electrodes were also mounted in the SEM cell with an electrolyte containing citrate stabilised gold nanoparticles. It was apparent that the nanoparticles were affected by the presence of the beam itself, the aspects which have been studied by others in TEM,[66] but warrants a separate study for the SEM. Comparing to the readily visible gold electrodes at 25 kV, it was not possible to determine where the carbon electrodes were located on the membrane due to the small difference in scattering from water and carbon. At an acceleration voltage of 15 kV sufficient contrast was available to clearly see the electrode (Figure 3.12). This tunable translucency enables studies of e.g. particles which would normally be concealed by the electrode.

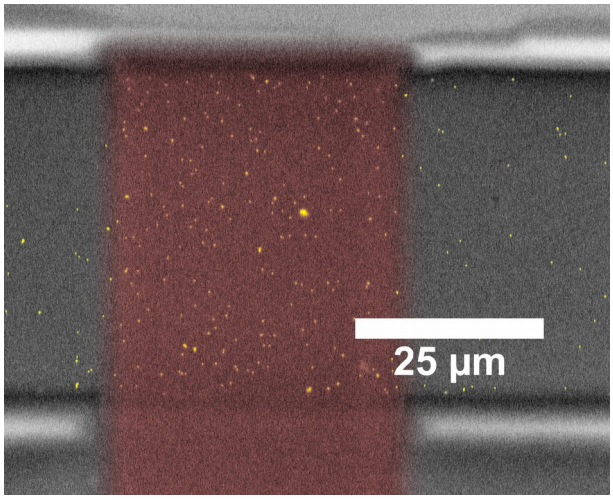

Figure 3.12: Gold nanoparticles on carbon electrode as seen in-situ SEM.

SEM image obtained at an acceleration voltage of 15 kV *showing high contrast spots (yellow) on the membrane (grey) and through the electrode (red) which correspond to nanoparticles being stuck on the membrane and electrode respectively. Particles would detach and disappear after a few seconds of focused exposure to the electron beam.*

Discussion

The electrochemical performance of the electrodes was assessed by means of copper electroplating, which showed that a homogeneous layer could be plated. Analysis of CVs performed after plating showed that the copper was in good electrical contact with the underlying carbon electrode. The CVs on copper coated carbon, and thus also the estimated exchange current density of copper, was comparable to similar measurements performed on gold despite the higher resistivity of the carbon electrode. As such, we conclude that the electrochemical performance of the carbon electrode is reasonable.

We found that pyrolyzed carbon electrodes are stable at least to potentials 0.75 V higher than that of gold, and destructive testing showed that this is not due to insulating contamination on the surface, as also shown by the homogeneous copper plating. The significant increase in the stable window compared to gold electrodes makes chip-based systems more versatile, as it allows a greater range of electrochemical reactions to be studied, as well as physical experiments which rely on high electric potentials such as electromigration.

Conclusion and outlook

We have fabricated a microchip for in-situ SEM studies which features carbon electrodes made by pyrolysis of AZ5214E photoresist. After copper electroplating carbon electrodes obtained similar values for the copper exchange current to that of a comparable gold electrode, despite higher carbon electrode resistance. The electrodes were evenly covered in copper, illustrating that the entire electrode is electrochemically active. The active area of the electrode was independently shown in dilute sulfuric acid, where at sufficiently high potential the entire exposed area of the electrode would be destroyed, but not parts which were covered in SU8.

Experiments with CVs performed up to high potentials demonstrated that the carbon electrodes could withstand potentials at least 0.75 V higher than the potential at which the Ti/Au electrodes failed. Because of carbon's low atomic number these electrodes scatter the electron beam less than gold electrodes, and as a consequence make it easier to make translucent or transparent electrodes for in-situ electron microscopy. As such, the technique to make pyrolysed carbon electrodes is very promising for the purpose of making chip-systems for in-situ electron microscopy, and in other systems where high potentials may be required.

In this particular work we did not emphasize thin electrodes, meaning that even more transparent electrodes can readily be manufactured by simply starting out with a more dilute solution of the resist. Doing so would allow in-situ experiments to resolve comparably smaller structures with SEM imaging through the electrode, although connecting leads may have to be augmented with a more conductive layer (e.g. gold) to compensate for the higher resistance.

Chapter 4: Radiolytic H_2 and H_2O_2 during SEM exposure

Introduction

Electron microscopy has undergone a gradual change from mainly being used to image metals, minerals and other resilient materials, to soft matter, gaseous environments and more recently liquid processes and even electrochemical cells. As a consequence imaging is no longer performed just on materials where damage caused by the electron beam can be studied before and after irradiation. Instead there is now a plethora of different effects that could change the operating conditions of processes observed live, as well as alter the sample temporarily.

It has been shown that several ionic liquids and lithium ion electrolytes degrade and precipitate particles under conditions prevalent in electron microscopes.[67,68] As can aqueous solutions containing chloroauric acid where the electrons act as a reducing agent.[19] Radiolysis can also happen, in which the impinging electron beam splits water to form gaseous bubbles.[19]

Based on earlier studies of radiolysis in which the complex interplay between radiolytic species was characterised,[17] Schneider et al.[18] used finite element simulations to predict the transient and steady-state reaction products of a 1 nA brightfield TEM electron beam at 300 keV passing through a thin sample containing liquid water. Due to the large differences in radiation type, energies and dose rates involved compared to traditional radiolytic studies they emphasise that the quantitative results cannot be taken literally, but provide a qualitative description of the outcome of electron microscope irradiation.

The simulations show that the most prevalent radiolysis products will likely be H_2 and H_2O_2, followed by $OH^{\bullet}$ and O_2, and finally hydrated electrons and atomic hydrogen. They also predicted a drop in pH for neutral solutions to 4.9 within the irradiated region.

The predictions made by Schneider et al. are mainly concerned with TEM samples sufficiently thin for most 100 kV electrons to pass through the sample without interaction. Here we use a SEM liquid cell with a single electron transparent window, and where the vast majority of the beam is absorbed, with the exception being <5% backscattered electrons.[14] Compared to current liquid cells for TEM, our comparably large cell allows for a more complex and feature-rich experiment, such as using commercial reference electrodes and a large number of on-chip electrodes. The SEM cell hence provides an electrochemically well controlled environment to study the radiolytic products that can also easily be extrapolated to TEM conditions.

In this study we set out to directly detect the reaction product of radiolysis, specifically testing the hypothesis that we can detect the long-lived radiolytic products by electrochemical means, based on the predictions of radiolytic products by Schneider,[18] i.e. that the concentration of; H_2 and H_2O_2 is comparable at around 1 mM, and at least an order of magnitude greater than other products, of which we shall focus mainly on O_2. In the following we will describe how our experimental conditions compare to those laid out by Schneider, and the method by which we detect the radiolytic products present. Finally we will compare our results to the predictions by the FEM simulations by Schneider et al., and discuss the deviations between what they predicted and we observed.

Experimental details

In this study we quantify limits for the presence of long-lived radiolytic aqueous species H_2, O_2 and H_2O_2, which we detect using electrochemical means. Measurements are compared to ex-situ control experiments with varying mixtures of the species. In the following the details of the electron transparent cell, the ex-situ cell and the electrochemical methods employed will now be outlined, starting with the electrolyte and ex-situ setup.

Reference electrode

Two different reference electrodes were used in this study; a traditional saturated calomel electrode (SCE) and a compact leak free electrode (LFE). The latter is a silver/silver chloride based fully sealed reference electrode with a glassy junction in which ions cannot cross (Innovative Instruments, inc., FL USA). The LFE was used in all experiments involving the SEM cell, while the SCE was typically used in the ex-situ beaker experiments.

The potential of the LFE vs SCE was routinely measured, and in our experiments we observed shifts in the potential between them indicating some hysteresis in the LFE. Shifts between different experiments could be several hundred mV, but within the time scale of single experiments, e.g. 1 hour, the electrode was stable to within <10 mV. For this reason we do not use the LFE to establish absolute values of the potential, but it is more than adequate for relative changes and for cyclic voltammetry.

Electrolyte

To ensure reliable electrical measurements we wanted a certain minimum of conductivity in the solution. Schneider reported that the expected concentration of radiolytic species varies with pH. To increase the chances of a clear signal we decided to go for an acidic starting point, since at low pH values H_2 and H_2O_2 concentrations were equal, and >100 times greater than O_2. Sulphuric acid was chosen due to pronounced hydrogen adsorption and desorption peaks,[69] and a nominal pH of 1.0 was achieved using 0.1 M H_2SO_4. The electrolyte was degassed for >1 hour by bubbling either nitrogen (prior to in-situ) or argon (prior to ex-situ) to prevent interference from atmospheric oxygen. In experiments relying on electrolysis for the generation of H_2 the electrolyte contained 1 M of Na_2SO_4 to enhance the conductivity, as the hydrolysis was very slow otherwise.

Ex-situ measurement setup

Qualitative oxygen and hydrogen detection were performed in a beaker with 0.1 M H_2SO_4, Pt wire working- and counter electrodes and a reference electrode (SCE or LFE) which were placed in a glass encapsulation. The electrolyte and chamber were both purged with argon. Baseline electrochemical measurements were performed before either hydrogen or oxygen was bubbled in the solution for several minutes. Hydrogen and oxygen gas were sourced as pure gas (AGA). Potentiometric measurements were performed while bubbling the analyte gas in the electrolyte, while cyclic voltammetry measurements were performed with the gas turned off. After completing the measurements the electrolyte was again bubbled with argon to verify that any electrochemical response was reversible.

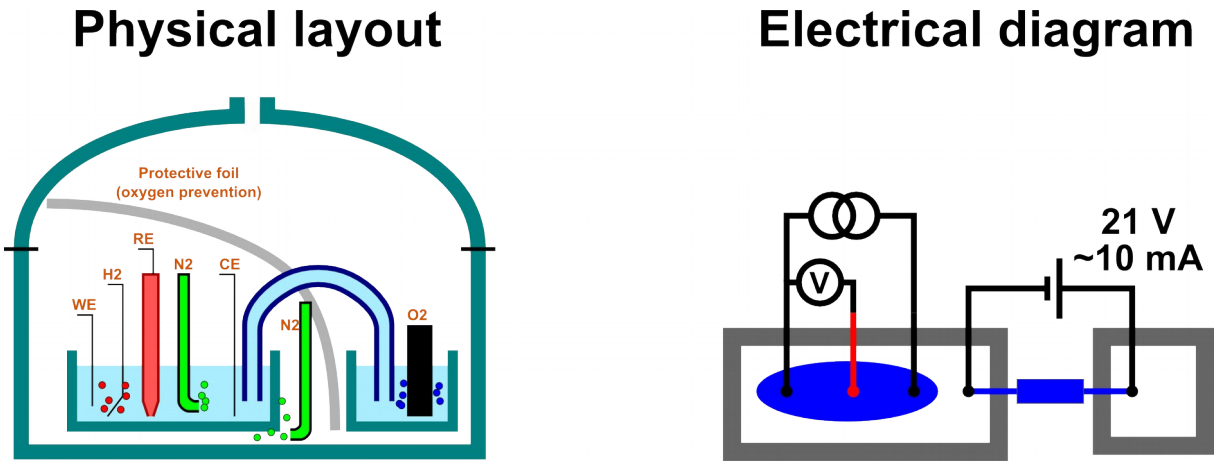

Figure 4.1: (Left:) Both the ex-situ gas bubbling experiment and hydrolysis experiments were set up in a glass chamber purged with an inert gas. Pt wires for WE and CE electrodes were placed together with the RE in one beaker, and in those experiments involving electrolysis this beaker was connected to a second beaker by means of a salt bridge. To prevent interference from oxygen the chamber was compartmentalized and purged continuously with inert gas. (Right:) OCP and CVs were performed with a potentiostat, while a Keithley 2400 was used to drive the electrolysis.

Both detection of hydrogen, and the influence of hydrogen peroxide on a hydrogen saturated solution was tested. The electrolyte was saturated with hydrogen by means of electrolysis. Hydrogen was evolved in the beaker of interest, which was connected with a salt bridge to a second

beaker outside the containment in which oxygen was produced Figure 4.1. H_2 has a low solubility (<1 mM), so although electrolysis produces OH^- in addition to H_2 the concentration is not sufficient to alter the pH in a solution of 0.1 M sulphuric acid appreciably. The interference between hydrogen and hydrogen peroxide was investigated with potentiometry while the electrolyte was continuously bubbled with hydrogen. At this point known amounts of H_2O_2 were added until a change in potential was registered. The continuous purging with H2 ensures proper mixing and allows an upper limit of H_2O_2 to be determined in later experiments.

In-situ cell setup

Our in-situ SEM cell, previously described by Jensen et al.,[14] consists of a PEEK liquid chamber (<0.5 mL), a PDMS gasket and a microchip with microelectrodes of platinum (Figure 4.2). The gasket was coated in a thin layer of Fomblin® RT-15 PFPE high vacuum grease to enhance seal quality. Electrodes are passivated outside the electron transparent region of the chip by means of SU8 photoresist. A platinum wire serves as the counter electrode, while the same leak-free reference electrode (LFE) is used as above. The cell is flushed with approximately 5 mL N_2-purged electrolyte before it is sealed off for an SEM-experiment.

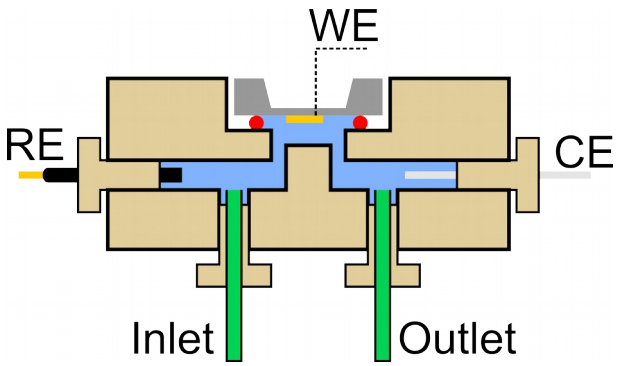

Figure 4.2: The SEM-cell maintains pressure by pressing the chip down onto the O-ring by means of a lid. Pogo-pins contact the different working electrodes which are placed in an array on the chip. Total liquid volume is less than 0.5 mL, and the recess immediately below the chip is 0.14 mL.

Ex-situ experiments in the in-situ cell

In addition to using the in-situ cell for the SEM experiments it was also used to test the detection limit of hydrogen peroxide by injecting known concentrations of hydrogen peroxide between 0 and 1 mM in the aforementioned H_2SO_4/Na_2SO_4 electrolyte into the in-situ cell by means of a syringe. For each fluid exchange the cell was flushed with at least 5 mL, corresponding to replacing the liquid fully 10 times.

In-situ SEM details

When performing measurements in-situ SEM it is important to keep the top surface neutral, as any charge across the nitride membrane can induce a structural failure of the membrane. Any charge resulting from the impinging beam and the loss of secondary electrons is neutralized by coating the surface with amorphous carbon in a TEM preparation coater and grounding the aluminium lid used to press the chip down onto the gasket. In addition, E-SEM mode is used with 10 Pa of water

vapour present in the chamber which is known to reduce sample charging.[70] Backscattered electrons create a cascade of secondary electrons which can be detected by means of the gaseous secondary electron detector, the LFD.

The beam current itself was measured in two ways: Either by the built-in hardware of the microscope which measures the current through the sample holder, and which is accessible by the software; or by leading the current out of the microscope, through a Keithley 2400 sourcemeter, before returning it to the grounded microscope flange. Both utilized a Faraday cup.

For these experiments we used an FEI Inspect SEM with tungsten thermionic emission configured to 25 kV, starting out with the lowest current. During the experiment the beam current was varied from 50 pA to 8 nA. The beam was initially focused and imaging fine-tuned on areas of the chip which did not contain a window. Subsequently the general area in which the membrane and electrodes are situated was found, and the irradiated area was quickly narrowed down to 40 µm x 25 µm. During irradiation the potentiometric signal was continuously recorded.

Electrochemical techniques

An Ivium CompactStat potentiostat was used to perform the electrochemical measurements. The main techniques used were cyclic voltammetry (CV), open circuit potential (OCP) and chronopotentiometry (CP). Cyclic voltammetry was performed using a stair-case waveform, while the recorded current was the average of each step to correctly reproduce transients (i.e. hydrogen adsorption and desorption) as per the manufacturer's recommendations.[1] In some measurements it was possible to measure multiple electrodes simultaneously using an external Ivium differential amplifier with high impedance inputs.

One challenge with electrochemical experiments performed in an SEM is the injection of charge into the cell by the electron beam. This charge must be dissipated to prevent a build-up of high potentials and erroneous data being recorded from non-faradaic capacitive effects and discharges. Some of the problems associated with charging include degradation of cell components, image distortion, membrane failures – and potentially also damage to the potentiostat if not correctly grounded.

During normal operation, for example during chronoamperometry (a digital/staircase CV can be viewed as a series of such measurements), the potentiostat is set to achieve a certain potential, V_{set}, between the WE and RE. This is achieved by a feedback loop that applies a voltage between the CE and WE, and as a consequence drives a current between them. Depending on the V_{set} potential the counter electrode can either source or drain any current needed. After a short time to settle, the potentiostat reads out the magnitude of the current and stores it in the data file. The important realisation is that since the WE is by convention connected to GND in the potentiostat the net current is also being sourced/drained to GND at the WE. But at the CE the current is obtained from

1 In normal staircase CVs the current is measured at the end of each voltage step, after the current has stabilised. Since some surface effects like hydrogen adsorption/desorption are capacitive in nature, and thus transient, they are poorly reproduced in traditional digital CVs unless the current for the entire step is averaged. Additional information is usually provided in the potentiostat documentation (e.g. Gamry, Ivium).

the amplifier source/drain supply voltages which enable the CE to be regulated up to V_{s+} and down to V_{s-} to meet the target V_{set} at WE.

Hence, when an electrochemical cell is set up in an SEM there is an additional current of electrons which is injected into the cell regardless of whether the cell (i.e. CE) relay is ON or OFF. The premise for OCP is that the electrode is in equilibrium, but in this configuration the CE relay is off and thus this is no longer the case: Any net current – i.e. the electron beam current – is being sourced/drained to GND at the WE, although the current is not measured or accounted for by the potentiostat.

To avoid this issue we use chronopotentiometry (CA), rather than a standard OCP setting, to measure the effective open circuit potential. The CA is set up with an applied WE current of zero at a very low current range, which the potentiostat actively regulates by monitoring the ammeter that connects WE to GND. During this regulation the CE potential is adjusted so that the net beam current is sunk there without affecting the WE. Although ESEM-mode is used for imaging, this may not be able to adequately protect against charge accumulating on the liquid side of the insulating silicon nitride membrane. It is therefore essential that this regulation loop is operating, even if no measurement is needed, as otherwise the cell may burst due to electrostatic breakdown of the membrane, or the connected electronics might be damaged.

Chronopotentiometry may not be as precise as true OCP, since the accuracy of applied potentials is lower than if it is just measured (<2 mV for Ivium CompactStat), and because the actual applied current depends on the current resolution (current range). We used a current range of 100 nA (resolution 13 pA) on an electrode which had a typical CV peak current of 1-2 µA, which provided a signal to noise ratios suitable for the experiments.

During cyclic voltammetry there is not the same concern of which path the injected electrons will take, since the current needed to polarise the WE with respect to the reference electrode is correctly measured, and it does not matter if the current is sourced by the electron beam or the CE. Should the electron beam exceed what is needed the CE will sink as much as is needed.

Method of detection – electrochemical fingerprints

Detection of H_2

Detection and quantification of hydrogen by potentiometry has been studied extensively[71] and found use in the quantification of corrosion rate.[72] Metallic platinum is particularly well suited for potentiometric detection of H_2, since the potentiometric signal is independent of geometry,[73] which allows it to be scaled down to the microelectrodes used in our SEM-cell.

In a hydrogen-rich electrolyte, as is the case for the hydrogen reference electrode, the Pt electrode has a potential governed by the Nernst equation, in which it varies with pH (given by the activity *a* and the concentration of H_3O^+) and the logarithm of the partial pressure of H_2 ($p[H_2]$):[72]

$$E = E_0 + \frac{RT}{nF}\left(\ln\left(\left[H_3O^+\right]\right) - \frac{1}{2}\ln\left(p\left[H_2\right]\right)\right) \quad (4.1)$$

Where E_0 is commonly the offset with respect to the hydrogen electrode, i.e. 0 V in our case; RT is the ideal gas constant and temperature respectively, n=1 is the number of electrons per reaction and F is Faraday's constant.

However, in practice the Nernstian potential is only valid when only H_2 is present, i.e. abundant. When O_2 is present in the system the potential can instead be described in terms of a mixed potential which is determined by the simultaneous reduction of oxygen and oxidation of hydrogen. Siebert et al. describe three distinct regimes as H_2 concentration increases, overlaid in Figure 4.3,[74] from which it is clear that Equation 4.1 does not adequately explain the sudden drop in measured OCP versus concentration.

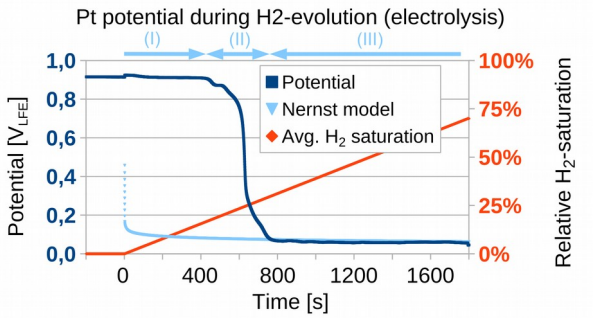

Figure 4.3: Oxygen and hydrogen were produced by means of electrolysis in two separate beakers connected by a salt bridge. As H_2 concentration increased in the electrolyte of the beaker with the passive sensing Pt electrode, the three regimes of the platinum-hydrogen electrode can be seen (approximate location indicated). Total drop in OCP was 870 mV. Measured with respect to the LFE reference electrode. The expected potential based on the Nernst model was calculated by assuming the potential at 2400 seconds to be fully saturated at 1 atmosphere partial pressure.

The three regimes[74] are: (i) A low H_2 regime in which the main reactions are reduction of oxygen and the oxidation of Pt in contact with water. (ii) An intermediate regime in which the potential changes abruptly when the concentration-dependent limiting hydrogen oxidation current according to the Tafel equation equals that of oxygen reduction. (iii) And finally a H_2-rich regime in which the Nernst equation holds and there is a linear dependence between the measured potential and the logarithm of the H_2-concentration.

We found that even after extended bubbling of the electrolyte in purified N_2 the potentiometric signal appeared to follow the mixed-potential profile in Figure 4.3 during H_2 evolution, starting out in the high OCP region exceeding what a pure Nernstian response to a very low concentrations would suggest. When performing electrolysis on a degassed electrolyte in a pulsed manner in the fully enclosed SEM-cell (shown previously) a distinct drop in OCP started to form already after generating enough hydrogen to reach between 0.1 and 0.5% saturation, as would be expected from the Nernst-equation.

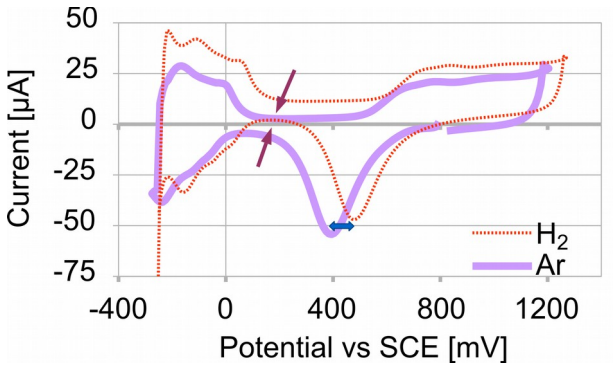

Figure 4.4: Cyclic voltammetry in an Ar-saturated beaker and in the same beaker after H_2 bubbling. The shift in peak position (blue arrow) and the positive shift in current (purple arrows) was also seen in a similar experiment where the H_2 was sourced by electrolysis and the LFE was used as reference. The vertical shift is well suited to determine whether the system contains H_2 by looking at whether the reductive (negative) current is zero at the green arrow (H_2 present), or the oxidative is zero (not H_2). The absolute magnitude of the oxidative current is also influenced by how low in potential the sweep is, since any H_2 generated by electrolysis can subsequently also be oxidized back to water.

CVs were also performed to determine how hydrogen influenced such measurements. Two different ex-situ setups were tested; one in which the electrolyte (0.1 M H_2SO_4 and SCE reference electrode) was bubbled in first argon then H_2, and one in which the electrolyte (0.1 M H_2SO_4 +1.0 M Na_2SO_4 with LFE RE) was bubbled with N_2 after which hydrogen was produced by electrolysis. In both cases we saw a shift in the peak potentials, as well as a vertical shift in the measured currents (Figure 4.4). The measured response makes sense in light of Le Chatelier's principle: e.g. in the presence of abundant dissolved H_2 gas the current is shifted such that no H^+ is reduced to H_2, and the potential is shifted such that a higher potential is needed for oxidation (e.g. of the Pt) while it is not necessary to go as low in potential to reduce it again.

In summary, the presence of H_2 can be determined based on a significant drop in OCP, a signal that may be corroborated by the slight changes in CV.

Detection of H_2O_2

Several electrochemical means of detecting hydrogen peroxide have been demonstrated. Chronoamperometry on a Pt electrode at +600 mV_{SCE} (nominally 840 mV_{SHE}) provides a current signal that is linear with concentration at low concentrations (less than ca 20 mM).[75] However, since the electron beam produces many species – including oxygen – that may alter the measured current such an electrode may not be sufficiently selective, and since the detected current scales with the surface area of the electrode the beam current will eventually be significant in relation to the electrochemical response for these microelectrodes as they are miniaturised.

Cyclic voltammetry can also be used to detect H_2O_2. E.g. one study found that upon the addition of 5 mM a peak appeared at +0.4$V_{Ag/AgCl}$.[76] Gu and Chen provide a clearer picture of how the CV is modified by the presence of hydrogen peroxide.[77] Most importantly, they showed that O_2 can be distinguished from H_2O_2 since only H_2O_2 increases the anodic current at positive potentials (beyond +0.4 $V_{Ag/AgCl}$). The remaining parts of the CV (the cathodic peak and the hydrogen

adsorption/desorption signal) are offset towards more negative currents for both oxygen-containing and hydrogen peroxide containing samples, which they attribute to oxygen resulting from the decomposition of H_2O_2.

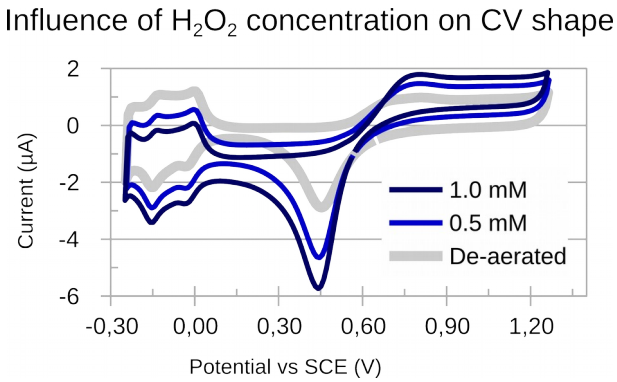

Figure 4.5: When injecting electrolyte containing increasing concentrations of H2O2 we observed that the CV shifted towards more positive currents at positive potentials, and more negative currents at negative potentials. This agrees with the expected result.

According to the prediction by Schneider et al. hydrogen peroxide and H_2 should be present in similar concentrations, approximately 1 mM. The solubility of H_2 in water at room temperature is approximately 0.8 mM.[78] In a de-aerated solution we saw a significant response in the CV shape to the addition of H_2O_2 in the EC-SEM cell, with the cathodic part shifted towards more negative currents, and the anodic part towards more positive currents, very much as would be expected (Figure 4.5).[77]

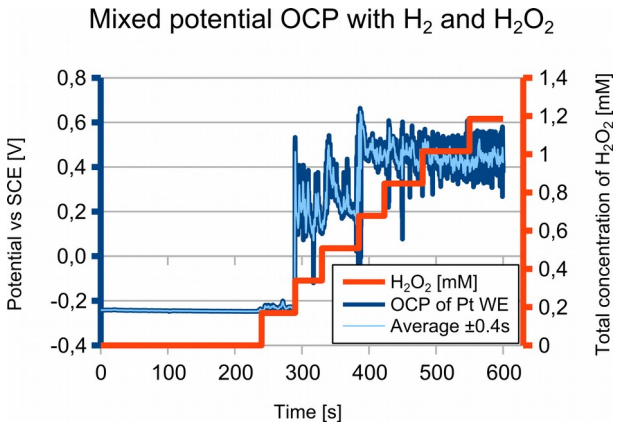

Figure 4.6: Adding H_2O_2 to a solution saturated and continuously bubbled with H_2 revealed that already at a H_2O_2 concentration of 0.3 mM there was a significant increase in potential, and the low potential characteristic of H_2 was no longer obtainable.

H_2 and H_2O_2 are competing species when it comes to determining the open circuit potential of Pt vs. a known reference. The influence of H_2O_2 was determined by bubbling the electrolyte continuously with H_2 to ensure proper mixing, while pipetting in diluted H_2O_2. Already at 0.3 mM H_2O_2 in the H_2-saturated electrolyte we found a Pt vs SCE potential 0.25 – 0.3 V, an increase of more than 0.4 V vs. the hydrogen saturated solution (Figure 4.6). This makes OCP detection suitable to determine the ratio of H_2 to H_2O_2, but the absolute concentration is not known. For example, since the solubility of

H_2 is approximately 0.8 mM it shows that if the potential is low then the concentration of H_2 to H_2O_2 must be at least 2.5:1.

Detection of oxygen and possible interference

Because oxygen is another possible radiolytic product we looked at how ambient and pure oxygen levels affected the CV by performing measurements on both both deaerated and non-deaerated solutions (Figure 4.7). As with hydrogen peroxide, the currents recorded at cathodic potentials are shifted negatively in current, while there is little change on the anodic side of the Pt reduction peak.

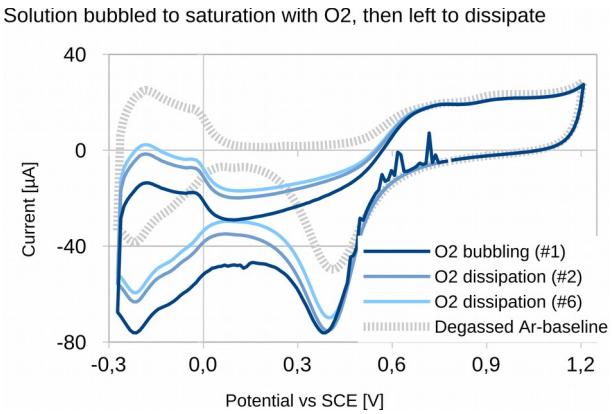

Figure 4.7: CV performed in 0.1 M H_2SO_4 (vs SCE) at 100 mV/s after degassing in argon, and after saturating the solution with O_2 by bubbling. Some bubbles are seen in the first O_2 scan caused by slight residual pressure in the O_2-line, after which the O_2 levels in the solution drop off as it is exposed to ambient conditions. When the solution was subsequently degassed in Ar the initial curve was fully restored. When subjected to air the graph the atmospheric oxygen produces a similar change to the cathodic part of the graph.

The solubility of oxygen at room temperature is only 0.27 mM,[79] which means that at ambient conditions the electrolyte will contain no more than 0.06 mM when in equilibrium with the air. It is worth noting that the solubility is reduced when salts are introduced to the electrolyte. Compared to how the CVs appear in the presence of hydrogen or H_2O_2 at the above tested concentrations, the aerated electrolyte displays a very characteristic signal for the low O_2 concentration, and CV is thus a very sensitive method of detecting O_2 presence. It is also a selective method, since among the radiolytic products which are present in significant numbers only O_2 and H_2O_2 depress the cathodic side of the CV, and only H_2O_2 shift the anodic side.

Diffusion of dissolved hydrogen and H_2O_2 in the electrolyte

During SEM experiments we are irradiating the sample for a few minutes at a time. During this time radiolytic species are generated and diffuse away from the irradiated region. In our cell we have a number of electrodes in a linear array, where the greatest distance between two electrodes is approximately 4 mm. The smallest spacing between electrodes is 80 µm.

Although the SEM-cell is small compared to most tabletop electrochemical cells the distances involved still require diffusion to be considered. Hydrogen diffuses almost three times faster than H_2O_2 ($4.5 \cdot 10^{-5}$ cm^2/s and $1.7 \cdot 10^{-5}$ cm^2/s respectively).[80,81] At this rate the characteristic diffusion

length after the 26 seconds a typical CV cycle takes to complete[2] will be 340 µm for hydrogen and 210 µm for hydrogen peroxide. During a typical beam irradiation experiment lasting 200 seconds the distance will be 950 µm and 580 µm respectively. The consequence is that during the experiments we would expect radiolytic products to be detectable on most electrodes on the chip, and we would expect there to be a sufficient volume of electrolyte surrounding any electrode for the measurement technique to be completed without fully depleting the electrolyte.

Summary

Based on the ex-situ measurements we can draw up a table (Table 4.1) over the characteristic fingerprints of the three elements we are looking for. In short, only hydrogen reduces the OCP, and if enough hydrogen is present the OCP can drop many 100's of mV. It also causes a slight positive current-shift in the lower range of the CV. H_2O_2 and O_2 both raise the OCP back to initial levels, and produce a very clear and distinct change in the CV, where O_2 and H_2O_2 can be told apart in the anodic (positive) potential range.

Compound	CV, lower range	CV, upper range	Pt-O_{red}	OCP
Hydrogen	(↑)	(↑)	→	↓↓
Oxygen	↓↓	–	(←)	↑
H_2O_2	↓↓	↑↑	(←)	↑
H_2 and H_2O_2				↑

Table 4.1: Both CV and OCP measurements are affected by the change in electrolyte composition. For hydrogen the strongest indicator is a distinct drop in OCP, while O_2 and H_2O_2 can most easily be told apart from the shift in CV and the difference in the upper potential range. Arrows indicate in which direction the electrochemical signal is shifted, e.g. OCP ↓ indicates a drop in potential, and ↓↓ a severe drop in potential.

In-situ results

In the following section we will first show OCP measurements to test the presence of radiolytic H_2 against the test-criteria in Table 4.1, followed by CVs to investigate the presence of H_2O_2, O_2 or other radiolytic species.

Irradiation experiments were set up to investigate any changes to the OCP and CV. The beam current was started at 0.050 nA and gradually increased to 7.7 nA. The electrolyte (0.1 M H_2SO_4) was the same for all experiments, and was not replaced between irradiation cycles. Typically the irradiation was performed for a few minutes at a time, which due to the size of the cell is not sufficient to reach equilibrium. After irradiation the system was subjected to a CV, typical duration of 4-5 minutes, after which it rested for at least 100 seconds before the next irradiation.

2 Spanning 1.3 V at 100 mV/s, both directions.

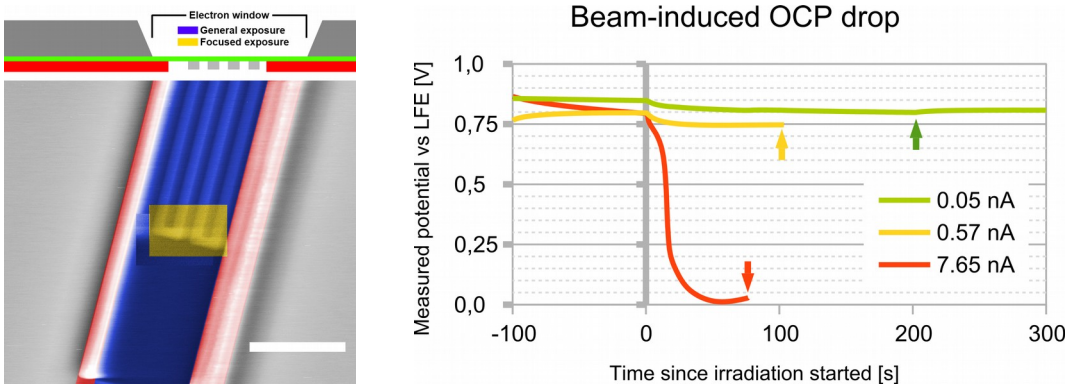

Figure 4.8: (Left, scalebar 50 µm:) After locating the connected electrodes the irradiated area was narrowed down to the electrode tip to ensure the beam irradiated the liquid rather than the grounded bulk silicon. (Right:) Irradiation induced an immediate drop in the measured OCP, the magnitude of which depended on the beam current being used. When the beam was switched off (arrows) the OCP started to recover, but did not reach its initial level. This result is consistent with the production of radiolytic hydrogen. The increase seen towards the end of the irradiation for the measurement at 7.65 nA is discussed separately.

The experiment shown in Figure 4.8 demonstrates how the measured OCP dropped progressively as higher beam currents being tested. Not only did the minimum voltage drop with larger beam currents, the rate at which the OCP dropped to those levels also increased. When the beam was moved to an adjacent electrode and the beam was no longer impinging on the working electrode (Figure 4.9) the OCP was seen to continue to drop, albeit at a slower rate. This indicates diffusive supply of the H_2 from the irradiated region and that the effect we are observing is not merely a subtle charging effect in the system.

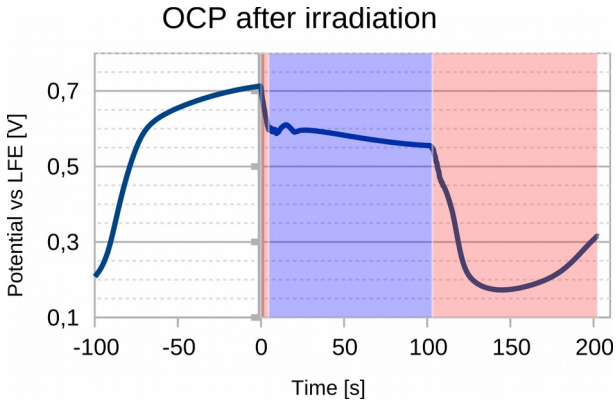

Figure 4.9: Initially the OCP recovers from a recently terminated CV. When the 7.7 nA electron beam is turned (red) there is a rapid decrease in potential. When the beam is relocated to another nearby electrode 80 µm away (blue – measurement still on the 1st electrode) the decrease continues at a lower rate. After 100 s the beam is returned to the original electrode and the original rate of OCP-change is resumed. After 120 seconds the OCP flattens out before it starts to increase while still being irradiated.

A surprising observation is that unlike the ex-situ experiments in which hydrogen was produced by electrolysis or by bubbling, the in-situ results show that the potential eventually starts to increase

again while the beam is still irradiating the sample. We know from the ex-situ experiments that the presence of either O_2 or H_2O_2 is capable of raising the OCP of even a H_2 saturated solution.

A more detailed study of this long-term irradiation effect shows that there appears to be a regime-change in high beam current experiments the beam causes the OCP to drop. When the beam is turned off OCP "returns" to a value somewhere in-between the initial value and the last value before the beam was turned off. When the beam is left on for extended periods of time (5 minutes irradiating the same area in this case) the opposite eventually occurs; OCP decays to a lower value than the last value with the beam on (Figure 4.10). Once the electrolyte is in this regime OCP will increase if the beam is turned back on.

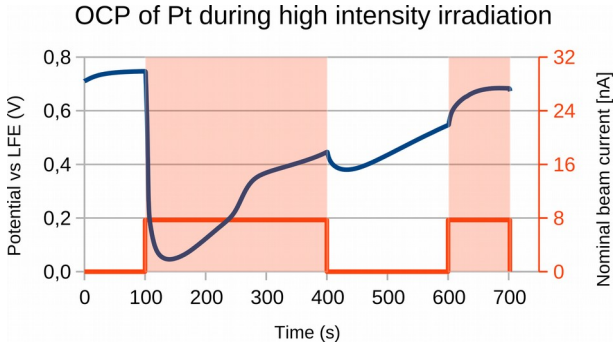

Figure 4.10: When irradiating the sample with a sufficiently high beam current (indicated in red) we observed that the measured OCP would first rapidly decrease, consistent with the evolution of hydrogen, but as the irradiation continued the OCP started increasing again.

To shed some additional light on what exactly is happening we performed CVs between OCP measurements. The first CV cycle in the measurement provides the most instantaneous picture of the electrolyte, while later CVs provide a steady-state picture where species which are forced to react on the electrode are replenished by diffusion from the electrolyte.

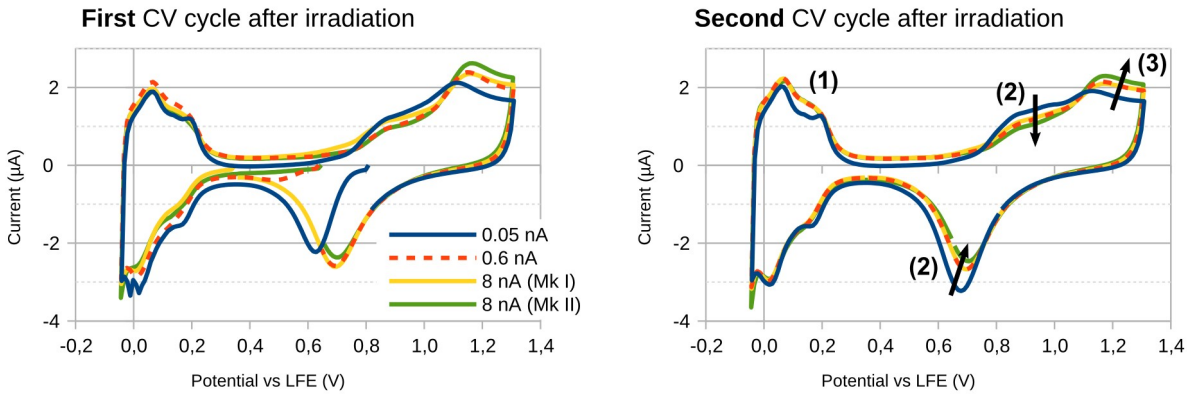

Figure 4.11: (Left:) The first cycle of CV after irradiation can be used to analyse the electrolyte in immediate vicinity of the electrode. This peak does not match the ex-situ experiments of neither H_2O_2 nor O_2. (Right:) There are three things of note in this graph of the 2nd CV cycle: (1) The hydrogen desorption peak is either unchanged or increasing with current; (2) both the Pt-O reduction and oxidation peaks decreases in magnitude; and (3) a new oxidation peak appears. None of these three changes are indicative of H_2O_2 or O_2 present. There is also a slight positive shift in current seen around and below 0.4 V_{LFE} which is anticipated for H_2 presence.

In events where the electrolyte may have significant gradients in the concentration it is worthwhile to look at the very first cycle (Figure 4.11). The cyclic voltammogram is not consistent with the production of H_2O_2, since the current is shifted vertically towards more positive values at potentials below than the platinum reduction peak. There is also not a significant vertical shift of the oxidation peaks, but rather an increase in current. Although this bears some resemblance to the initial ex-situ experiments containing oxygen, the CV is not shifted towards more negative currents at low potentials as expected. Later cycles of the CV – i.e. complete and stable cycles – reveals the same. It must therefore be concluded that there has not been enough oxygen or hydrogen peroxide for us to detect it, despite the presence of hydrogen.

Discussion

In the preceding we set out to investigate whether the prediction by Schneider et al. is accurate; that the dominating radiolytic species in an acidic aqueous solution are H_2 and H_2O_2. In the ex-situ experiments we found that the H_2O_2 will mask the signal of H_2, hence conditions as predicted in Schneider et al. would give high OCP-readings and a clear H_2O_2 signal in the CV.

The experiment was set up with a rastering beam such that the frame-averaged intensity was varied between 0.1 and 20 MGy/s, with an instantaneous local intensity in the majority of the volume of 7 to 1000 MGy/s.

From the drop in OCP and marginally varying CV measurements we conclude that the concentration of H_2 is significantly higher than H_2O_2, at a ratio of at least 2.4:1, and likely closer to 4.7:1. This is in stark contrast to Schneider, which for de-aerated water with neutral pH obtains a ratio close to unity, with a slightly higher H_2 concentration, with the difference becoming indiscernible at low pH. In an deaerated electrolyte at low pH their predicted ratio of hydrogen to hydrogen peroxide is ~1.1:1, with a much higher concentration of hydrogen peroxide present in the aerated electrolyte.

We also see a change in the OCP which coincides with a change in the CV which is inconsistent with the CV of platinum in acid or the presence of H_2, O_2 or H_2O_2. Other radiolytic radicals predicted by Schneider, such as solvated electrons, $OH^{\bullet}$ and $O^{\bullet}$, all have too short lifetimes to still be recorded after several CV cycles – each of which lasts >25 seconds.

Radiolysis of sulphuric acid is a possible candidate, since the lack of vertical shift in the anodic part of the CV and the emergence of a stronger cathodic peak would match that of sulfur on Pt.[82] Sulphur has a very rich radiochemistry,[83] and will significantly affect a CV even in ppm concentrations.[84] The 0.1 M sulphuric acid used as electrolyte may thus be a sulphur source during extended irradiation.

From literature[84] one would expect the CV to also lose the hydrogen ad-/desorption peaks in the presence of sulphur, which is not observed. A possible explanation could be a more localized nature of radiolytic sulphur: Unlike the cited experiments for fuel cells our electrolyte is not saturated with a sulphur precursor, instead the sulphuric acid decomposes to some extent in interaction with the

electron beam and other radicals. This leads to a localised region with sufficiently high sulphur concentration to affect the OCP and CV. And since the Pt electrode used for the CV extends more than 1 mm beyond the irradiated area there is plenty of Pt surface area that has not been sulphur-poisoned and consequently is still able to produce a hydrogen adsorption- and desorption signal.

The tendency where the OCP is seen to rise upon irradiation, and drop when the beam switches off, after being irradiated for extended periods of time might be because of a mixed potential between the hydrogen and oxidative sulphur species, the presence of which is indicated by the anodic peak in the CV.

This experiment further emphasizes that radiolysis causes large changes to the electrochemical environment of the electrolyte, and should not be overlooked when planning and performing in-situ measurements with ionizing radiation. Measurements can easily be affected in such a way that it could lead to incorrect conclusions being drawn, unless the effect is carefully considered and accounted for, regardless of whether it is a SEM experiment, TEM, or for instance a high energy X-ray cell. It is therefore in the interest of anyone using ionising radiation for in-situ electrochemical experiments to attempt to predict and measure which radiolytic species are produced during an experiment.

Conclusion

We set out to test the predictions made by Schneider et al. in the context of a liquid SEM-cell. Although the SEM differs from a TEM by absorbing nearly all the beam energy vs. only a small fraction, it is possible to show that the average energy absorbed near the chip is comparable for some typical SEM parameters in use here. Since the conditions are similar we sought out to detect the two main species in the prediction, hydrogen and hydrogen peroxide.

Based on a series of ex-situ and in-situ measurements we believe that we have detected the presence of hydrogen by its potentiometric signature; distinct reduction in the open circuit potential on a platinum electrode. The concentration of hydrogen increases with beam current and exposure time. Based on the predictions for TEM we also expected to see hydrogen peroxide, which we have not detected. As such it appears that the concentration of hydrogen peroxide is significantly lower than that of hydrogen under the conditions valid for SEM. H_2 is rapidly produced over the course of a few tens of seconds, depending on the radiation intensity.

However, we did not detect H_2O_2 despite ex-situ experiments showing that we should be able to. Instead of the O_2 and H_2O_2 we observed changes in the cyclic voltammetry that is more consistent with the presence of sulphur which causes sulphur poisoning of the part of the Pt-electrode which is exposed to the beam.

The conflicting results from predictions and measurements is illustrative of the complex interplay occurring in aqueous electrolytes during electron microscopy, and as such should be interpreted as a strong caution against using simulations blindly without direct measurements. This emphasizes the

need to study beam effects in depth as in-situ electron microscopy studies find their way as an increasingly valuable tool for spatially resolving electrochemical properties of materials.

Chapter 5: Radiolytic changes in electrolyte conductivity

Introduction

The conductivity of water is determined by the ionic strength and the mobility of those ions. For pure water self-dissociation provides the charge carriers, but in most solutions this number is dwarfed by that of impurities or additives. Directing an electron beam into the electrolyte will inevitably create charged species which alter the conductivity. To which extent this is the case depends on the radiolytic yield and the specific species being produced. Depending on the experiment the (spatially dependent) change in electrolyte conductivity may be affecting measurements by altering IR potential drops, reducing debye lengths and providing conductivity for e.g. corrosion.

Consequently it is interesting to quantify the beam induced changes so that this effect can be accounted for when designing in-situ experiments. Since EIS is a fundamental electrochemical characterisation method which has so far not been applied to in-situ electron microscope liquid cells, it also is valuable to investigate if this method can be applied and to what extent the radiolytic effects may influence such measurements. For this reason we use EIS in this study to measure radiolytic changes in electrolyte conductivity between adjacent microelectrodes.

There are different ways of quantifying the electrolyte conductivity. One way is to use a dedicated instrument. In such instruments 2, 3 or 4 electrodes are used to apply an alternating electric current which is regulated such that a certain potential is measured. The exact frequency varies with the measurement system and with the conductivity range it is configured for, but in general lower frequencies are used with lower conductivity electrolytes, e.g. on the order of 10^2 Hz vs 10^4 Hz for

higher conductivities.[85] Based on the measurement result the electrolyte conductivity can be calculated by correcting for the specific geometry of the probe by what is called the cell constant.

In the case of the 2-point system the same two electrodes are used to measure the potential as to apply the current. This system suffers from convoluting the electrode polarisation resistance with the electrolyte resistance, but as the electrolyte conductivity drops this effects diminishes.

Four-point measurements are more accurate because the current is sourced at two electrodes, while potential is measured across the remaining two. Since no current is being drawn on the remaining two electrodes the polarisation resistance is zero, eliminating this form of error.

In order to further reduce the polarisation resistance it is common to increase the surface area of the electrodes, and thereby reduce the effective current density. If it is not possible increase the geometry dimensions further one can platinise the electrodes (i.e. form black platinum), but this has the adverse effect that the electrode is less tolerant to contamination and handling, since the platinisation must be factored in when determining the cell constant.

Two-point probes have been used in previous microsystems since they can be made more compact than a four-point system. A relevant example is the study by Ayliffe et al. who produced microelectrodes with gaps ranging from 5 to 10 µm, and characterised them using deionised water and various concentrations of phosphate buffered saline (PBS).[86] The exposed surface area of the electrodes was not mentioned, but their SEM images suggest an area on the order of 4 µm by 10 µm. They conclude that they are able to differentiate between the different conductivities (starting at a concentration of 150 mOsm, i.e. 150 mmol ions per liter).

Ayliffe et al. used electrochemical impedance spectroscopy (EIS) to measure the electrolyte conductivity. EIS is a technique that where the applied AC electrical signal is swept across the frequency range in order to measure the impedance of the electrochemical system. It is as such not limited to one or a few frequencies in the same way simple conductivity meters are.

In this study we are looking at radiolytic species produced when the electron beam strikes water. Upon irradiation water will up until 10^{-6} s undergo increasing levels of chemical recombination and reactions based on the initial physical yield. These reaction finally end up with a set of longer lived radiolytic species, such as H^+, H_2, H_2O_2 and $OH^{\bullet}$.[16,18] During continuous irradiation the transient species such as the hydrated electron can be expected to play a role in the electrolyte conductivity.

Although Woehl et al. stated that more than 35% of the initial radiolytic yield would be hydrated electrons and 6% hydrogen gas, Schneider et al. predicted that the ratio of hydrated electrons to hydrogen to be only 1:1000:[18,20] Their prediction was based on the many possible reaction pathways for radiolytically split water and the respective rate constants. In these calculations they find that the highest concentrations are expected to be seen for the non-ionic H_2 and H_2O_2, both close to 1 mM. Other species are expected to be on the order of 10 µM, while hydrated electrons are predicted to be 1 µM or less.[18]

The exact number of charged species is not predicted by Schneider et al., but if the concentration of charged species is lower than the concentration of other radiolytic products due to recombination to more stable products, then the concentrations of ionic particles that is of interest in this study will be 2 – 3 orders of magnitude lower than that demonstrated by Ayliffe et al. when they demonstrated that microelectrodes could detect different electrolyte conductivities by means of EIS.

EIS for electrolyte resistance measurement

Normally EIS is performed by applying a low voltage (e.g. 10 mV) AC signal on the working electrode. To prevent the measurement from being disturbed by the electrode polarisation this voltage is applied with respect to the open circuit potential, and ideally performed in a 3 electrode cell. However, it may be necessary to perform measurements using only two electrodes depending on the effect that is of interest and the cell geometry.

Measurements are performed by sweeping the applied AC potential from high to low frequencies, e.g. from 10^5 – 10^{-1} Hz. The upper frequency is limited by the capacitance of the measurement system, especially in configurations using only two electrodes. At lower frequencies the limit is set by the requirement to complete the measurement in a timely manner, and cell drift.

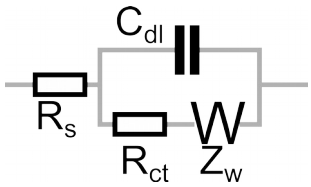

Figure 5.1: Randles cell diagram. Its individual components may for example be interpreted to mean the series resistance, R_s, which covers e.g. the electrolyte resistance and resistance in leads and connections; the charge transfer resistance R_{ct} which describes the polarisation of the electrode resulting from a Faradayic reaction; the Warburg tail associated with diffusive resupply at low frequencies, Z_w; and the double layer capacitance C_{dl}.

EIS data is commonly analysed by setting up an equivalent diagram which maps the electrochemical measurement onto electrical components that are combined in series and parallel. One of the most commonly used cell blocks for analysing EIS spectra is the Randles circuit (Figure 5.1), which allows one to infer the electrolyte resistance and the active area of the electrode.

Method

In order to maximise the relative change in conductivity a dilute pH-neutral electrolyte was chosen. Different aerated electrolyte solutions were prepared with ultrapure water and KCl in various concentrations. The water conductivity was measured using a Adawa Instruments AD8000 in still solutions after stirring the submerged probe in the solution to ensure no air bubbles were trapped inside the probe sheath.

Measurements were performed using the EC-SEM cell discussed in chapter 3 with gold electrodes, 50 nm thick on 10 nm titanium. As in the previous experiments the lithographically defined gold

electrodes are placed on a nominally 50 nm silicon rich low stress nitride membrane, and the electrochemically active area is defined by SU8 epoxy-based photoresist.

Electrochemical measurements were performed after flushing repeatedly with purified water, and during the control measurements care was taken to always go from lower to higher concentration. In order to minimise the polarisation resistance the largest on-chip electrodes with 10 µm by 40 µm exposed area were chosen, the distance between which was 75 µm. During in-situ experiments the area between adjacent electrodes was irradiated in order to form a relatively homogeneous channel through which to measure the conductivity. CASINO simulations shown previously (Figure 3.4) suggest that irradiation at 25 kV reaches down to 10 µm, which thus defines the extent of the immediate conductive channel. During irradiation this channel is spread out due to diffusion, but for short lived species such as solvated electrons this extended region will be of with a different composition relative to the immediate conductive channel.

EIS was performed in 2-point configurations with adjacent electrodes. Experiments in four-point configuration did not succeed due to instrument compliance voltages, at which there is a risk of electrolytically forming ionic species which could interfere with the measurement due to the relatively small area of the source-drain electrodes. In-situ EIS was performed with the beam continuously irradiating between the electrodes to make sure that the conductive channel did not diffuse away.

In-situ experiments were performed in an FEI Inspect S tungsten filament SEM operated at 25 kV in low vacuum mode. Imaging was performed using the FEI LFD detector, which detects the electron-induced cascade amplification in the water vapour. Different beam currents were tried incrementally from low to high.

Calibration measurements

EIS of electrolytes with a known conductivity will allow us to make a calibration curve that will later be used to determine the conductivity of irradiated water. For this purpose we used a purified water supply mixed with a set of known KCl concentrations. In the ideal case the resistivity of pure water is 18 MΩ·cm, but on exposure to air this eventually drops to around 1 MΩ·cm due to the dissolution of atmospheric CO_2.[87]

Measurements of the water supply resistivity were limited by the measurement setup to >16 MΩ·cm (0.06 µS/cm) when flowing past the conductivity meter, but when left still in the beaker it recorded a higher conductivity of 0.2 µS/cm. This is likely due to a combination of gas from the air (carbonic acid from dissolved CO_2) and ionic species leaching from the measurement probe and glass.[3] The recorded value was stable at the time of the measurement. The conductivity of the different dilutions of KCl correlated very well with the concentrations, as seen by the log-log linear fit (Figure 5.2).

3 Stirring the probe in the solution typically gave a temporary reduction in the conductivity reading, indicating that CO_2 is not the exclusive reason for increased conductivity.

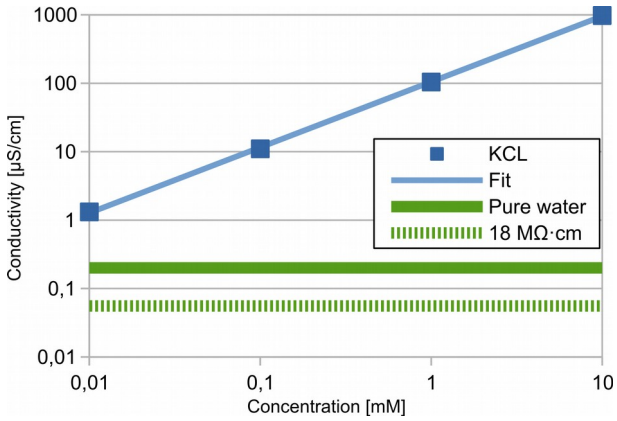

Figure 5.2: Conductivity of solutions used for EC-SEM EIS calibration. The blue line is obtained by linear regression to the log-log transformed data. The solid green line represents the measured conductivity for pure water, while the dashed line indicates the theoretical limit.

Measurements performed in the EC-SEM cell using these different concentrations show that at as conductivity goes up both the impedance and the phase angle are consistently reduced at low frequencies, even though the sensitivity is small (Figure 5.3 indicates a ~30% increase in impedance when conductivity decreases by two orders of magnitude). By plotting the measurements recorded at 100 Hz we obtain an empirical relation between the impedance and phase vs the electrolyte conductivity.

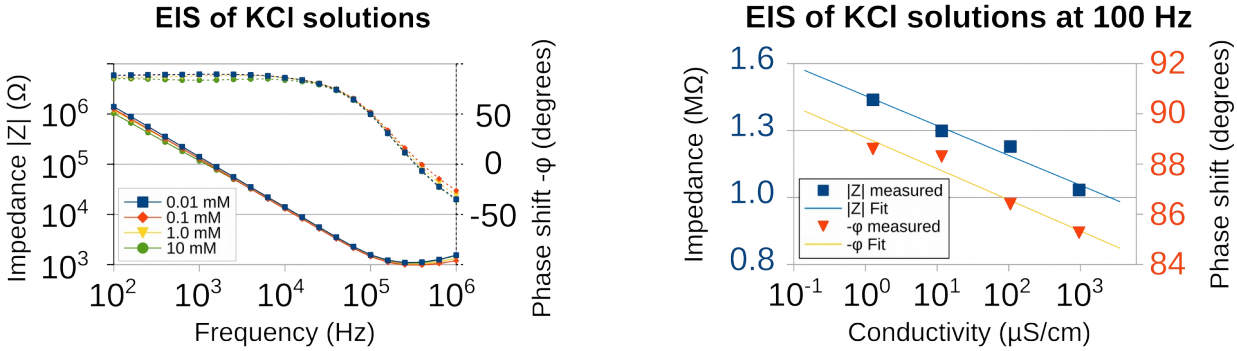

Figure 5.3: Left: EIS spectra for different concentrations of KCl injected into the EC-SEM cell. A reduction in the impedance was seen to be associated with higher concentrations of KCl. Right: Plotting the impedance and phase measured at 100 Hz at the four different irradiation intensities gives a calibration curve that can be used later to estimate the electrolyte conductivity during irradiation.

Because the SEM does not report the beam current directly it was measured immediately after the in-situ experiments in high vacuum mode. We have measured the beam current on several occasions, and it follows a logarithmic profile with increasing *spot sizes*. Since the exact current depends on the alignment and configuration of the microscope we measured three spot sizes immediately after our experiments, and infer the current for intermediate spot sizes by means of a linear regression of the log-transformed measurements (Figure 5.4).

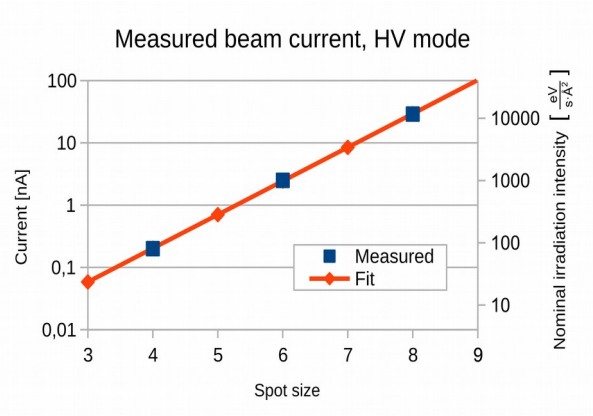

Figure 5.4: The beam current profile for the FEI Inspect has been configured to be logarithmic. We measured the spot sizes 4, 6 and 8 and infer the values for spot size 5 and 7 based on a linear fit to the log-transformed data. Measurements were performed using the integrated equipment linked to the EDX and using the stub holder as a faraday cup. Since the measurement is affected by the contrast setting of the detector in low vacuum (LV) mode the current was recorded in high vacuum (HV) since this current remains representative for LV at low pressures. Current density is calculated using an area of 75 µm by 50 µm.

During irradiation the region of interest is aligned to the area between two adjacent electrodes spaced 75 µm apart, scanning a width of nominally 50 µm, which for the beam currents used in this study results in a power density ranging from 84 to 3500 eV/(s·Å^2).

In-situ results

Measurements performed in-situ show no appreciable change in impedance or phase angle at frequencies higher than approximately 10^3 Hz. Near 100 Hz we see a consistent shift towards lower phase angles and a trend towards lower impedance for higher irradiation intensities, with the difference between high and low intensity increasing as frequencies decrease (Figure 5.5). Comparing with the calibration curve in Figure 5.3 this is consistent with an increase in effective electrolyte conductivity. However, at very low frequencies measurements become problematic due to the measurement time required to reduce noise and due to limitations of the potentiostat current range.

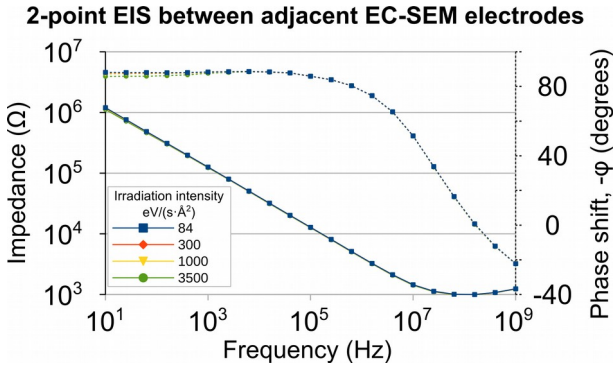

Figure 5.5: Impedance and phase angle both see a slight drop upon irradiation that is consistent with increasing spot size. The change is most noticeable at low frequencies between 100 and 1000 Hz.

Looking exclusively at the impedance measured at 100 Hz we find that the beam induced reduction in impedance – compared to the measurement at the lowest irradiation intensity – increases progressively with increasing irradiation intensity (Figure 5.6 Left). The relative difference is mostly constant in the range 10^2 to 10^4 Hz. For the data measured at 300 eV/(s·Å^2) we see what appears to be digital noise, i.e. aliasing due to the analogue to digital conversion. It is likely that this effect would be largely reduced or eliminated by reducing the current range, however that would require several more experiments to eliminate current overload errors in parts of the circuitry that is not directly controlling the cell.

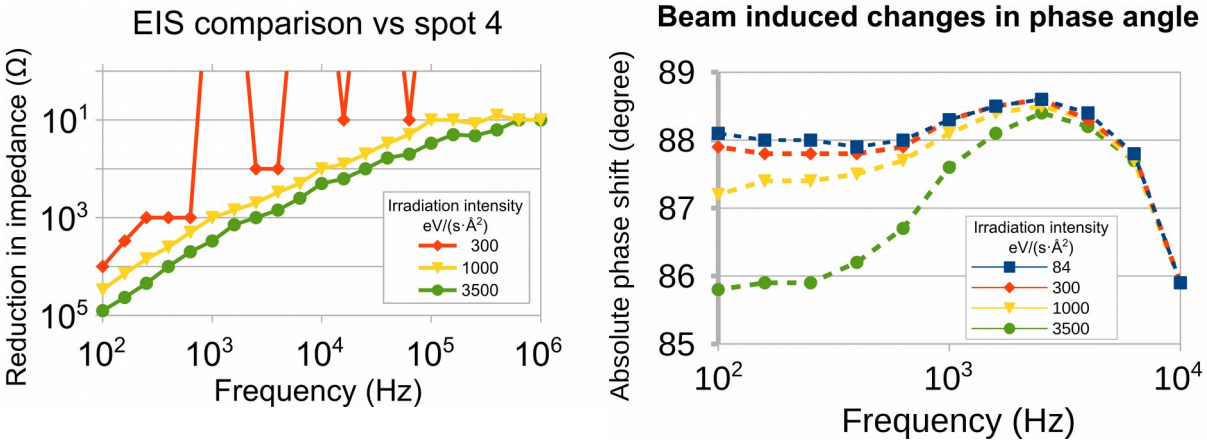

Figure 5.6: Left: Absolute differences in impedance compared to measurement at 84 eV/(s·Å^2). The relative difference is largely constant in the range 10^2-10^5 Hz. Aliasing observed at 300 eV/(s·Å^2) is due to the potentiostat ADC at this current range. Right: The phase angle is reduced significantly by higher irradiation intensities, suggesting a higher conductivity of the irradiated electrolyte.

We also observe that the phase angle decreases distinctly with increasing irradiation intensity (Figure 5.6 Right), indicating a higher electrolyte conductivity. For frequencies between 10^0 and 10^2 Hz this phase shift is progressively reduced as far down as 55°, increasing the sensitivity of the method at the cost of measurement time and the risk of being limited by the potentiostat current range.

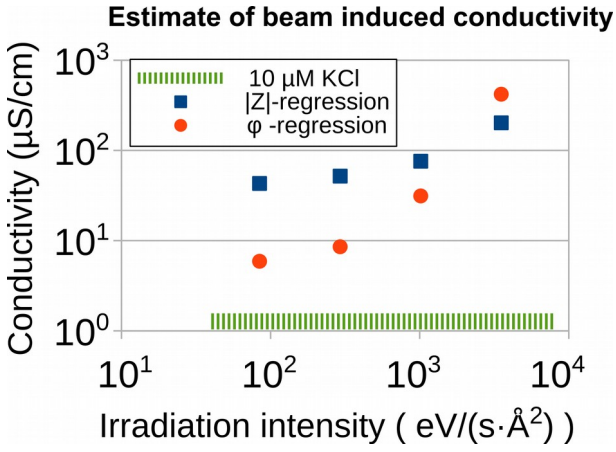

Figure 5.7: There is a steady increase in conductivity associated with an increase in irradiation intensity, although the magnitude is not entirely consistent between impedance- and phase-based regression. Regression based on impedance measured at 100 Hz.

By combining the in-situ measurements in Figure 5.6 with the ex-situ calibration curve in Figure 5.3 we obtain a plot over the expected electrolyte conductivity depending as a function of the irradiation intensity, shown in Figure 5.7. The inferred values based on both impedance and phase show a trend of higher conductivity with higher beam irradiation intensity, and the magnitude is similar at intensities of 10^3 and 10^4 eV/(s·Å^2). At lower intensities the curve based on impedance flattens out to a high conductivity compared to the unirradiated electrolyte, while the conductivity based on the phase angle is observed to be one order of magnitude lower.

Discussion

In order to determine the conductivity of the SEM irradiated electrolyte the electrochemical cell and method must be characterised with different reference solutions. We do that by performing 2-point EIS of dilute KCl solutions with gold micro-electrodes. The conductivity of all the KCl solutions was at least 10x that of pure water, and was proportional to the dilution ratio.

The measurements show that we may be able to discern the difference in conductivity between KCl mixtures of 10 µM and 100 µM by focusing on the lower frequency range. A more distinct difference is visible between solutions of 100 µM and 1 mM. These concentration limits are comparable to the peak concentrations of radiolytic species expected from beam influence.

EIS measurements were stable and reproducible, but for low frequencies it was essential to use a longer acquisition time than default to prevent noise. Noise was easily recognised as it deviated randomly from the otherwise smooth curve when plotting the data. By combining the EIS data with the conductivity measurements of the KCl solutions we obtain a calibration curve relating the impedance ($|Z|$) and phase shift ($-\varphi$) to electrolyte conductivity.

By localising the irradiation between two adjacent electrodes a conductive channel is being formed which can be measured by means of EIS. The interaction volume of the irradiated region is roughly one order of magnitude smaller than the electrode spacing, which would imply that where the beam strikes a local volume is made conductive, but before the beam has continued scanning to all the way from one electrode to the other the transient species may already have recombined since the beam dwell time (time per pixel) is on the order of 10^{-6} s, at which time there is only a limited set of reactive and ionic species left.[16] Since a frame may take from several tens of milliseconds to about a second to scan only the longest-lived species (e.g. H_3O^+) should be able to contribute to form a cohesive channel.

At the highest beam current, 8.5 nA, the frame-averaged radiation intensity in this channel is approximately 6 MGy/s. We observed a small but consistent change in the impedance as irradiation intensity increased from 0.1 MGy/s to 6 MGy/s. The change in the phase shift was markedly more distinct, and in EIS scans extending down towards 1 Hz the difference between the lowest and highest irradiation intensity was very large – 80° vs 55°.

When calculating the conductivity of the irradiated solution based on the KCl calibration we find that although there is not complete agreement between the estimated conductivity based on

impedance and phase at low irradiation intensities, there is indeed a consistent increase in conductivity with increasing irradiation intensity. At the highest irradiation intensity (3500 eV/Å^2, 6 MGy/s) we estimate the electrolyte conductivity to be approximately 200 µS/cm (impedance-based) to 400 µS/cm (phase-based). This is equivalent to a 2 – 4 mM KCl-solution, or a ~0.1 mM HCl solution.

Additional experiments may be required to determine which of the two calibration curves is more applicable. For example, by varying the distance between the adjacent electrodes it should be possible to determine if the observed conductivity scales with the length of the conductive channel. Comparing results at different AC potentials (increasing it from 10 mV to 20 mV) would indicate whether the SEM beam current which is directed to ground through the electrodes is affecting the result. And varying the DC potential between the WE and CE could allow this condition to be simulated ex-situ.

With these caveats in mind our results establish a lower limit on the beam influence, because the irradiated geometry is confined. In normal EIS the electrolyte is homogeneous around the two electrodes, and as a consequence the current profile is merely the superposition of a current source located at each of the two electrodes, and thus a non-negligible contribution to the current is spread into the bulk of the liquid. During irradiation a highly conductive channel is formed in the confined region between the two electrodes, and to obtain a certain increase in average or bulk conductance this irradiated region must be significantly more conductive.

It remains an unanswered question exactly which species are the cause for such a high conductivity: Upon electron beam irradiation the electrolyte conductivity will increase due to the formation of charged species such as H^+ and – transiently – dissolved electrons. The conductivity of different ionic species varies, and for H^+ it is particularly high due to H_3O^+ not moving as a unit through the water, but rather the proton hopping from one water molecule to the next.[88,89] Similar to H^+, both OH^- and the hydrated electron also exhibits a high molar conductivity compared to ions from traditional salts.[90]

Based on the Schneider prediction for the small nanoaquarium cell the steady state pH-value of the irradiated region when subjecting it to 6 MGy/s is reduced to 5.5,[18] which corresponds to a conductivity of only 1 µS/cm.[91] In an aerated solution they predict an additional 20% increase in conductivity. As such, H^+ formation is not sufficient to explain our high conductivity.

The instantaneous irradiation intensity is much higher depending on which volume one chooses to normalise to, but is at any rate at least on the order of 10^8 Gy/s, going as high up as several teragray per second if one looks at the area where the first 50% of the power is dissipated (discusses in further detail previously, see Figure 3.4). Although Schneider et al. predict that a higher irradiation intensity results in a higher concentration of H^+ (and thus higher conductivity), they also predict that the concentration drops rapidly outside the irradiated region (one order of magnitude reduction within a few µm from the TEM spot).

Because of Schneider's low prediction of H^+ and hydrated electrons it is puzzling that we observe such a distinct increase in conductivity. We hope that by performing additional experiments we would be able to identify a relevant decay time scale and distance from the irradiated region. In this way we would be better able to determine which combination of radiolytic species give rise to this result.

Specific experiments worth including could be single-frequency EIS around 100 Hz while the scanning electron is alternatingly blanked. In this way it would be possible to determine if the conductivity of the electrolyte decays according to a time-scale corresponding to diffusion or if there are additional effects at play, for example chemical reactions. Another relevant experiment would be to defocus the electron beam sufficiently for the electron beam to strike the membrane at random locations between the two electrodes in order to more closely match the assumptions by Schneider et al., although this would inevitably come with a significant reduction in the beam current that makes it all the way to the liquid (and is not stopped by the silicon chip instead).

To rule out any direct influence from the beam it would also be necessary to perform EIS under equal conditions at different perturbation voltages. Not only does the beam produce charged species, in thick cells as those used here for SEM the entire beam is absorbed which results in a constant current that must be conducted to ground. A real change in electrolyte conductivity should result in the same measured impedance and phase when increasing the perturbation voltage.

Conclusion

The electron beam used for imaging during in-situ electron microscopy causes a change in the chemical composition of the electrolyte by splitting it into a host of different radicals and ions which can then recombine into new species. As a result of this process the electrical conductivity of the electrolyte will also change, potentially affecting the outcome of in-situ experiments.

In an attempt to better understand this process we have performed electrochemical impedance spectroscopy between two on-chip electrodes before and during electron beam irradiation. Without irradiation we determined that different conductivities are most easily distinguished using measurements 100 Hz. Both the phase and absolute impedance change as a function of conductivity. When irradiating an electrolyte containing 10 µM KCl we found that the apparent conductivity goes up as the beam irradiation intensity goes up (determined by increasing beam currents).

There is a discrepancy between the estimated electrolyte conductivity based on impedance and based on phase, especially at low irradiation intensities. It remains an open question for now exactly why this discrepancy is there. At the highest irradiation intensity we attempted, 3500 $eV/(s \cdot Å^2)$, there is reasonable agreement between the two methods of determining the conductivity, and we estimate it to be between 200-400 µS/cm. To obtain such a high conductivity from an acidic solution a concentration of e.g. HCl would have to be on the order of 0.5 – 1 mM.[91]

Schneider et al. provides the best estimate on radiolytic concentrations for TEM cells to date and attempts to take into account the many possible reaction pathways of radiolytic products. However, the concentrations they arrive to disagree with the prediction by Woehl et al. who expect a higher concentration of hydrated electrons. Schneider et al. point out that much of the literature relating to radiolysis has to be extrapolated by as much as 7 orders of magnitude to reach the high sustained radiation intensities in electron microscopes, which means that predictions such as theirs can be deviating significantly from experimental data.

When applying the predictions by Schneider et al. we find that with our frame averaged irradiation intensity of up to 6 MGy/s the obtained conductivity is too high to be accounted for solely by H^+ or hydrated electrons. Although the equivalent concentrations required to reach the measured radiolytic conductivity, e.g. 2-4 mM KCl or ~0.1 mM HCl, match with the peak concentrations predicted by Schneider, the compounds which reach such high concentrations are mainly H_2 and H_2O_2 which are not ionic, and should not contribute significantly to the conductivity at such low concentrations.[92]

Although we obtain a reasonable correlation between conductivity and radiation intensity we find that the measured conductivity is higher than what Schneider's prediction alone would suggest. We are as of yet reluctant to conclude which is more accurate, and therefore deem it necessary to reproduce the experiment with different electrode spacings and irradiation regions in order to better describe the electrochemical processes which occur. Reproducing the experiment in a TEM or other instrument which has an even irradiation instead of rastering would also eliminate some of the difficulties in interpreting the data.

Chapter 6: In-situ SEM determination of copper G-values and observation of beam-induced anomalous electroplating of copper

Preface – in-situ SEM electroplating of copper

Copper plating is a good process to use as model system for in-situ experiments. It is a topic which has received a lot of attention in previous studies due to its large importance in the industry, both to form a conductive layer for e.g. microchips, and to create a seed layer for other forms of electroplating.

Copper electroplating is by no means a new invention. Studies on how to create quality coatings of copper date back to the 19th century,[93] and inventions regarding copper plating have been awarded patents more or less continuously since. Since those early times it was known that the current density[94] and differences in electrolyte composition both affect the quality of the coating.[95,96] With the advent of high frequency microprocessors with very high thermal outputs in the late-1990s there was a push to replace the aluminium interconnects with electrodeposited copper due to better thermal and electrical performance.[97] With the push to create ever smaller features in copper (such as the Intel Pentium 4 “Northwood” which was created on the 130 nm node) the value of understanding the initial growth has gone up.

Since then there have been examples of in-situ electron microscopy being used to study copper electroplating. Traditional studies have determined that the electroplating quality depends on electrode surface finish,[98] electrolyte composition[99] and electroplating conditions. In-situ TEM studies show that the growth takes place with a higher than predicted nucleation density, suggesting a process involving the formation and surface diffusion of adatoms.[100]

The stability of various chemical forms of copper can be determined from a pourbaix-diagram. The diagram shown in Figure 6.1 Left indicates that at acidic pH-values only metallic and ionic copper may exist,[101] leading to a direct dissolution instead of the formation of non-soluble substances. If excessively negative potentials are applied there is a risk of forming hydrogen gas by radiolysis (dashed line). Conversely, positive potentials may cause the formation of oxygen.

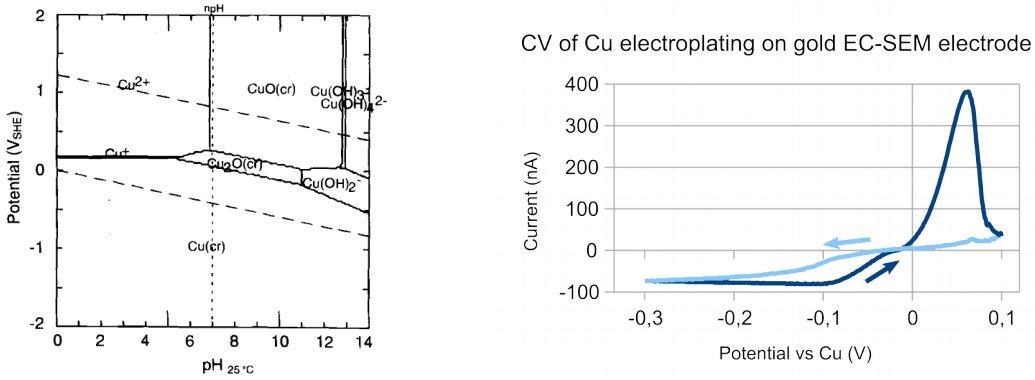

Figure 6.1: Left: Pourbaix diagram of copper by Beverskog and Puigdomenech (1997). In acidic solutions metallic copper is formed by reducing the potential below the $Cu_{(s)}/Cu^{2+}{}_{(aq)}$ border.

Right: Typical cyclic voltammogram of copper solution on the EC-SEM micro-electrodes. Although copper plating can occur at any potential less than 0 V_{Cu} a certain overpotential is needed to form the necessary seeds. Copper dissolution is rapid, as indicated by the rapidly increasing current when sweeping past 0 V_{cu} (dark curve) . This continues until all electrically connected copper is etched away, although a significant loss may occur if the copper is porous since the copper can be etched from the interface resulting in loss of contact.

In our in-situ experiments on copper plating on gold we use a copper wire as the reference electrode. Such a reference electrode is particularly suitable because the exact potential at which electroplating occurs depends on the electrolyte concentration. The wire is situated in the same electrolyte, and as a result the zero point for electroplating and dissolution is 0 V vs the Cu/Cu^{2+} pair. However, a certain overpotential is needed to form nucleation points on the gold electrode to which the copper may attach (Figure 6.1 Right).

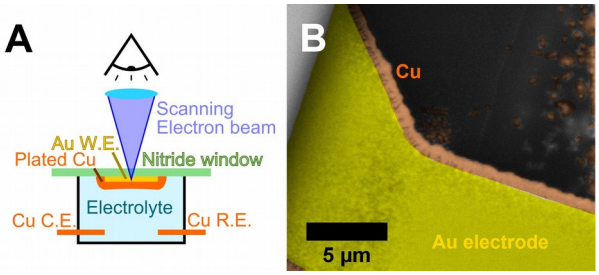

Figure 6.2: A: The electrochemical cell consists of an opaque gold electrode on a transparent silicon nitride membrane. Copper wire electrodes serve as both counter- and reference electrodes. B: In-situ image after growth. The smallest features in this image are less than 100 nm *across. The speckled brightness of the gold electrode seen under the SU8-layer is due to the SU8 limiting diffusion and growth of copper.*

Electroplating was performed in-situ SEM by applying negative potentials on the microelectrode relative to the Cu reference electrode. At high magnification it can be seen that the structure of the copper contains cavities which may be due to excessive plating current density (Figure 6.2B). The image also shows a faint line where the SU8 protective resist is compared to the electrolyte, and that it on this chip has delaminated as evident by the gradually decreasing plating thickness below it. The smallest copper grain seen to the side of the electrode measures less than 100 nm, which is approaching the resolution reported by Schneider for a TEM system[55] despite being taken with a tungsten filament SEM.

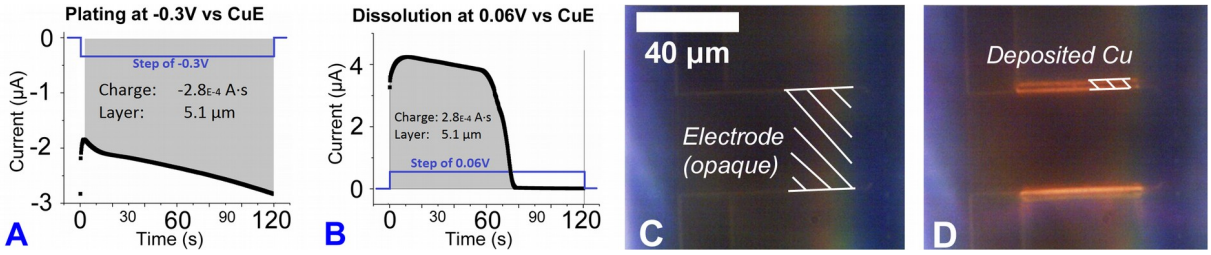

Figure 6.3: A and B: During electroplating and dissolution there is a good faradayic efficiency, as indicated by the small difference in total charge used to deposit copper. C and D show how the copper layer becomes visible in darkfield optical microscopy as it expands beyond the opaque gold electrode. Chronoamperometric measurements by S. Colding-Jørgensen.

During normal electroplating copper forms a dense structure on the electrode that gradually extends outwards in all directions. When performed in this way a very high faradayic efficiency can be attained if the layer is subsequently dissolved by applying a positive potential (Figure 6.3).

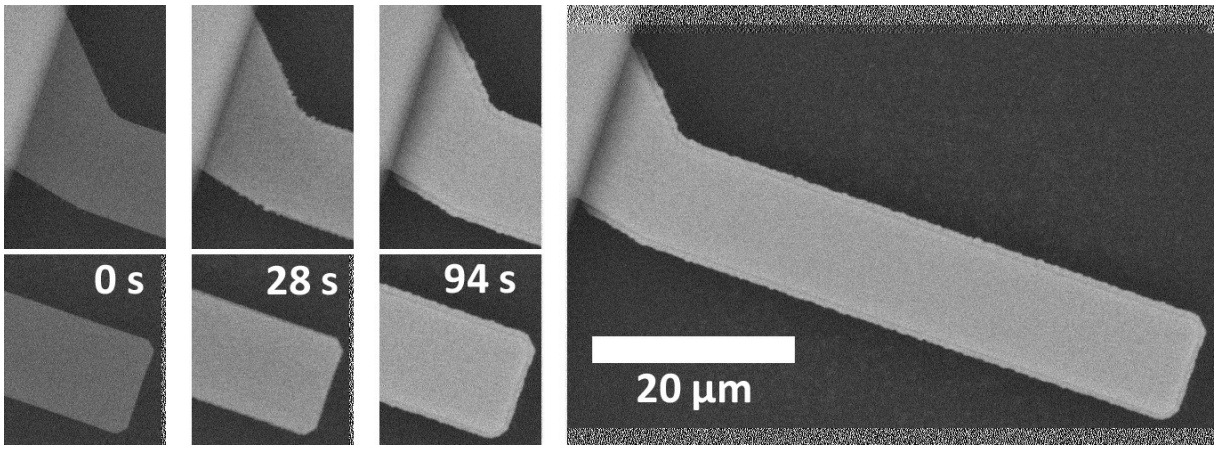

Figure 6.4: Three stages of in-situ SEM electroplating at -0.2 V vs Cu on a micro-electrode. All images show the same electrode, with top showing the innermost part of the electrode and the bottom image sequence the tip. As more material is plated on the electrode even the center becomes brigher.

In situ image series (Figure 6.4) demonstrate that it is possible to see the electroplating through the 50 nm gold electrode, as evident by the much higher brightness in plated areas. Plating appears homogeneous, although the edge becomes rougher as plating continues. At positive potentials the bulk of the copper is dissolved quickly, leaving behind small grains which are observed to disappear much slower (Figure 6.5). This suggests that some particles have poor connection to the electrode

and experience a high ohmic potential drop. It is likely that the copper layer is to some extent under-etched – especially if it is porous or dendritic, exacerbating the effect of disconnected grains.

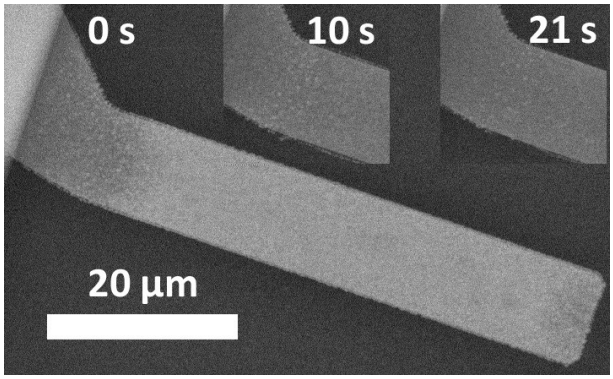

Figure 6.5: During dissolution the bulk of the material is quickly removed (a couple of seconds), leaving behind small dendrites that take several tens of seconds to remove. These structures are visible even through the 50 nm *Au on 10* nm *Ti electrode. This image sequence was recorded at +60* mV_{Cu}.

SEM-investigation of the electroplated electrodes after rinsing and drying the chip showed several different surface qualities, ranging from dendritic, to extremely porous and finally solid with inclusions of voids (Figure 6.6). This suggests that the electrodes were subjected to too high a current density, either as a result of different electrode contaminants or different degrees of beam irradiation. When the current density is too high for too long the electrolyte becomes depleted, and the dendritic structures appear as the diffusing copper ions are immediately reduced upon contact – as opposed to finding the most favourable position.

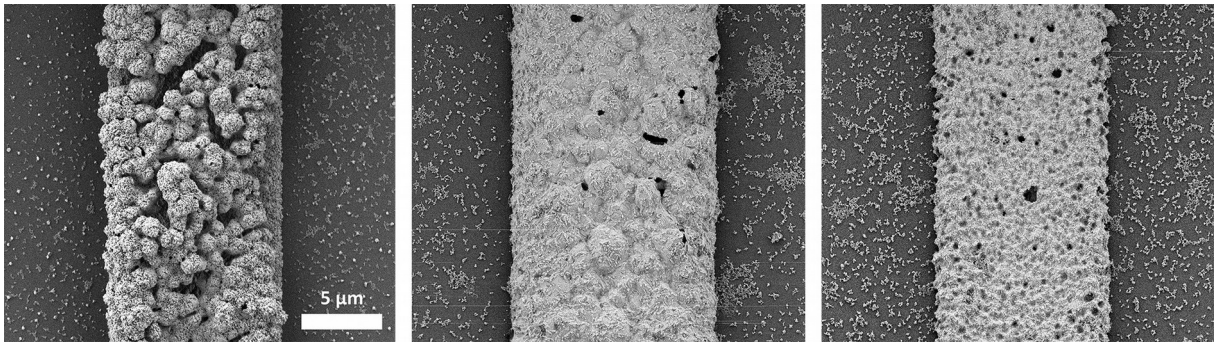

Figure 6.6: Three different surface morphologies during copper electroplating. The differences are likely to be the result of different plating rates, for example because of different degrees of surface nucleation and beam assisted plating. The particles surrounding the electrodes are copper pieces that have lost connection to the bulk material. (All images are to the same scale).

In summary the in-situ SEM cell provides high resolution images that is close to that obtainable with liquid TEM, but with the additional advantage of a dedicated reference electrode. Experiments demonstrate that we obtain high contrast during in-situ electroplating and dissolution of copper on a gold electrode. The following text describes the characterisation of the electron beam influence on a copper electroplating solution. A good understanding of the beam influence is important in order to correctly isolate the effect of the applied potential on the electroplated nanostructure.

Introduction to the study of radiolytic yield of copper

In-situ electron microscopy studies of electrochemical processes seek to utilize the observational power of high resolution imaging from electron microscopy to study electrochemical processes. Suitable processes are those where the electrochemical process exhibits a change that can be observed with the electron microscope, whether that is volume change,[102] or changes in the crystal structure.[103] Since the first electrochemical in-situ EM studies using ionic liquids the field has seen tremendous growth, and will likely continue to do so now that there are several commercial systems enabling electrical contacts inside vacuum compatible and electron transparent wet cells.

However, with the increase in such electrochemical studies it becomes ever more important to account for the influence the electron beam has on the experiment. Electrons may for example create radicals,[16] oxidise or reduce ions to the neutral state[19] or etch metals,[53] split water into gas,[19] cause polymerisation[67] and change the pH.[18] In general, radiochemistry is a very complicated field where even seemingly simple reactions turn out to have many alternative paths.[31,83]

A number of studies have reported on the behaviour of electrochemical systems when subjected to irradiation. In-situ TEM was used to observe the initial stage of copper electroplating, where copper seeds are formed.[104] The study revealed a large difference in the nucleation density compared to the model expectation, a discrepancy which they hypothesized was due to adsorption of copper onto the surface prior to nucleation and growth.

In a different TEM study, also performed with acidic copper sulphate solution, it was observed that electrochemical plating was assisted by the electron beam:[105] Upon addition of a small amount of chloride ions there was a range in applied potential within which nucleation and growth would only take place in those parts of the electrode which were irradiated.

Nucleation and particle growth can even be observed in systems without electrical contact, whether that is the reduction of cupric ions to copper from a chloride-containing sulphuric acid electroplating solution,[105] or silver,[53] or lead,[106,107] or gold.[20,108] Etching can also occur.[53] To date the perhaps most elaborate theoretical study in the potential effects of electron beam radiation on liquid samples was performed by Schneider et al.,[18] who used the existing G-values for various radiolytic water products to estimate the time-dependent concentrations of the various compounds resulting from electron beam radiation, most notably H_2, H_2O_2 and H^+.

Heijer et al.[105] observed that for acidic copper sulphate solutions containing chloride ions nucleation was inhibited at small negative potentials, but interestingly regions subjected to focused electron beam irradiation exhibited an uninhibited growth. In an electrolyte without Cl^- there was only a very small difference in electroplating rate, which they attribute to localised heating. They argue that Cl^- may form a monolayer of CuCl when depositing at low potentials, and which inhibits further growth. This layer is then reduced to metallic copper by the electron beam irradiation, onto which further copper growth may commence at smaller overpotentials than without the beam.

A direct study of the radiolytic yield of metal (reduced from metal ions) does not exist for SEM or TEM. Instead the studies to date have described such reduction in terms of e.g. the accumulated beam charge in a spot, or the current densities at which precipitation occurs. In a TEM-study, platinum particles have been reduced from dissolved salts by means of high current densities during imaging (equivalent to 5 – 30 GGy/s).[109] Based on their reported data we can calculate their effective g-values (depending on which of their reported beam current densities the data set is for) to be between 0.005 and 0.04.

The present study is a step in elucidating the radiolytic processes happening under the conditions prevalent in electron microscopy wet cells. Specifically, it is a study in the direct influence of the electron beam in a scanning electron microscope on copper reduction. And since radiochemistry is linked to the energy absorbed by the liquid the results are directly relevant for scanning transmission electron microscopy (STEM) as well, and with some additional reservations also for conventional transmission electron microscopy (TEM).

Method

We used the electrochemical in-situ SEM cell previously described by Jensen et al.,[14] which was modified to have two pure copper wires as the reference and counter electrode. The electrolyte was 0.80 M $CuSO_4$ in 0.46 M H_2SO_4, and was not degassed. Working electrodes were available on the microchip, and consisted of 50 nm Au on a 10 nm Ti adhesion layer, with regions covered in SU8 photoresist in order to more accurately define the active electrode area. The electrodes were on an electron transparent 50 nm silicon-rich low-stress nitride membrane.

Radiation induced nucleation was done on the membrane in regions without electrodes. Electrochemical plating and beam-assisted electrochemical plating was performed on electrodes by chronoamperometry using an Ivium CompactStat potentiostat. The potential was first set to +0.150 V_{Cu} in order to eliminate any copper deposited by imaging with the electron beam, or other contamination. Immediately afterwards the potential was reduced to -0.075 V_{Cu} in order to perform electroplating.

Beam-assisted electroplating was done with a region of interest which closely fitted to a small segment of the electrode, so that the irradiated area could more easily be recognised.

Radiation-induced nucleation was studied by irradiating an area of the membrane continuously for 60 seconds, while storing an image approximately every 5 seconds. The sample was then moved to access a new region of the membrane far away from the previously irradiated area, while at the same time reducing the size of the scanned area. By reducing the scanned area different frame-averaged radiation intensities were recorded (i.e. electron beam current densities at the sample).

Irradiation was performed in an FEI Inspect tungsten-filament scanning electron microscope in E-SEM mode with 10 Pa of water vapour to reduce the chance of charging, but since the cell was sealed off the pressure inside the cell itself remains at close to 1 bar. Backscattered electrons were

recorded with a gaseous secondary electron detector (FEI Large Field Detector, LFD). Secondary electrons in E-SEM mode are also created by backscattered electrons,[49] and since the top surface of the membrane is featureless the contrast in the signal is initally caused by backscattered electrons. The microscope was operated at 25 kV with a beam current (measured with the built in equipment in high vacuum mode) of 0.20 nA. We have measured separately that similar values are found with 0 V on the LFD in E-SEM mode. The FEI Inspect beam is only irradiating the region of interest and not outside it.

In order to determine the quantity of copper based on the backscatter signal we observe the change in backscattered signal averaged over the region of interest. Since metallic copper is far more dense than dissolved 0.8 M copper ions we obtain a contrast in the image, and this increase in backscattered electrons can be quantified and related to the deposited Cu. We looked at electrochemically deposited copper on gold under identical imaging conditions and correlated the average backscattered signal with the increasing electrochemically imposed charge density (Figure 6.7). Since the amount of copper is known from the electrochemical measurement through Faraday's law we now have a correlation between intensity change and quantity of copper. The experiment was performed twice, resulting in an average slope of $3.45 \cdot 10^{-3}$ pxval·(#Cu/Å^2)$^{-1}$, with the two measurements differing by less than 2%. There was no clipping or saturation in the source images for this calibration.

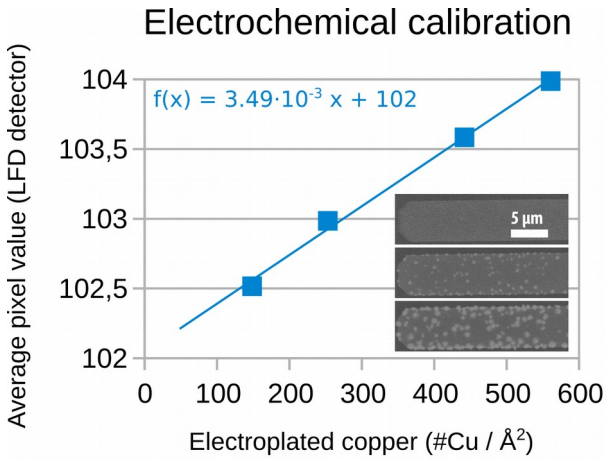

Figure 6.7: Calibration was performed by scanning the beam across an electrode (inset) and plotting the mean intensity vs the amount of chronoamperometrically deposited copper. The amount of copper was normalised to the electrode area, using the resulting slope as the correlation between copper density and change in image intensity. Electroplating experiments were performed in chronoamperometric mode in two steps; first a dissolution step at +0.15 V for 30 s to dissolve any copper seeds that might have been nucleated by for example the beam, followed by a plating step at -0.075 V. Irradiation was limited to single images (as opposed to continuous irradiation) of a confined area, such as either one single electrode, or a limited part of an electrode. Potentials are reported with respect to the copper wire reference electrode.

Using the slope as the calibration measure to find the final radiolytic yield eliminates certain types of errors, such as those causing a shift in the curve: The gold electrode provides a constant

background signal, causing a vertical shift in the curve. Also, any leakage current before copper nucleation on the electrode will induce a horizontal shift in the curve.

Results

G-value for $Cu^{2+} \rightarrow Cu$

The backscatter intensity resulting from beam-induced nucleation on the membrane was observed to be linear with the irradiation dose across several different recording sequences at different irradiation intensities (Figure 6.8). By employing the slope from the previously measured calibration measurement we can transform this into a plot of number of metallic copper atoms per electron, both normalised to area. And since effectively all the incoming beam energy is deposited in the sample (no transmission and negligible backscattering)[14] we can describe the x-axis in terms of the deposited energy per unit area by multiplying the number of electrons per area by the acceleration voltage.

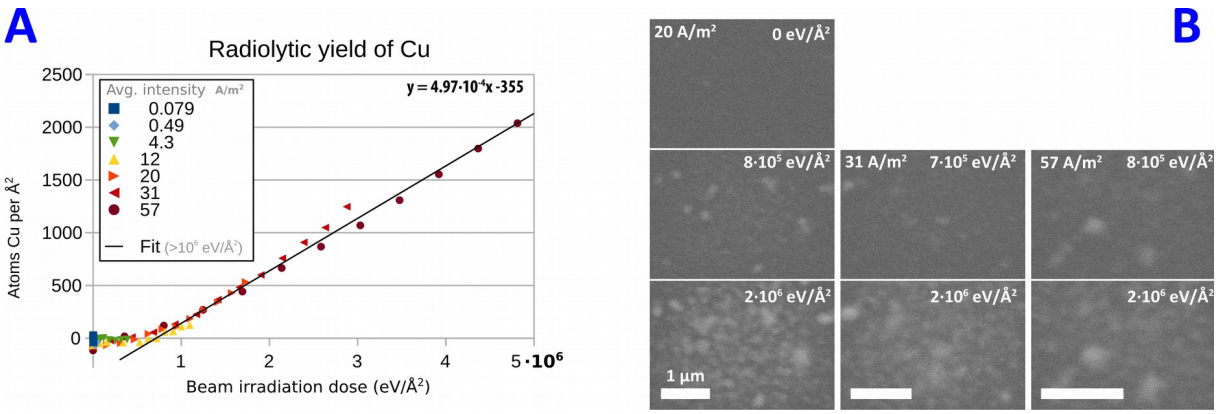

Figure 6.8: A: The observed radiolytic yield appears to behave linearly with accumulated dose, independent of beam intensity (modulated by changing the area). B: Images of the radio-nucleation at increasing intensities by changing magnification (columns) and doses by increasing time (rows). Bright spots correspond to backscattered electrons from copper deposits.

From the resulting graph we find a linear relation between the amount of energy deposited and the amount of copper converted from cupric ions at high doses. In order to determine a lower bound on the G-value – the quantity of a specific radiolytic species that is produced per 100 eV deposited – we take the slope of all measurements in the linear regime at intensities exceeding 1 MeV/Å^2 to obtain a G-value of 0.050 atoms Cu per 100 eV. Copper which is reduced but not adhering to the membrane will not be measured and hence this is a lower limit of the g-value.

Of particular note is the apparent threshold observed at 29 electrons per square Ångström (fit intercept with the x-axis) below which we did not observe any change in image intensity (Figure 6.9).

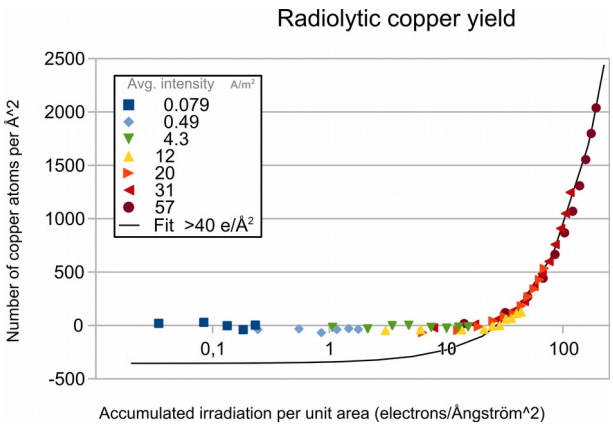

Figure 6.9: Below a threshold dose there is no observed change in detected radiolytic copper, regardless of beam intensity. The threshold value appears independent of beam intensity, suggesting that it is not a time- or dose rate dependent effect.

The exact cause for a threshold value is not certain. One of the effects that could be in play is diffusion of reduced species into the bulk of the liquid or etching of such reduced species by sulphuric acid. However, both of these effects are time-dependent and as such fit very poorly with the data where the onset was at constant dose, but depending on the dose rate at different time.

For example, since copper diffusion is relatively fast (characteristic length on the order of 150 µm for the 60 seconds irradiation)[110] the required threshold dose should vary with the dose rate due to diffusive loss of radiolytic material. We observe no such difference between different dose rates, and must conclude that the threshold value is not dominated by diffusion. Similarly, it cannot be due to e.g. dissolved oxygen etching away copper seeds until the oxygen supply is depleted, since such a depleted region would be recovering with a diffusive supply and thus also exhibit a dose rate dependency in the threshold.

The next possible explanation could be that it is linked to the seeding of particles small enough to not be detected, onto which the copper will later be deposited. However, this is also unlikely for a couple of reasons: Even such small quantities of copper would statistically give a signal (albeit smaller in magnitude) when integrating over the entire region of interest, and as such is a very poor match with the stepwise linear response before and after the threshold dose. A signal-to-noise issue should result in an intercept with the y-axis comparable to the spread in the data, but that is not the case and both plots reveal that the fit deviates clearly in regions below 40 electrons/Å^2 or 1 MeV/Å^2.

As such, we are uncertain what causes this threshold dose, and would encourage further study to see if this is also observed with different systems. If that is the case it is very encouraging, since it would allow experiments to be designed with awareness of which dose to stay below to prevent the radiochemistry from interfering with normal chemical- and electrochemical observations.

Anomalous electroplating

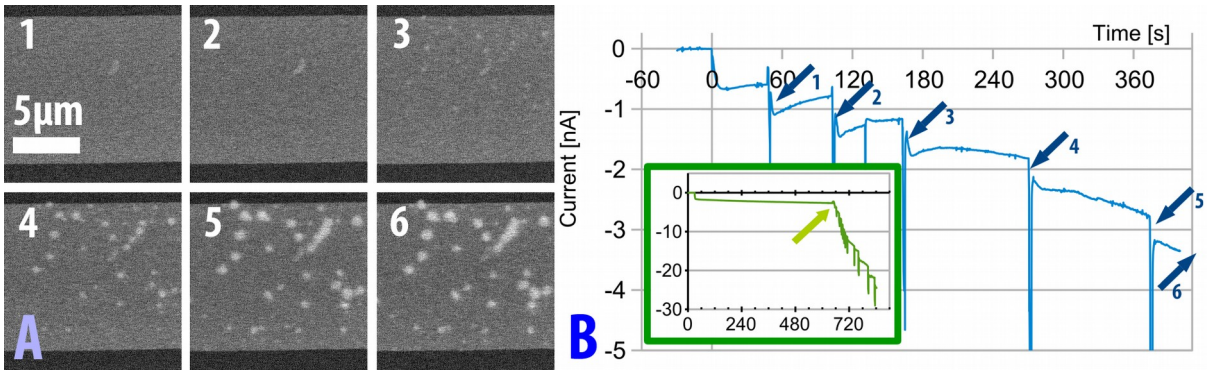

Figure 6.10: Electroplating current (B) increased with each successive image (indicated by arrows). This did not happen if the electrode was not irradiated (inset). After the 2nd image it was possible to see growing copper deposits in the irradiated region (A).

We observed that when electroplating at -0.075 V_{Cu} we had a low electrochemical current (Figure 6.10), and the current increased stepwise upon irradiation with SEM. The first image was taken one after minute the potential was applied, at which point there were no visible electroplated material. After two images, each a dose of only 0.03 e/Å^2 and well below the threshold in Figure 6.9, we could clearly see a deposit. For each successive image there was a significant increase in plated material.

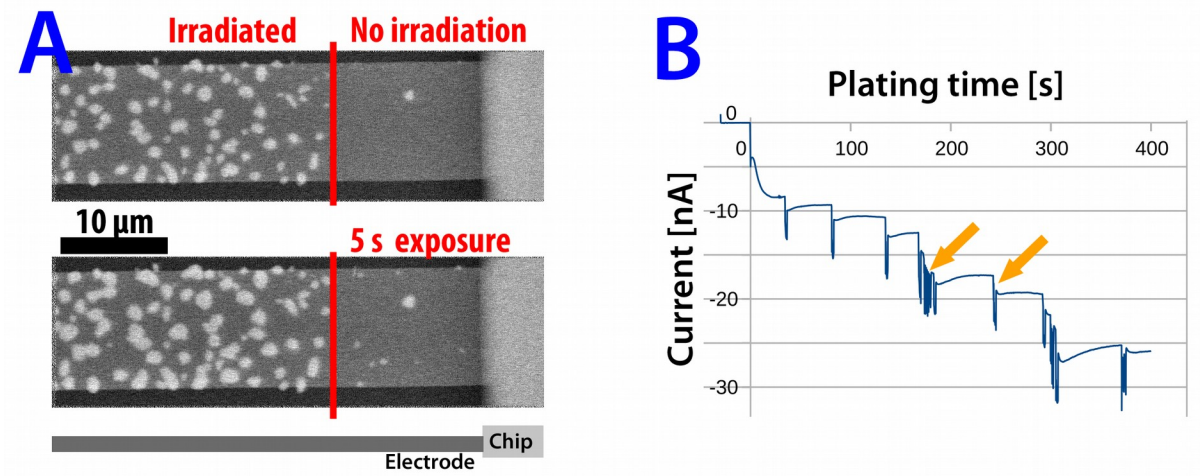

Figure 6.11: Electrochemical plating of copper was limited to the irradiated region (A) for more than three minutes until also the remaining part of the electrode was exposed for 5 seconds (arrows in B indicate the first and second image in which the right side is exposed). At this point growth was also occurring on the remaining part of the electrode. The dose for 5 seconds of exposure is less than 0.1 electrons per square Ångström.

When confining the radiation to only a portion of the electrode (Figure 6.11) we could see that the plating was also confined to this region. However, once the irradiated area was increased new nucleation points started appearing in the new region. After an initial irradiation not exceeding 0.1 e/Å^2 new spots appeared which grew simultaneously with the deposits in the first region, hence

there is no indication of proximity effects as otherwise observed during Ni electroless plating in SEM at 20-30 kV.[14]

Influence from the geometry at the edge of the electrode can be ruled out as the cause of the confined deposition in Figure 6.11, since when we irradiated an empty electrode in a small area confined to the middle (Figure 6.12) a similar confinement in electroplated material was seen. The total dose in this case was less than 1 electron per Å^2, which is still much lower than the threshold observed for pure beam induced nucleation.

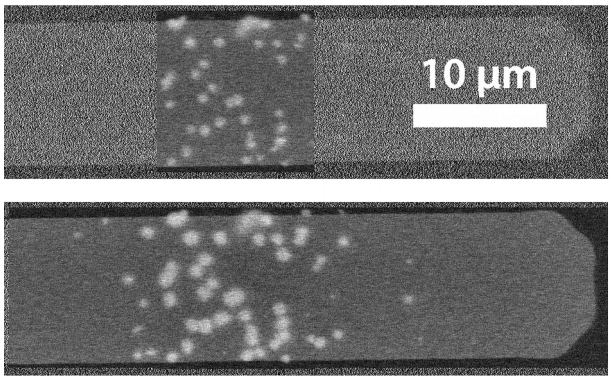

Figure 6.12: A segment of the electrode was irradiated more heavily (less than 1 electron per Å^2), and as with the previous experiment the initial growth was limited to the irradiated part of the electrode (visible here as a difference noise level). Only when a larger part of the electrode was exposed did electroplating occur elsewhere.

It seems then that the electron beam produces a localised reducing environment, which depending on applied potential and electron dose will either assist (negative potential, low dose) or trigger (no potential, higher dose)the nucleation and growth of metallic copper depending on the applied potential and the radiation dose. In this reducing environment seeds are formed in the irradiated region on which plating is preferential compared to the bare gold electrode. We note that at negative potentials the dose required before clear visible change in the amount of deposited copper is orders of magnitude lower than the previously observed 29 electrons per Ångström^2. Different electrodes varied in their observed currents, but the behaviour where plating did not occur until irradiated was the same in all cases.

Discussion

In our experiments we observed that the electron beam reduced copper ions to copper when the accumulated dose was sufficiently high. This allowed us to obtain an estimate of the g-value for copper when subjected to electron beam irradiation. This estimate is a lower bound for the following reasons:

First, we have assumed that all electrons deposit their entire energy in the liquid. If this was the case there would be no way to obtain an image. Approximately 5% of the incoming electrons are backscattered,[14] and as a consequence the g-value is under-estimated by the same amount.

Second, although we do not depend on resolution to obtain an estimate of the amount of copper, the depth from which we obtain backscattered electrons matter. CASINO simulations suggest that maybe as much as 25% of the energy is deposited too deep to observe, and consequently any radiolytic yield is not included.

Although some copper is etched away by the acidic solution, this is not likely to be a large cause a significant under-estimate of the g-value, since the graph suggests that time (i.e. diffusion) is not a significant effect.

The reported g-value for Cu^{2+} to Cu is on the order of 4-5. This value is two orders of magnitude higher than our observation of 0.050 per 100 eV. Even when accounting for factors which make our estimate a lower bound, an increase in this value of 30% does not alter the picture significantly. However, our observation is very close to the value of 0.04 which we calculated from published results on platinum. The ramification is that traditional g-values are not directly transferrable to in-situ electron microscopy conditions, and that further experiments are required to be able to correctly predict the electrolyte composition. Through this comparison our results also show that in this context SEM and TEM behave similarly.

One possible reason for the low g-value is the high irradiation intensity in the SEM. It is known alpha radiation that when an electrolyte is irradiated with particles which lose their energy in a shorter distance the g-value may decrease because the higher proximity between radiolytic products enables recombination.[22,29] If the high intensity of electron radiation in a focused spot creates a high proximity between radiolytic products similar to alpha particles one could expect the observed G-value to be somewhat lower than what Sosebee et al. measured by using the conventional approach at comparably low doses and dose rates.[28]

When irradiating the electrolyte directly we observed nucleation of copper on the membrane at irradiation doses above 29 electrons per Ångström^2 (equivalent to 0.7 MeV/Å^2). Below this threshold dose we observed no change, suggesting that perhaps other reactions dominate. However, when combining beam irradiation with an applied potential we found that this threshold was insufficient as a measure of a safe dose: Effects were seen at much lower doses, with nucleation points for further growth appearing confined to the irradiated region at as low as 0.03 electrons per Ångström^2.

How does our observed threshold compare to existing literature? In a 20 kV SEM-study on the reduction of platinum from an aqueous electrolyte[111] a threshold was indicated at a dose of 10 MeV/Å^2 for point-shaped exposures. Square platinum structures with sidelength of 2 µm were patterned with doses as low as 0.4 MeV/Å^2. Our exposure conditions resemble the latter more, where a large area is irradiated and the electrons lost due to lateral scattering are recuperated by neighbouring pixels. Our intensities are thus of the same order of magnitude as for platinum, but it seems that copper has a higher threshold. This could perhaps be linked to copper being less noble than platinum.

Conclusion

We have established a lower bound on the g-value for $Cu^{2+} \rightarrow Cu$ in acidic copper sulphate solution to be 0.05 per 100 eV when subjected to high dose electron beam irradiation by observing the change in image contrast. No change was observed below a threshold of 29 electrons per $Å^2$. This threshold was insufficient when applying a potential of -0.075 V_{Cu} on the gold electrode, where electroplating would start in areas which had been irradiated with doses as low as 0.03 electrons per $Å^2$.

This important result illustrates clearly the effect the electron beam might have in affecting the experimental outcome, and as such that it is necessary to exercise caution when interpreting in-situ electrochemical experiments – especially when such experiments are performed at potentials close to the transition-point between two opposite reactions (such as dissolution/electroplating). The results are transferable between SEM and STEM, and likely also to TEM, provided that the amount of energy that is deposited is correctly accounted for.

Chapter 7: Joint conclusion and outlook

In-situ electrochemical experiments performed in electron microscopes are currently experiencing a growth in interest and results. What started with individual research groups creating their own liquid cells and holders is now a field with several commercial players offering turn-key solutions with electrical connections and liquid flow. The proliferation of such equipment gives hope for a number of interesting and useful observations that can benefit future battery types, fuel cells and thin-film coatings to mention only a few applications.

But with this proliferation comes the increasing need to be able to rely on the experimental results. While in-situ optical microscopy imaging may indirectly affect the outcome in non-photosensitive experiments by heating up the sample, in-situ electron microscopy is a much more actively interfering due to its ionising nature: Ionising electron radiation is focused to a very high intensity in the sample, which in the case of water will cause radiolysis where water and other constituents of the electrolyte are split and recombined in new ways. These new reactive molecules can reach concentrations high enough to severely affect in-situ experiments, whether that is observing electrochemistry or for example the mixing of two chemicals.

This thesis has described the work performed to obtain a better experimental understanding of the radiolytic effects experienced in in-situ SEM and TEM experiments. The primary advantage of a TEM over SEM is the promise of higher resolution, an advantage that is often negated by the sample thickness and by samples where the SEM resolution of some tens of nanometers is sufficient to reach a satisfactory conclusion. Instead the SEM offers unique capabilities for stable standardised reference electrodes and large-area counter electrodes far enough away from the working electrodes that reaction products from the CE do not affect measurements at the working electrode. In-situ TEM is difficult – it relies on two fragile membranes, several good seals in a miniature packaging, combined with a very delicate and sensitive microscope. Unless the high resolution of TEM or other

analytical capabilities such as holography or electron energy loss spectroscopy is required then the SEM can in many cases provide a more versatile and productive platform for experiments.

To reach that experimental stage it has been necessary to consider which improvements might be needed for the EC-SEM system initially developed by Jensen. As a result of this a new electrode design with integrated connections for the potentiostat sense-electrode has been made. Second, a device with all-carbon electrodes has also been made by means of pyrolysis of AZ5214E photoresist.

These carbon electrodes were proven to be stable at 0.75 V higher potentials than comparable gold electrodes when subjected to oxidative potentials. Carbon is already one of the most important electrode materials in electrochemistry, so it is a significant advantage to also have such electrodes in the EC-SEM system. And in addition to applications where it acts as an inert electrode, it also opens up for studies in cases where it is an active electrode material – such as anode material for lithium batteries (although it is not yet certain that the electrode has sufficient porosity for this application).

The main studies in this thesis have revolved around radiolytic effects from the beam. Theoretical predictions such as that of Schneider et al. offer a best estimate of what the real electrochemistry could be like during and after irradiation, but because they often rely on extrapolations several orders of magnitude it is essential to complement such predictions with actual measurements. This thesis does exactly that in three ways:

First, since the highest radiolytic concentration is predicted to be of dissolved H_2 and H_2O_2 we have looked at how to quantify these with respect to each other. Hydrogen can be detected by means of OCP of platinum vs. a stable reference. Since OCP cannot be directly measured when injecting an electron beam current the actively regulated chronoamperometry set to zero current was used instead. By comparing to calibration measurements we saw that there was indeed a dramatic drop in OCP consistent with the presence of H_2, and could conclude that the concentration of H_2O_2 must be below 1:2.5 (relative to H_2), which is significantly lower than the predicted ratio of as high as 1:1.1 for deaerated solutions. The exact cause for this discrepancy is not yet clear, but it is possibly linked to the extremely high irradiation intensity and subsequent recombination. Such recombination may cause the g-values for different species to change relative to one another.

Presence of H_2 was also shown by the characteristic changes in the cyclic voltammogram. But as irradiation continued oxidative species caused the OCP to rise, and in addition also added a characteristic peak in the anodic current regime of the CV. Based on the CV the change is not consistent with O_2 or H_2O_2. We therefore hypothesise that this change is due to sulphur-based species from the radiolytically split sulphuric acid electrolyte. This hypothesis is corroborated by the CV which bears resemblance to reports in literature on sulphur chemistry.

Second, an increase in conductivity was observed by means of EIS when the area between two electrodes was irradiated with the electron beam. Compared to calibration measurements of KCl we found indications of an electrolyte conductivity of up to 400 µS/cm at 6 MGy/s. Since this value is

roughly two orders of magnitude higher than what can be attributed solely to H^+ according to Schneider's predictions there may be transient species (eg. solvated electrons) which make up for a sizeable contribution. We would like to perform additional experiments to cement the conclusion that the electrolyte conductivity is as high as we measured, but as it stands with our current measurements it may seem that Schneider's predictions offer a good qualitative picture of the radiolytic effects in our electrolyte, but that the quantitative values should be taken with some scepticism.

Third and finally, we looked at the radiolytic reduction of copper ions in an acidic sulfate solution. The effect has been demonstrated in several publications, but to date the rate of precipitation in electron microscopy studies has not been linked to the irradiation intensity. We therefore offer the first measured g-values for electron microscopy, here 0.05 atoms $Cu^{2+}_{(aq)} \rightarrow Cu_{(s)}$ per 100 eV. The value was reached by correlating the overall brightness of the backscattered electron image with the amount of electrochemically plated copper, then applying this correlation to infer the amount radiolytically reduced copper as a function of radiation dose.

Some published data can be re-analysed to also provide a g-value for other metal ions, and in the cases we analysed we reached values such as e.g. 0.04 for Pt, even though the method differed completely from our experiment. Our measured g-value for copper is two orders of magnitude lower than the published reference value for copper, which is quite likely related to the very high radiation intensity and dose used in an electron microscope compared to what would be typical for traditional studies of g-values.

Outlook and future experiments

Elliot and McCracken clearly illustrated the complexity of radiolysis when they presented more than 70 chemical reactions which take place to varying extent when irradiating water.[17] The many orders of magnitude difference in both radiation intensity and dose between experiments in the field can make it particularly difficult to predict the outcome of the many radiolytic processes occurring – especially in electrolytes more complex than pure water.

This only highlights the need for qualitative and quantitative measurements under realistic imaging conditions in both SEM, TEM and STEM, and to compare measurements performed with these different microscopy techniques. Mitigating strategies, such as scavengers, are also likely to become very important in future in-situ electron microscopy studies, since in most studies the radiolytic effects are merely an unwanted side-effect that is difficult to avoid when trying to resolve very small features with an electron microscope.

The results presented in this thesis demonstrate the need to explore possible scavengers which can help reduce electrolyte decomposition, so that it is possible to avoid e.g. the interference from sulphuric acid seen during the study of water radiolysis. In a similar vein, beam induced nucleation of copper was demonstrated to be affecting electrodeposition even below the dose where pure beam induced nucleation occurs. Published literature indicates that the solvated electron is the source of

metal ion reduction, and the experiment performed in this thesis could serve as a model system to test the effect of different forms of electron scavengers.

During the studies described in this thesis there are some particular future experiments that stand out as being able to build on the work that has been done here to further determine the actual radiolytic conditions. Some of these are listed below with a short discussion of how they could be performed and what to expect.

Qualitative study of radiolytic H_2 and H_2O_2 in TEM

Our extensive study of radiolytic hydrogen relative to hydrogen peroxide demonstrated a method that can be used to determine changes to the electrolyte composition in SEM. To repeat this experiment in-situ TEM would first and foremost provide a measurement of the radiolytic conditions applicable to anyone who performs in-situ TEM experiments on aqueous electrolytes.

Second, it would provide a more straight forward comparison to Schneider et al.'s calculations.[18] Determining to which extent their approach based on low-dose radiolytic values translates to electron microscopy would make it clear whether it would be useful to extend their model to describe more complex electrolytes, or if only direct measurements provide useful predictions of the radiolytic outcome. Finally, an experiment using the same method as our SEM study would demonstrate if the SEM acts as a good model system for TEM, which would make it easier to assess new electrolytes and scavengers than if all experiments have to be performed in a TEM.

There are however some significant challenges associated with this. In the EC-SEM system a sealed reference electrode is used which does not interfere with the electrolyte. Similarly, the counter electrode is placed far away from the working electrode, separated by a narrow channel. In a TEM system all of these electrodes have to fit on the same chip (at least with most common in-situ electrochemical systems), which increases the risk of products from the counter electrode interfering with the measurement at the working electrode. There are also concerns for the reference electrode: It is exposed directly to the electrolyte, which means that an appropriate choice of electrolyte and electrode material must be made. It is also possible that the miniature nature of a thin-film reference electrode means that longevity and stability will be a concern. Neither of these two concerns affect the EC-SEM system, which nicely illustrates the greater flexibility inherent to the slightly larger design.

The process to carry out these experiments has already started with the design of suitable devices, where two separate mask sets allow the reference electrode to be made with a different material than the working electrode, for example Pt working- and counter electrodes, vs. a silver-based reference electrode.

Quantitative study to determine the G-value for O_2 and H_2O_2

In our experiments we demonstrated that water radiolysis was an issue, and obtained a ratio of H_2 to H_2O_2. If all the H_2O_2 and O_2 can be collected and measured electrochemically it would be possible to obtain a more precise measure of the g-value. Liedhegner et al. described such a membrane

device to determine the radiolytic yield resulting from alpha radiation.[30] With an electrochemical electrode they directly measure the radiolytic products, and do not depend on the conversion of constituents of the electrolyte to an optically detectable form, such as for example the Fricke dosimeter. A direct electrochemical device is preferable since chemical methods of measuring dose or yield can be depleted when all sensitive molecules in the solution have reacted.

By replacing the EC-SEM electrode layer with a large thin-film sheet of silver a large-area active electrode which can be used to reduce O_2 and H_2O_2, nearly all of which can be measured by means of chronoamperometry. The SEM has the advantage of a large Pt counter electrode far away from the working electrode chip, as well as the option to use any type of miniature reference electrode. It is therefore possible to perform the experiment nearly completely analogous to Liedhegner, except with the radiation conditions relevant for electron microscopy.

A similar experiment could be designed for TEM and STEM. In this case lithographically defined electrodes would be necessary, since counter- and reference electrodes have to be on the same chip (with most common implementations). This may lead to issues with reference electrode degradation or interference from reactions occurring on the counter electrode, but whether such issues are severe enough to prevent reliable measurements is not certain.

Radiolytic reduction of copper and other materials in-situ TEM

Radiolytic reduction of metal ions is an excellent model system to compare different types of irradiation profiles, such as the scanning beam in SEM and STEM vs. homogeneous irradiation in TEM. Such reduction of several different metals have been documented (e.g. copper,[105] gold,[19] silver,[53] etc.) for individual systems, but with the combination of resources in our group it would be possible to perform a comparison with identical chemistry across different microscope types.

The experiment performed in this thesis would be relatively easy to repeat in a TEM cell. No special electrodes are needed, which means that the limited electrode area and challenges associated with different electrode material choices are eliminated. That reduces the task to keeping track of the irradiation intensity and dose, so that the amount of reduced metal can be reliably linked to the accumulated dose. Any metal ion that can be reduced by the electron beam could be used, and in this thesis it has been demonstrated that copper is a suitable system. By using the same system for both TEM and STEM it would be possible to offer a much needed clarification on how much of a difference it makes for radiolysis to receive the entire pixel-dose in a single high-intensity pulse (STEM), compared to averaging it over a certain exposure time (TEM).

In the discussion of the radiolytic reduction in chapter 6 we compare our results to state-of-the-art TEM experiments, some of which allow an equivalent G-value to be calculated. It may be possible to perform such calculations for additional published studies, though in some cases it may be necessary to obtain additional information on e.g. accumulated dose or microscope configuration.

The combination of experimental study across imaging types (SEM, STEM, TEM) for a single material (e.g. Cu) combined with an exhaustive review of such studies across different materials

would allow for a robust conclusion on the beam effect, and provide a standard against which to test e.g. scavengers and other mitigating strategies for in-situ experiments.

Bibliography

1. Wang, J. *et al.* Structural Evolution and Pulverization of Tin Nanoparticles during Lithiation-Delithiation Cycling. *J. Electrochem. Soc.* **161,** F3019–F3024 (2014).
2. Abrams, I. M. & McBain, J. W. A Closed Cell for Electron Microscopy. *J. Appl. Phys.* **15,** 607–609 (1944).
3. Jonge, N. de & Ross, F. M. Electron microscopy of specimens in liquid. *Nat. Nanotechnol.* **6,** 695–704 (2011).
4. Wang, C.-M. In situ transmission electron microscopy and spectroscopy studies of rechargeable batteries under dynamic operating conditions: A retrospective and perspective view. *J. Mater. Res.* **30,** 326–339 (2015).
5. Wang, J. W. *et al.* Two-Phase Electrochemical Lithiation in Amorphous Silicon. *Nano Lett.* **13,** 709–715 (2013).
6. Huang, J. Y. *et al.* In Situ Observation of the Electrochemical Lithiation of a Single SnO2 Nanowire Electrode. *Science* **330,** 1515–1520 (2010).
7. Arimoto, S., Kageyama, H., Torimoto, T. & Kuwabata, S. Development of in situ scanning electron microscope system for real time observation of metal deposition from ionic liquid. *Electrochem. Commun.* **10,** 1901–1904 (2008).
8. Joy, D. C. & Joy, C. S. Scanning electron microscope imaging in liquids – some data on electron interactions in water. *J. Microsc.* **221,** 84–88 (2006).
9. Nishiyama, H. *et al.* Atmospheric scanning electron microscope observes cells and tissues in open medium through silicon nitride film. *J. Struct. Biol.* **169,** 438–449 (2010).
10. Radisic, A., Vereecken, P. M., Searson, P. C. & Ross, F. M. The morphology and nucleation kinetics of copper islands during electrodeposition. *Surf. Sci.* **600,** 1817–1826 (2006).
11. Zheng, H., Claridge, S. A., Minor, A. M., Alivisatos, A. P. & Dahmen, U. Nanocrystal Diffusion in a Liquid Thin Film Observed by in Situ Transmission Electron Microscopy. *Nano*

Lett. **9,** 2460–2465 (2009).

12. Grogan, J. M. & Bau, H. H. The Nanoaquarium: A Platform for In Situ Transmission Electron Microscopy in Liquid Media. *J. Microelectromechanical Syst.* **19,** 885–894 (2010).
13. Ring, E. A., Peckys, D. B., Dukes, M. J., Baudoin, J. P. & De Jonge, N. Silicon nitride windows for electron microscopy of whole cells. *J. Microsc.* **243,** 273–283 (2011).
14. Jensen, E., Køble r, C., Jensen, P. S. & Mølhave, K. In-situ SEM microchip setup for electrochemical experiments with water based solutions. *Ultramicroscopy* **129,** 63–69 (2013).
15. Masuda, T. *et al.* In situ x-ray photoelectron spectroscopy for electrochemical reactions in ordinary solvents. *Appl. Phys. Lett.* **103,** 111605 (2013).
16. Le Caër, S. Water Radiolysis: Influence of Oxide Surfaces on H2 Production under Ionizing Radiation. *Water* **3,** 235–253 (2011).
17. Elliot, A. J. & McCracken, D. R. Aqueous Lithium Salt Blanket (ALSB) Concept Computer modelling of the radiolysis in an aqueous lithium salt blanket: Suppression of radiolysis by addition of hydrogen. *Fusion Eng. Des.* **13,** 21–27 (1990).
18. Schneider, N. M. *et al.* Electron–Water Interactions and Implications for Liquid Cell Electron Microscopy. *J. Phys. Chem. C* **118,** 22373–22382 (2014).
19. Grogan, J. M., Schneider, N. M., Ross, F. M. & Bau, H. H. Bubble and Pattern Formation in Liquid Induced by an Electron Beam. *Nano Lett.* **14,** 359–364 (2013).
20. Woehl, T. J. *et al.* Experimental procedures to mitigate electron beam induced artifacts during in situ fluid imaging of nanomaterials. *Ultramicroscopy* **127,** 53–63 (2013).
21. Woods, R. J. & Pikaev, A. K. *Applied Radiation Chemistry: Radiation Processing*. (John Wiley & Sons, 1994).
22. Anderson, A. R. A CALORIMETRIC DETERMINATION OF THE OXIDATION YIELD OF THE FRICKE DOSIMETER AT HIGH DOSE RATES OF ELECTRONS1a. *J. Phys. Chem.* **66,** 180–182 (1962).
23. Barker, G. C. & Fowles, P. Pulse radiolytic induced transient electrical conductance in liquid solutions. *Trans. Faraday Soc.* **66,** 1661–1669 (1970).
24. Watson, C. *et al.* Pulsed Electron Beam Water Radiolysis for Sub-Microsecond Hydroxyl Radical Protein Footprinting. *Anal. Chem.* **81,** 2496–2505 (2009).
25. Barker, G. C., Fowles, P., Sammon, D. C. & Stringer, B. Pulse radiolytic induced transient electrical conductance in liquid solutions. Part 1.—Technique and the radiolysis of water. *Trans. Faraday Soc.* **66,** 1498–1508 (1970).
26. Buxton, G. V., Greenstock, C. L., Helman, W. P. & Ross, A. B. Critical Review of rate constants for reactions of hydrated electrons, hydrogen atoms and hydroxyl radicals (·OH/·O− in Aqueous Solution. *J. Phys. Chem. Ref. Data* **17,** 513–886 (1988).
27. de Cointet, C., Mostafavi, M., Khatouri, J. & Belloni, J. Growth and Reactivity of Silver Clusters in Cyanide Solution. *J. Phys. Chem. B* **101,** 3512–3516 (1997).
28. Sosebee, T., Giersig, M., Holzwarth, A. & Mulvaney, P. The Nucleation of Colloidal Copper in the Presence of Poly(ethyleneimine). *Berichte Bunsenges. Für Phys. Chem.* **99,** 40–49 (1995).
29. Burns, W. G. & Sims, H. E. Effect of radiation type in water radiolysis. *J. Chem. Soc. Faraday Trans. 1 Phys. Chem. Condens. Phases* **77,** 2803–2813 (1981).

30. Liedhegner, J. E. *et al.* Rapid Electrochemical Detection of Radiolysis Products in an Aqueous Solution Exposed to Alpha Particle Beams, Rapid Electrochemical Detection of Radiolysis Products in an Aqueous Solution Exposed to Alpha Particle Beams. *Int. J. Electrochem. Int. J. Electrochem.* **2011, 2011,** e864126 (2011).

31. Christensen, H., Studsvik Energiteknik, A. B. & Bjergbakke, E. EFFECT OF B-RADIOLYSIS ON THE PRODUCTS FROM a-RADIOLYSIS OF GROUND WATER. *SKBFKBS Tech. Rep.* **84,** (1984).

32. Christensen, H. & Bjergbakke, E. Radiolysis of Groundwater from HLW Stored in Copper Canisters. in *Symposium D – Scientific Basis for Nuclear Waste Management VI* **15,** (1982).

33. Littauer, E. L. & Tsai, K. C. Observations of the diffusion coefficient of the hydroxyl ion in lithium hydroxide solutions. *Electrochimica Acta* **24,** 351–355 (1979).

34. Bridel, J.-S., Azaïs, T., Morcrette, M., Tarascon, J.-M. & Larcher, D. In Situ Observation and Long-Term Reactivity of Si/C/CMC Composites Electrodes for Li-Ion Batteries. *J. Electrochem. Soc.* **158,** A750–A759 (2011).

35. Neudecker, B. J., Dudney, N. J. & Bates, J. B. 'Lithium-Free' Thin-Film Battery with In Situ Plated Li Anode. *J. Electrochem. Soc.* **147,** 517–523 (2000).

36. Hartl, K., Hanzlik, M. & Arenz, M. IL-TEM investigations on the degradation mechanism of Pt/C electrocatalysts with different carbon supports. *Energy Environ. Sci.* **4,** 234–238 (2010).

37. Amalraj, S. F. & Aurbach, D. The use of in situ techniques in R&D of Li and Mg rechargeable batteries. *J. Solid State Electrochem.* **15,** 877–890 (2011).

38. Ruska, E. The development of the electron microscope and of electron microscopy. *Rev. Mod. Phys.* **59,** 627 (1987).

39. Clark, J. B. Transmission electron microscopy study of age hardening in a Mg-5 wt.% Zn alloy. *Acta Metall.* **13,** 1281–1289 (1965).

40. Magnusson, M. H., Deppert, K., Malm, J.-O., Bovin, J.-O. & Samuelson, L. Gold Nanoparticles: Production, Reshaping, and Thermal Charging. *J. Nanoparticle Res.* **1,** 243–251 (1999).

41. Danev, R., Kanamaru, S., Marko, M. & Nagayama, K. Zernike phase contrast cryo-electron tomography. *J. Struct. Biol.* **171,** 174–181 (2010).

42. Giannuzzi, L. A., Drown, J. L., Brown, S. R., Irwin, R. B. & Stevie, F. A. Applications of the FIB lift-out technique for TEM specimen preparation. *Microsc. Res. Tech.* **41,** 285–290 (1998).

43. Hansen, T. W. *et al.* Atomic-Resolution in Situ Transmission Electron Microscopy of a Promoter of a Heterogeneous Catalyst. *Science* **294,** 1508–1510 (2001).

44. Berger, M. J., Coursey, J. S., Zucker, M. A. & Chang, J. *Stopping-Power and Range Tables for Electrons, Protons, and Helium Ions*. (NIST, Physical Measurement Laboratory).

45. Wittke, J. H. Instrumentation - Electron Microprobe Laboratory - Northern Arizona University. (2015). Available at: http://nau.edu/cefns/labs/electron-microprobe/glg-510-class-notes/instrumentation/. (Accessed: 3rd March 2016)

46. Orloff, J. *Handbook of Charged Particle Optics, Second Edition*. (CRC Press, 2008).

47. Hagstrum, H. D. & Tate, J. T. Ionization and Dissociation of Diatomic Molecules by Electron Impact. *Phys. Rev.* **59,** 354–370 (1941).

48. Seah, M. P. & Dench, W. A. Quantitative electron spectroscopy of surfaces: A standard data base for electron inelastic mean free paths in solids. *Surf. Interface Anal.* **1,** 2–11 (1979).

49. Thiel, B. L. Master curves for gas amplification in low vacuum and environmental scanning electron microscopy. *Ultramicroscopy* **99,** 35–47 (2004).

50. Hill, M. A. & Smith, F. A. Calculation of initial and primary yields in the radiolysis of water. *Radiat. Phys. Chem.* **43,** 265–280 (1994).

51. Bielski, B. H. J. Reevaluation of the Spectral and Kinetic Properties of Ho2 and O2- Free Radicals. *Photochem. Photobiol.* **28,** 645–649 (1978).

52. Jensen, E. Engineering Electrochemical Setups for Electron Microscopy of Liquid Processes. (Technical University of Denmark, 2012).

53. Noh, K. W., Liu, Y., Sun, L. & Dillon, S. J. Challenges associated with in-situ TEM in environmental systems: The case of silver in aqueous solutions. *Ultramicroscopy* **116,** 34–38 (2012).

54. Wu, F. & Yao, N. Advances in sealed liquid cells for in-situ TEM electrochemial investigation of lithium-ion battery. *Nano Energy* **11,** 196–210 (2015).

55. Schneider, N. M. *et al.* Visualization of Active and Passive Control of Morphology during Electrodeposition. *Microsc. Microanal.* **20,** 1530–1531 (2014).

56. Sutter, E. *et al.* In situ liquid-cell electron microscopy of silver–palladium galvanic replacement reactions on silver nanoparticles. *Nat. Commun.* **5,** 4946 (2014).

57. Zhu, G.-Z. *et al.* In Situ Liquid Cell TEM Study of Morphological Evolution and Degradation of Pt–Fe Nanocatalysts During Potential Cycling. *J. Phys. Chem. C* **118,** 22111–22119 (2014).

58. Cherevko, S., Topalov, A. A., Katsounaros, I. & Mayrhofer, K. J. J. Electrochemical dissolution of gold in acidic medium. *Electrochem. Commun.* **28,** 44–46 (2013).

59. Beilby, A. L. & Carlsson, A. A pyrolytic carbon film electrode for voltammetry: Part V. characterization and comparison with the glassy carbon electrode by electrochemical pretreatment in basic solution. *J. Electroanal. Chem. Interfacial Electrochem.* **248,** 283–304 (1988).

60. Larsen, S. T. *et al.* Pyrolyzed Photoresist Electrodes for Integration in Microfluidic Chips for Transmitter Detection from Biological Cells. *ECS Electrochem. Lett.* **2,** B5–B7 (2013).

61. Kim, J., Song, X., Kinoshita, K., Madou, M. & White, R. Electrochemical Studies of Carbon Films from Pyrolyzed Photoresist. *J. Electrochem. Soc.* **145,** 2314–2319 (1998).

62. Amato, L. *et al.* Novel Nanostructured Electrodes Obtained by Pyrolysis of Composite Polymeric Materials. *Electroanalysis* n/a–n/a (2015). doi:10.1002/elan.201400430

63. Amato, L. *et al.* Dense high-aspect ratio 3D carbon pillars on interdigitated microelectrode arrays. *Carbon* **94,** 792–803 (2015).

64. Lee, J. A., Lee, S. W., Lee, K.-C., Park, S. I. & Lee, S. S. Fabrication and characterization of freestanding 3D carbon microstructures using multi-exposures and resist pyrolysis. *J. Micromechanics Microengineering* **18,** 035012 (2008).

65. Park, B. Y., Taherabadi, L., Wang, C., Zoval, J. & Madou, M. J. Electrical Properties and Shrinkage of Carbonized Photoresist Films and the Implications for Carbon Microelectromechanical Systems Devices in Conductive Media. *J. Electrochem. Soc.* **152,**

J136–J143 (2005).

66. Verch, A., Pfaff, M. & de Jonge, N. Exceptionally Slow Movement of Gold Nanoparticles at a Solid/Liquid Interface Investigated by Scanning Transmission Electron Microscopy. *Langmuir* **31,** 6956–6964 (2015).
67. Abellan, P. *et al.* Probing the Degradation Mechanisms in Electrolyte Solutions for Li-Ion Batteries by in Situ Transmission Electron Microscopy. *Nano Lett.* **14,** 1293–1299 (2014).
68. Abellan, P. *et al.* Factors influencing quantitative liquid (scanning) transmission electron microscopy. *Chem. Commun.* **50,** 4873–4880 (2014).
69. Daubinger, P., Kieninger, J., Unmüssig, T. & Urban, G. A. Electrochemical characteristics of nanostructured platinum electrodes – a cyclic voltammetry study. *Phys. Chem. Chem. Phys.* **16,** 8392–8399 (2014).
70. James, B. Advances in 'wet' electron microscopy techniques and their application to the study of food structure. *Trends Food Sci. Technol.* **20,** 114–124 (2009).
71. Bouchet, R., Siebert, E. & Vitter, G. Polybenzimidazole-Based Hydrogen Sensors I. Mechanism of Response with an E-TEK Gas Diffusion Electrode. *J. Electrochem. Soc.* **147,** 3125–3130 (2000).
72. Kuhlmann, J., Witte, F. & Heineman, W. R. Electrochemical Sensing of Dissolved Hydrogen in Aqueous Solutions as a Tool to Monitor Magnesium Alloy Corrosion. *Electroanalysis* **25,** 1105–1110 (2013).
73. Korotcenkov, G., Do Han, S. & Stetter, J. R. Review of Electrochemical Hydrogen Sensors. *Chem. Rev.* **109,** 1402–1433 (2009).
74. Siebert, E., Rosini, S., Bouchet, R. & Vitter, G. Mixed potential type hydrogen sensor. *Ionics* **9,** 168–175 (2003).
75. Evans, S. A. G. *et al.* Detection of Hydrogen Peroxide at Mesoporous Platinum Microelectrodes. *Anal. Chem.* **74,** 1322–1326 (2002).
76. Zain, Z. M. & Zakaria, N. Hydrogen Peroxide Impedimetric Detection on Poly-Ortho-Phenylenediamine Modified Platinum Disk Microelectrode. *Malays. J. Anal. Sci.* **18,** 107–115 (2014).
77. Gu, Y. & Chen, C.-C. Eliminating the Interference of Oxygen for Sensing Hydrogen Peroxide with the Polyaniline Modified Electrode. *Sensors* **8,** 8237–8247 (2008).
78. Wiesenburg, D. A. & Guinasso, N. L. Equilibrium solubilities of methane, carbon monoxide, and hydrogen in water and sea water. *J. Chem. Eng. Data* **24,** 356–360 (1979).
79. Weiss, R. F. The solubility of nitrogen, oxygen and argon in water and seawater. *Deep Sea Res. Oceanogr. Abstr.* **17,** 721–735 (1970).
80. Cussler, E. L. *Diffusion: mass transfer in fluid systems*. (Cambridge University Press, 2009).
81. Pena, R. C. Studies on the Electrocatalytic Reduction of Hydrogen Peroxide on a Glassy Carbon Electrode Modified With a Ruthenium Oxide Hexacyanoferrate Film. *Int. J. Electrochem. Sci.* **6,** 394–403 (2011).
82. Fu, J., Hou, M., Du, C., Shao, Z. & Yi, B. Potential dependence of sulfur dioxide poisoning and oxidation at the cathode of proton exchange membrane fuel cells. *J. Power Sources* **187,** 32–38 (2009).

83. Leddicotte, G. W. *The radiochemistry of sulfur.* (Oak Ridge National Lab., 1961).
84. Gould, B. D., Baturina, O. A. & Swider-Lyons, K. E. Deactivation of Pt/VC proton exchange membrane fuel cell cathodes by SO2, H2S and COS. *J. Power Sources* **188,** 89–95 (2009).
85. Radiometer analytical. *Conductivity - Theory and Practice*. (2004).
86. Ayliffe, H. E., Bruno Frazier, A. & Rabbitt, R. D. Electric impedance spectroscopy using microchannels with integrated metal electrodes. *J. Microelectromechanical Syst.* **8,** 50–57 (1999).
87. Light, T. S., Kingman, B. & Bevilacqua, A. C. The Conductivity of Low Concentrations of CO2 Dissolved in Ultrapure Water from 0-100 C. in *209th American Chemical Society National Meeting* 2–6 (1995).
88. Day, T. J. F., Schmitt, U. W. & Voth, G. A. The Mechanism of Hydrated Proton Transport in Water. *J. Am. Chem. Soc.* **122,** 12027–12028 (2000).
89. Coury, L. Conductance Measurements - Part 1: Theory. *Curr. Sep. Biolytical Syst. Inc* (1999).
90. Schmidt, K. H., Han, P. & Bartels, D. M. Temperature dependence of solvated electron diffusion in water and water-d2. *J. Phys. Chem.* **96,** 199–206 (1992).
91. Table of conductivity vs concentration for common solutions. (1999).
92. Schumb, W. C. Stability of Concentrated Hydrogen Peroxide Solutions. *Ind. Eng. Chem.* **41,** 992–1003 (1949).
93. Sheldon, S. & Downing, G. M. The Critical Current Density for Copper Deposition and the Absolute Velocity of Migration of Copper Ions. *Phys. Rev. Ser. I* **1,** 51–58 (1893).
94. Mahla, E. M. Stress in Electrodeposited Copper as Determined by X-Rays. *Trans. Electrochem. Soc.* **77,** 145–156 (1940).
95. Johnson, G. R. & Turner, D. R. The Effect of Some Addition Agents on the Kinetics of Copper Electrodeposition from a Sulfate Solution II . Rotating Disk Electrode Experiments. *J. Electrochem. Soc.* **109,** 918–922 (1962).
96. Turner, D. R. & Johnson, G. R. The Effect of Some Addition Agents on the Kinetics of Copper Electrodeposition from a Sulfate Solution I . Cathode Potential-Current Density Relation. *J. Electrochem. Soc.* **109,** 798–804 (1962).
97. Andricacos, P. C., Uzoh, C., Dukovic, J. O., Horkans, J. & Deligianni, H. Damascene Copper Electroplating for Chip Interconnections. *IBM J Res Dev* **42,** 567–574 (1998).
98. Ueno, K., Ritzdorf, T. & Grace, S. Seed layer dependence of room-temperature recrystallization in electroplated copper films. *J. Appl. Phys.* **86,** 4930–4935 (1999).
99. Vicenzo, A. & Cavallotti, P. L. Copper electrodeposition from a pH 3 sulfate electrolyte. *J. Appl. Electrochem.* **32,** 743–753 (2002).
100. Radisic, A., Ross, F. M. & Searson, P. C. In Situ Study of the Growth Kinetics of Individual Island Electrodeposition of Copper. *J. Phys. Chem. B* **110,** 7862–7868 (2006).
101. Beverskog, B. & Puigdomenech, I. Revised Pourbaix Diagrams for Copper at 25 to 300°C. *J. Electrochem. Soc.* **144,** 3476–3483 (1997).
102. Liu, X. H. *et al.* In situ atomic-scale imaging of electrochemical lithiation in silicon. *Nat. Nanotechnol.* **7,** 749–756 (2012).

103. Brunetti, G. *et al.* Confirmation of the Domino-Cascade Model by LiFePO4/FePO4 Precession Electron Diffraction. *Chem. Mater.* **23,** 4515–4524 (2011).

104. Radisic, A., Vereecken, P. M., Hannon, J. B., Searson, P. C. & Ross, F. M. Quantifying Electrochemical Nucleation and Growth of Nanoscale Clusters Using Real-Time Kinetic Data. *Nano Lett.* **6,** 238–242 (2006).

105. Heijer, M. den, Shao, I., Radisic, A., Reuter, M. C. & Ross, F. M. Patterned electrochemical deposition of copper using an electron beam. *APL Mater.* **2,** 022101 (2014).

106. White, E. R. *et al.* In Situ Transmission Electron Microscopy of Lead Dendrites and Lead Ions in Aqueous Solution. *ACS Nano* **6,** 6308–6317 (2012).

107. Evans, J. E., Jungjohann, K. L., Browning, N. D. & Arslan, I. Controlled Growth of Nanoparticles from Solution with In Situ Liquid Transmission Electron Microscopy. *Nano Lett.* **11,** 2809–2813 (2011).

108. Schardein, G., Donev, E. U. & Hastings, J. T. Electron-beam-induced deposition of gold from aqueous solutions. *Nanotechnology* **22,** 015301 (2011).

109. Zheng, H. *et al.* Observation of Single Colloidal Platinum Nanocrystal Growth Trajectories. *Science* **324,** 1309–1312 (2009).

110. Noulty, R. A. & Leaist, D. G. Diffusion in aqueous copper sulfate and copper sulfate-sulfuric acid solutions. *J. Solut. Chem.* **16,** 813–825 (1987).

111. Donev, E. U. & Hastings, J. T. Electron-Beam-Induced Deposition of Platinum from a Liquid Precursor. *Nano Lett.* **9,** 2715–2718 (2009).

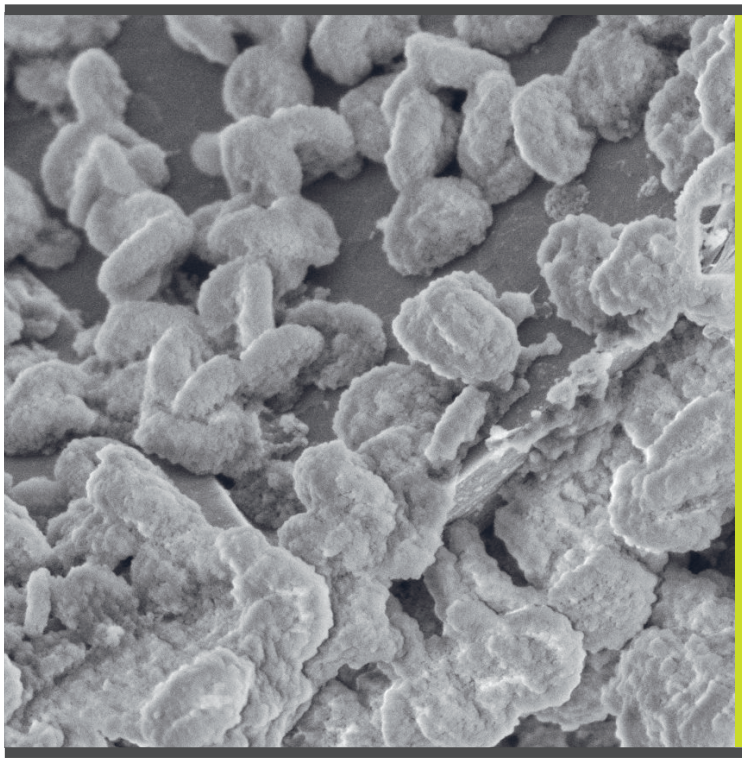

Published by:
DTU Nanotech
Department of Micro- and Nanotechnology
Technical University of Denmark
Ørsteds Plads, building 345C
DK-2800 Kgs. Lyngby